UNIVERSITY OF GENOVA

PHD COURSE IN:
SCIENCES AND TECHNOLOGIES FOR THE EARTH AND ENVIRONMENT

Potential fields data modeling: new frontiers in forward and inverse problems

by

Alessandro Ghirotto

Thesis submitted for the degree of *Doctor of Philosophy* (35° cycle)

22nd May 2023

Prof. Egidio Armadillo, *University of Genova*	Supervisor
Dr. Andrea Zunino, *ETH Zürich*	Supervisor
Prof. Marco Scambelluri, *University of Genova*	Head of the PhD program

Thesis Jury:

Prof. Klaus Mosegaard, *University of Copenhagen*	External examiner
Prof. Alberto Godio, *Politecnico di Torino*	External examiner
Prof. Marco Scambelluri, *University of Genova*	Internal examiner

Università di Genova | DISTAV DIPARTIMENTO DI SCIENZE DELLA TERRA, DELL'AMBIENTE E DELLA VITA

Earth, Environment and Life Sciences Department

There will always be rocks in the road ahead of us. They will be stumbling blocks or stepping stones; it all depends on how you use them.

Friedrich Nietzsche

To my grandparents Erminio, Umberto and Ines who always assist and support me from heaven, and to my grandmother Rina who still fills my life with love.

Acknowledgements

I would like to thank my supervisors Prof. Egidio Armadillo and Dr. Andrea Zunino for the time, experience and opportunities they have provided me during this challenging but exciting PhD course. Prof. Egidio Armadillo has been my mentor since the last year of the B.Sc. in geological sciences, and he has continued to dispense me wise and constructive advice ever since. I thank him, in particular, for his rare ability to stimulate my curiosity and to convey me his passion for applied geophysics, a discipline on which I am starting to build my scientific career. I am also very grateful to Dr. Andrea Zunino to have opened me the door to the world of inverse problems, a fascinating research field on which I have almost entirely founded this thesis work and planned my future research outputs. In addition, thanks to Dr. Andrea Zunino I had the opportunity to meet Prof. Klaus Mosegaard at the Niels Bohr Institute of the University of Copenhagen and Prof. Andreas Fichtner at ETH Zürich, with whom I had interesting scientific discussions culminated in some first-class research papers.

Among all the people I have had the opportunity to get to know at the DISTAV department, i.e., my home institution, I would particularly like to thank Prof. Laura Crispini for always believing in my abilities, even supporting my projects and research visits abroad financially.

A special thanks goes to Silvia, my brilliant sweetheart, who shares with me the passion for scientific research and this hard but rewarding type of career. She has always understood to the core how much energy and commitment I put into this PhD, helping me never to give up. We always supported each other even in the most difficult moments, always trying to come out with our heads held high together. Notwithstanding, the darkest moments have

strengthened our feelings even more, transforming these last years into the most beautiful we have ever lived together.

My biggest thanks go to my family, of whom I am very proud. They have always supported me emotionally and financially from the first to the last day of my studies, giving me the means to reach such an important milestone in my life and the chance to lay the foundation for a future ambitious scientific career. To my father, I owe my great passion for science and research, to my mother my great stubbornness, qualities that also endowed my dear sister Valentina, enabling her to achieve brilliant academic results.

My heartfelt thanks go to my grandparents, to whom this thesis is dedicated. I hope to have done everything possible so that they can truly be proud of me, albeit my greatest sorrow will be to not having them present at my PhD defence.

Abstract

Since the ’50, potential fields data modeling has played an important role in analyzing the density and magnetization distribution in Earth’s subsurface for a wide variety of applications. Examples are the characterization of ore deposits and the assessment of geothermal and petroleum potential, which turned out to be key contributors for the economic and industrial development after World War II.

Current modeling methods mainly rely on two popular parameterization approaches, either involving a discretization of target geological bodies by means of 2D to 2.75D horizontal prisms with polygonal vertical cross-section (polygon-based approach) or prismatic cells (prism-based approach). Despite the great endeavour made by scientists in recent decades, inversion methods based on these parameterization approaches still suffers from a limited ability to (i) realistically characterize the variability of density and magnetization expected in a study area and (ii) take into account the strong non-uniqueness affecting potential fields theory. The prism-based approach is used in linear deterministic inverse methods, which provide just one single solution, preventing uncertainty estimation and statistical analysis on the parameters we would like to characterize (i.e, density or magnetization). On the contrary, the polygon-based approach is almost exclusively exploited in a trial-and-error modeling strategy, leaving the potential to develop innovative inverse methods untapped. The reason is two-fold, namely (i) its strongly non-linear forward problem requires an efficient probabilistic inverse modeling methodology to solve the related inverse problem, and (ii)

unpredictable cross-intersections between polygonal bodies during inversion represent a challenging task to be tackled in order to achieve geologically plausible model solutions.

The goal of this thesis is then to contribute to solving the critical issues outlined above, developing probabilistic inversion methodologies based on the polygon- and prism-based parameterization approaches aiming to help improving our capability to unravel the structure of the subsurface.

Regarding the polygon-based parameterization strategy, at first a deep review of its mathematical framework has been performed, allowing us (i) to restore the validity of a recently criticized mathematical formulation for the 2D magnetic case, and (ii) to find an error sign in the derivation for the 2.75D magnetic case causing potentially wrong numerical results. Such preliminary phase allowed us to develop a methodology to independently or jointly invert gravity and magnetic data exploiting the Hamilton Monte Carlo approach, thanks to which collection of models allow researchers to appraise different geological scenarios and fully characterize uncertainties on the model parameters. Geological plausibility of results is ensured by automatic checks on the geometries of modelled bodies, which avoid unrealistic cross-intersections among them.

Regarding the prism-based parameterization approach, the linear inversion method based on the probabilistic approach considers a discretization of target geological scenarios by prismatic bodies, arranged horizontally to cover it and finitely extended in the vertical direction, particularly suitable to model density and magnetization variability inside strata. Its strengths have been proven, for the magnetic case, in the characterization of the magnetization variability expected for the shallower volcanic unit of the Mt. Melbourne Volcanic Field (Northern Victoria Land, Antarctica), helping significantly us to unravel its poorly known inner geophysical architecture.

Scientific products

Journal papers

1. **Ghirotto, A.**, Zunino, A., Armadillo, E., & Mosegaard, K. (2021). Magnetic anomalies caused by 2D polygonal structures with uniform arbitrary polarization: new insights from analytical/numerical comparison among available algorithm formulations. *Geophysical Research Letters, 48*(7), e2020GL091732. DOI: 10.1029/2020GL091732

2. Zunino, A.*, **Ghirotto, A.***, Armadillo, E., & Fichtner, A. (2022). Hamiltonian Monte Carlo probabilistic joint inversion of 2D (2.75 D) gravity and magnetic data. *Geophysical Research Letters, 49*(20), e2022GL099789. DOI: 10.1029/2022GL099789 (*contributed equally)

3. **Ghirotto, A.**, Armadillo, E., Crispini, L., Zunino, A., Caratori Tontini, F., & Ferraccioli, F. (2023). The sub-ice structure of Mt. Melbourne Volcanic Field (Northern Victoria Land, Antarctica) uncovered through High-Resolution Aeromagnetic data. In review in *Journal of Geophysical Research: Solid Earth*.

4. Zunino, A., Gebraad, L., **Ghirotto, A.**, & Fichtner, A. (2023). HMCLab: a framework for inversion of geophysical data and numerical experiments using the Hamiltonian Monte Carlo algorithm. *arXiv* preprint 2303.10047. In prep. to be submitted to *Geophysical Journal International*.

Open-source software

The following software packages, the first one written in the Python language (Van Rossum and De Boer, 1991) and the latter three in the Julia language (Bezanson et al., 2017), are co-authored with Dr Andrea Zunino (ETH Zürich):

- pyMag2Dpoly
- Mag2Dpoly
- MagGrav2Dpoly
- GeoPolygons

For more details, click on the links above and see Appendix 3.D and 4.C.

Two additional code packages written in the Julia language, entitled *MagAnom* and *MapAppSusc*, have been developed in the context of the inversion methodology presented in section 5.4.2, but to date have not yet been released open-source.

Table of contents

List of figures

List of tables

Introduction

Since time immemorial, gravity and magnetic fields have always fascinated both scientists and common people because of their mysterious nature. In fact, people could not explain why objects were falling downward, or why some materials tended to attract or repel each other. In the latter centuries, great efforts have been made to better comprehend these fields from the mathematical and physical points of view. For the gravity field, two milestone theories were derived less than 300 years apart, i.e., Newton's law of universal gravitation and Einstein's general relativity theory (Einstein, 1916; Newton, 1687). Einstein's theory has literally shaken the foundations of classical physics, opening the way to first theorize and then verify the existence of complex phenomena in the universe related to gravity, such as black holes, gravitational lensing and gravitational waves, the latter representing a main target in theoretical physics so far. In the magnetic case, Maxwell's equations have been capable to consider the magnetic and electrical fields as two physical effects of a unique entity, i.e., the electromagnetic field, allowing for a technological progress unknown in the past of humanity (Maxwell, 1873a,b).

Despite, at a first glance, gravity and magnetic fields could appear to be very different in their physical nature, they actually are very closely related. In fact, they can be mathematically derivable from each other using Poisson's relation (Blakely, 1996, see section 3.2.3 for a better explanation), thanks to which the magnetic response of a uniformly magnetized bodies can be transformed in the so-called pseudo-gravity, i.e., the gravity field generated by the same bodies with the magnetization replaced by an identical uniform density distribution.

Moreover, the gravity and magnetic fields show some other interesting properties thanks to which they are commonly called *potential fields*. Indeed, since they are conservative and solenoid fields far enough from sources generating them (i.e., $\nabla \times \mathbf{F} = 0$ and $\nabla \cdot \mathbf{F} = 0$, where $\mathbf{F}$ indicates either the gravity or magnetic field), they admit both scalar and vector potentials. As an example, the scalar potential is required in exploration geophysics to derive the gravity and magnetic fields at any heights starting from the same dataset collected during the survey.

Particularly useful in exploration geophysics are potential fields data in the form of gravity and magnetic anomalies. They arise since the Earth is not homogeneous, that is, its physical properties, density and magnetization in our case, may vary often in a complex way (Martín-Atienza and García-Abdeslem, 1999). In order to investigate such anomalies, huge data compilations have been acquired over decades across the world in different manners, such as through ground-based and airborne surveys and, lastly, satellite investigations, proving a powerful means to help in characterizing the structure of the subsurface both at local (e.g., Hinze et al., 2013; Li and Oldenburg, 1998, 2000; Nabighian et al., 2005; Zunino et al., 2009) and continental scales, in the latter case particularly to estimate heat flux or to infer crustal thickness (e.g., Baranov et al., 2018; Li et al., 2017; Llubes et al., 2018; Martos et al., 2017; Maule et al., 2005; Milano et al., 2020; Pappa et al., 2019; Scarponi et al., 2021; van der Meijde et al., 2013). A crucial example is related to Antarctica, where gravity and magnetic anomalies data have provided scientists with a unique way to image its geological framework, owing to the thick ice sheet covering almost the entire continent and preventing direct geological observations.

However, the most informative way to extract from gravity and magnetic data useful information to characterize the density and magnetization distribution in the subsurface relies on the use of *modeling methodologies*. In this context, the advent of information technology in the '50 allowed scientists to develop a plethora of methods, exploiting different ways to parameterize geological bodies of interest in the subsurface. In fact, they may

be parameterized in a more or less complex fashion both in 2D and 3D, involving, for instance, polygons, prismatic cells, spheres and so on (Hinze et al., 2013). Unfortunately, two significant issues affect potential fields modeling, that are (i) non-uniqueness of the solution and, often, (ii) strong non-linearity of the forward problem, requiring probabilistic inversion methodologies. These weaknesses are suffered in particular by the common polygon-based parameterization approach (Rasmussen and Pedersen, 1979; Talwani and Heirtzler, 1962, 1964; Talwani et al., 1959), whose usage has remained confined to a user-subjective trial-and-error strategy, i.e., manually adjusting modeling results until the fit with observed data is good. Conversely, the equally popular prism-based parameterization approach (Banerjee and Das Gupta, 1977; Bhattacharyya, 1964; Nagy, 1966) is characterized by linear forward problem, but the non-uniqueness issue remains not addressed owing to its usage in linear deterministic inversion methods; in fact, they provide as solution just an optimal model, preventing a more informative uncertainty estimation on the model parameters typical of probabilistic approaches.

This thesis aspires to rediscover the polygon- and prism-based parameterization strategies in potential fields inverse modeling, providing at first some theoretical findings, then proposing advanced inverse methodologies aiming to help improving our capability to unravel the structure of the subsurface. The discussion, subdivided in four main parts and six chapters, is structured as follows:

- **Part I**, provides the ingredients required for the understanding of results presented in this thesis. It groups the first two chapters, that are:

  Chapter 1, showing an overview on density and magnetization properties of rocks;

  Chapter 2, defining the key concepts of model parameterization and forward and inverse problems.

- **Part II**, presents some noteworthy theoretical results related to 2D/2.75D polygonal parameterization approaches. It is composed by two chapters, namely:

  Chapter 3, discussing about theoretical and numerical results achieved from the analysis of existing formulations used to compute the magnetic field of 2D uniformly magnetized polygonal bodies. Thanks to this analysis, a new formulation recently proposed as a correction to another popular one has been demonstrated to be just its algebraic variant, saving then almost sixty years of magnetic anomaly calculations. This chapter is based on paper 1 listed at page viii;

  Chapter 4, dealing with a novel non-linear inversion method of gravity and magnetic data in case of 2D to 2.75D polygonal bodies with uniform density and magnetization, exploiting the innovative Hamiltonian Monte Carlo approach. The use of such inversion method has highlighted the still enormous potential on the polygonal parameterization in characterizing real geological bodies, beyond to enabling statistical analysis and uncertainty estimation on the model parameters. This chapter derives from paper 2 listed at page viii.

- **Part III**, shifts the focus to 3D modeling approaches. It comprises one chapter, in detail:

  Chapter 5, showing the application of a linear inversion method based on an *ad hoc* unedited version of the prism-based approach, developed for magnetic data but theoretically suitable also for gravity ones. It is turned out to be crucial to reconstruct the geophysical architecture of the Mt. Melbourne Volcanic Field, located in Northern Victoria Land (Antarctica). All results discussed in this chapter are based on paper 3 listed at page viii;

- **Part IV**, introduces the closing chapter of this thesis, namely:

Conclusions, retracing the main scientific contributions of this thesis in the field of potential fields modelling, with a focus on future developments possibly arising from this work.

All results discussed in this thesis has been achieved thanks to many open source code packages written both in the Julia (Bezanson et al., 2017) and Python languages (Van Rossum and De Boer, 1991), listed at page ix.

Part I

Basic concepts

Chapter 1

Physical properties of rocks

1.1 Introduction

Physical properties of rocks are known to strongly control the geophysical signature of a study area. Hence, their knowledge is fundamental during reduction, analysis and modeling of geophysical data to reconstruct the geological framework inferred in the subsurface. This task is often a challenge for geophysicists, since direct measures of physical properties on rock samples are usually missing as well as the knowledge of their variability in the subsurface.

In potential fields geophysics, the physical properties investigated are *density* and *magnetization* for the gravity the magnetic case, respectively. In the next sections, a presentation of their characteristics and variability on Earth materials is made to better clarify to the readers their importance in exploration geophysics.

1.2 Density

Density is the fundamental parameter controlling gravity, as it can be observed looking at classical equation for the vertical gravitational attraction $\mathbf{g}_z$ (e.g., Blakely, 1996; Hinze et al., 2013)

$$\mathbf{g}_z = G\frac{m\Delta z}{r^3} = G\rho\Delta z \quad , \tag{1.1}$$

where $G \approx 6.67 \cdot 10^{-11}\,\mathrm{Nm^2/kg^2}$ is the universal gravitational constant, m is the mass of a body, ρ its density and r and Δz are the euclidean and vertical distances between the body and the point at which gravity is observed, respectively. The density ρ is commonly measured in geophysics in $\mathrm{g/cm^3}$ in CGS units (CGSu) and $\mathrm{kg/m^3}$ in SI units (SIu), whereas g_z is instead measured in mGal in CGSu, corresponding to $10^{-2}\,\mathrm{m/s^2}$ in SIu.

The great advantage of considering density instead of mass and volume of a body in equation (1.1) is that the first is an intensive physical properties, i.e., it does not depend on the amount of matter or the size of the body, making gravity calculation easier in practice. To be more precise, it is not properly the density of a body but its density contrast with the surrounding environment to control gravity anomaly at a certain location; in exploration geophysics, such body is called anomalous and its surroundings country rocks. From this density contrast, a gravity anomaly originates, that could be positive in the case the anomalous body is denser that the country rocks and negative *vice versa*.

Gravity anomalies exist on Earth because the planet is not homogeneous in the distribution of density. Such an evidence is easy to be deduced comparing common density values of crustal rocks, that ranges from 2500 to 3000 $\mathrm{kg/m^3}$, with the mean value of the Earth planet of 5520 $\mathrm{kg/m^3}$ (Hinze et al., 2013). This big difference is due, to a first approximation, to a quite sharp change in composition moving from the surface to the nucleus, separating the interior of the planet by layers (e.g., Dziewonski and Anderson, 1981). Such layering

originated in particular during the Earth formation, when heavy elements like iron precipitated in the nucleus.

However, the target of gravity exploration is to analyze and model gravity anomaly data in order to investigate the density variability expected in the crust and lithosphere, that represent the shallower parts of Earth. Here, subsequent endo- and exo-genous geological processes occurred in million of years have produced a huge amount of lithologies whose densities, according to Schön (1996) and Hinze et al. (2013), are mainly influenced by:

- mineral composition;
- porosity;
- lithostatic pressure;
- temperature.

Mineral composition is quite stable in sedimentary rocks, since mineral components are rather limited (e.g., quartz, clay, calcite) and their densities similar. Instead, mineral constituents of crystalline lithologies, i.e., plutonic, volcanic and metamorphic rocks, are extremely variable. Plutonic and volcanic rocks show higher densities both with increasing content of heavy elements, like calcium, magnesium and iron, and with decreasing content of H_2O and SiO_2. Metamorphic rocks tend to have higher densities since they form generally at high-pressure conditions, though their mineral composition depends on the original rock types from which they derive. Looking at a crustal scale, the continental crust shows, as a first approximation, an increase of density moving toward the interface with the mantle, reflecting a change in composition of rocks from felsic to mafic, whereas oceanic crust is quite homogeneous and changes in density are mostly related to sedimentary cover thickness and crustal age.

Porosity is related to the amount of void space in a rock mass and can be distinguished in primary and secondary; the first derives from the mechanisms originating the rock, whereas

the second is triggered by physical and chemical effects affecting the rock after its formation. For what concerns the relationship between porosity and density, basically the higher the porosity the lower the density. Porosity in sedimentary rocks depends on their grain size, shape and sorting, reaching very low values in lithotypes formed by chemical precipitation like limestones. In volcanic and plutonic rocks, porosity is generally less than 1%, reaching values greater that 3% rarely. A decrease in density is observed in particular when secondary porosity takes over owing to fracturing along fault zones or similar contexts (e.g., joints, cooling cracks, etc), though the amount of density decrease depends on the void space filling, i.e., air, water, hydrocarbons. For this reason, gravity surveys are usually performed coupled with other geophysical methods (e.g., seismic investigations, magnetotelluric, etc) to characterize potential hydrocarbon and geothermal reservoirs (Hinze et al., 2013; Huenges and Ledru, 2011).

Lithostatic pressure tends to reduce porosity and thus increases density of rocks, in particular in sedimentary rocks and sediments. Nevertheless, this effect decreases with depth since compaction and lithification intervene. Moreover, pressure plays an important role in the stability fields of mineral species contained in rocks; for instance, the high pressure typical of the crustal base and of the mantle leads to the transformation of plagioclase and magmatic pyroxene in garnet and omphacite (i.e., metamorphic pyroxene), that are the main constituent minerals of eclogites, metamorphic rocks characterized by high density ($\approx 3300\,\mathrm{kg/m^3}$, e.g., Raimbourg et al., 2007).

Temperature has a minor role in controlling the density of rocks, since their volume thermal coefficient of expansion is generally low. As an example, considering values of volume thermal coefficient of expansion ranging among 20 and $40 \times 10^{-6}\,^{\circ}\mathrm{C}^{-1}$, a temperature differential of $100\,^{\circ}\mathrm{C}$ determines a density decrease of $100\,\mathrm{kg/m^3}$ solely. Nevertheless, some analytical formulations consider the temperature effect together with the lithostatic pressure to make density estimates more accurate (e.g., Ravat et al., 1999).

However, it is important to notice that a general association between lithologies and density range values is a challenging task to do in practice, since mineral composition and porosity are extremely variable parameters on rocks. As an example, Figure 1.1 provides an overview of the density range values for common lithologies based on rock several density tabulations in literature (e.g., Daly et al., 1966; Eaton and Watkins, 1967; Johnson and Olhoeft, 1984; Parasnis, 1971).

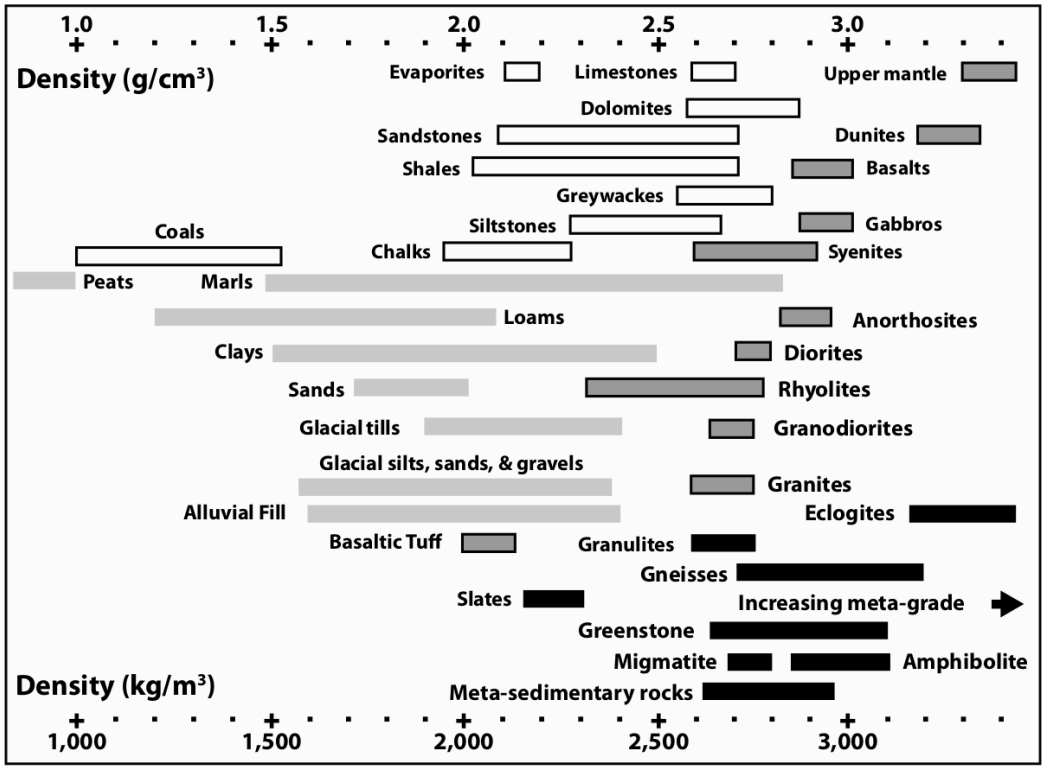

Figure 1.1 - Density ranges for common igneous (bordered grey bars), metamorphic (solid black bars) and sedimentary rock types (bordered white bars). Based on rock density tabulations from several authors (see main text). After Hinze et al. (2013).

1.3 Magnetization

1.3.1 Magnetization forms

Magnetization or polarization, commonly indicated as **M** or **J**, is an intrinsic property characteristic of materials, like density. Differently from the latter, it presents a vector nature resulting from the net magnetic effect of all the magnetic domains contained in a volume of material. Each magnetic domain is, in fact, a source of uniform magnetization, since it contains dipole magnetic moments that are all aligned in the same direction (Blakely, 1996; Hinze et al., 2013; Tarling and Hrouda, 1993).

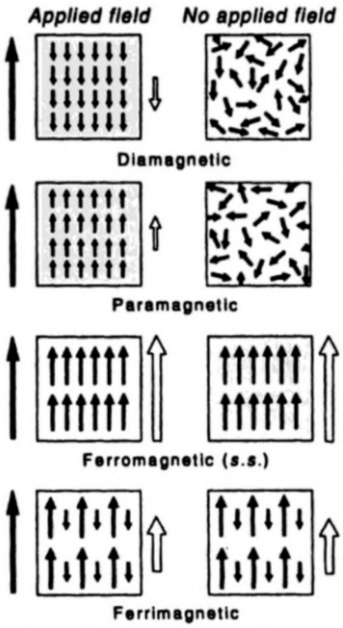

Figure 1.2 - Sketch of the magnetization forms observable on materials. After Tarling and Hrouda (1993).

According to Tarling and Hrouda (1993), Blakely (1996), Schön (1996) and Hinze et al. (2013), magnetization in substances shows different forms as a function of their composition, which are:

- diamagnetism;

- paramagnetism;
- ferromagnetism;
- ferrimagnetism.

Diamagnetism and paramagnetism occur when a material acquires a temporary polarization, called induced magnetization, upon the application of an external magnetic field, called inducing field. Such a polarization derives from an alignment of all the dipole magnetic moments to the direction of the magnetic field applied (Figure 1.2). The difference among diamagnetism and paramagnetism relies on the atomic electron shells of materials, that are complete in the first and incomplete in the second. As a result, the acquired polarization points in the opposite direction of the inducing magnetic field in the first case and in the same direction for the second one.

Ferromagnetism is shown by few materials constituted by elements belonging to the first transition series of the periodic table (e.g., iron), that are characterized by a strong magnetization called remanent. It is maintained permanently even after the removal of an external magnetic field, since all dipole magnetic moments in the magnetic domains remain aligned into its direction (Figure 1.2). Ferromagnetism disappears when a magnetized material is heated above a mineral/element-specific temperature called Curie temperature.

Similar to ferromagnetism is ferrimagnetism, the most common magnetic phenomenon shown by Earth materials. Such materials are of interest in magnetic surveys since they are remanent magnetization carriers and then source of magnetic anomalies. A substance behaves as ferrimagnetic whether adjacent magnetic domains show opposite magnetization directions, creating two oppositely magnetized lattices with different intensities (Figure 1.2). As a results, a net permanent magnetization aligned to the inducing magnetic field is retained, which disappears only in the case the material is heated above its characteristic Curie temperature as for ferromagnetic materials.

1.3.2 Induced vs remanent magnetization

Induced magnetization $\mathbf{M}_\mathrm{i}$ is the most common source of magnetization from rocks and its strength is related to the Earth's magnetic field intensity $\mathbf{H}$ by means of a dimensionless proportionality constant called magnetic susceptibility k, as follows (e.g, Blakely, 1996)

$$\mathbf{M}_\mathrm{i} = k\,\mathbf{H} = k\,\frac{\mathbf{B}}{\mu_0} \quad , \tag{1.2}$$

where $\mathbf{B}$ is the magnetic induction, μ_0 the magnetic permeability of free space and k the magnetic susceptibility, a scalar and dimensionless parameter. In SIu, $\mathbf{M}_\mathrm{i}$ is measured in $\mathrm{A/m}$, $\mathbf{B}$ is expressed in Tesla (T) or more commonly in geophysics with its sub-multiple nanoTesla (nT), μ_0 has a value of $4\pi \times 10^{-7}\,\mathrm{henry/m}$. The magnetic susceptibility k differs of a factor 4π between the CGS and SI systems (i.e., SIu $= 4\pi$ CGSu).

As clearly shown by equation (1.2), the magnetic susceptibility represents a measure of how easily a material becomes magnetized by an external magnetic field. Hence, the greater the susceptibility the higher the magnetization generated (Grant, 1985a). This parameter is commonly listed for a plenty of minerals and rock types in several geophysical compilations (e.g., Carmichael, 1982; Clark, 1983; Clark and Emerson, 1991; Dortman, 1976; Grauch and Hudson, 2011; Henkel, 1976; Hunt et al., 1995; Lindsley et al., 1966; Schön, 1996), making it easier for geophysicists to assess anomaly sources measured during a survey, for instance through magnetic modeling. Nevertheless, the interpretation of magnetic anomalies during a survey can be an hard task if other geological/geophysical information is not available, since magnetic susceptibility as density is not a rock-specific parameter (e.g., Clark and Emerson, 1991, see Figure 1.3).

Albeit susceptibility represents the principal magnetic property of diamagnetic and paramagnetic materials, it is also critical for ferrimagnetic ones. The latter, beyond to show generally higher susceptibilities values, are characterized by a remanent magnetization component $\mathbf{M}_\mathrm{r}$, leading to a resultant magnetization that is the vector sum of both induced and

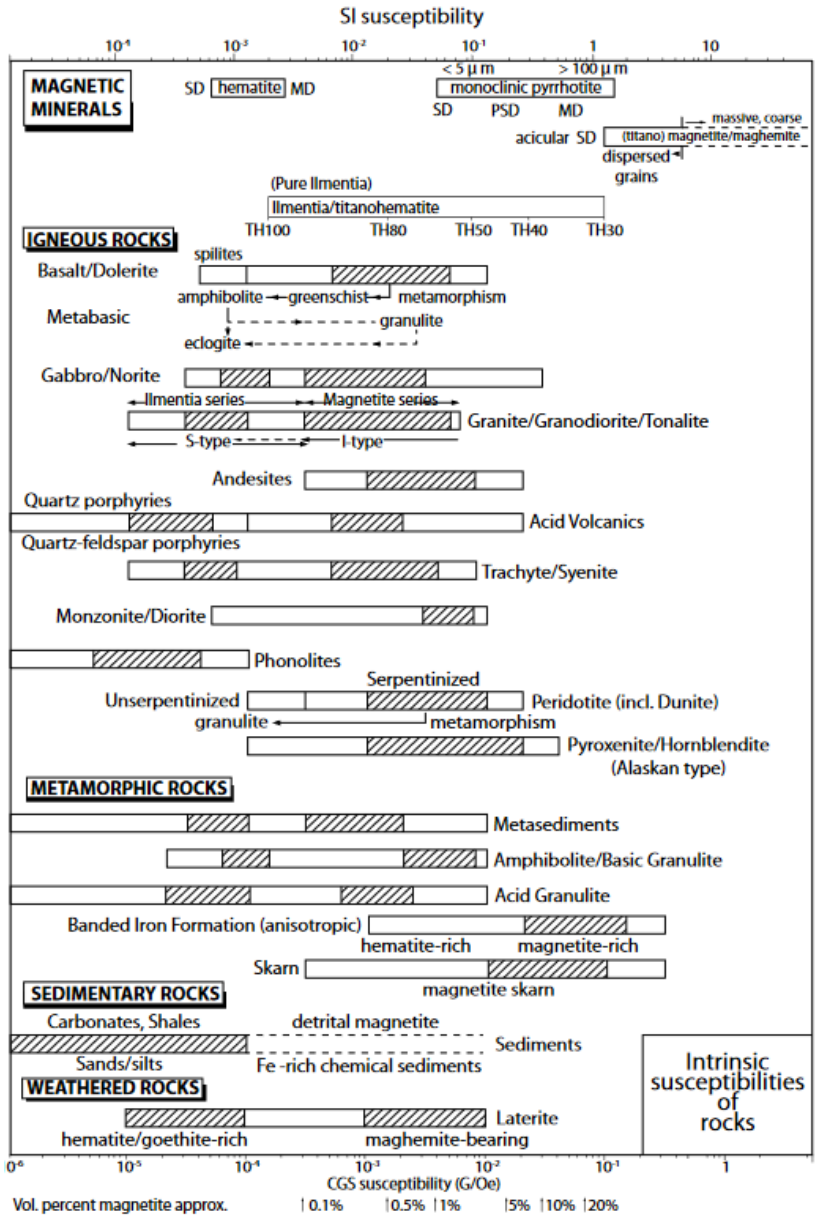

Figure 1.3 - Magnetic susceptibility ranges for common rock types. After Clark and Emerson (1991).

remanent magnetizations (Blakely, 1996). Mathematically speaking, using equation (1.2), then (in SIu)

$$\mathbf{M} = \mathbf{M}_{\mathrm{i}} + \mathbf{M}_{\mathrm{r}} = k\frac{\mathbf{B}}{\mu_0} + \mathbf{M}_{\mathrm{r}} \quad . \tag{1.3}$$

Both induced and remanent magnetizations concur to the magnetic field induction **B** as follows (in SIu)

$$\mathbf{B} = \mu_0\Big(1+k\Big)\mathbf{H} + \mathbf{M}_\mathrm{r} \quad . \tag{1.4}$$

The relative importance of induced and remanent magnetization in the overall magnetization of a material is quantified by the Koenigsberger ratio Q (Blakely, 1996)

$$\mathrm{Q} = \frac{|\mathbf{M}_\mathrm{r}|}{|\mathbf{M}_\mathrm{i}|} \quad , \tag{1.5}$$

where $\mathrm{Q} > 1$ indicates dominance of remanent magnetization on induced one and instead $\mathrm{Q} < 1$ *vice versa*. Such a parameter is quite important in modeling of magnetic anomaly data, since it allows in several geological contexts to limit the magnetization components of rocks to just one, usually induced magnetization, simplifying magnetic calculations and interpretation of results. Some considerations about the relationship between Koenigberger ratio Q and rock types are given in Figure 1.4.

At this point of the discussion, it should be noticed that the term "remanent magnetization" is quite generic and needs some clarifications. Commonly, remanent magnetization is indicated as natural remanent magnetization (NRM) and it represents the sum of both primary and secondary magnetization components (Hinze et al., 2013; Schön, 1996).

Primary magnetization is acquired by rocks and sediments during their formation and deposition, respectively. The most intense type is the thermo-remanent magnetization (TRM), gained by igneous rocks after cooling below Curie temperatures, that vary as a function of their ferrimagnetic mineral content and grain size (Hinze et al., 2013; Schön, 1996). A less intense primary magnetization occurring in sedimentary rocks and sediments is the detrital remanent magnetization (DRM), that is related to the preferential orientation of ferrimagnetic grains according to the Earth's magnetic field (Hinze et al., 2013; Schön, 1996; Tarling and Hrouda, 1993). Another minor primary magnetization is the chemical

remanent magnetization (CRM), that is similar to TRM but occurs in ferrimagnetic grains while growing without changes in temperature (Hinze et al., 2013; Schön, 1996; Tarling and Hrouda, 1993). An example is the CRM derived from the grow of magnetite grains in peridotites during serpentinization (e.g., Saad, 1969a,b).

Secondary magnetization originates after rocks formation and sediments deposition. The main type is the viscous remanent magnetization (VRM), caused by the low and progressive rotation of magnetic domains contained in rocks into the ambient field, cancelling out previous remanent magnetization components (Hinze et al., 2013; Tarling and Hrouda, 1993). Since the time required to acquire a consistent VRM is remarkably long, in particular in fine-grained rocks, its effect can be considered often negligible also for rocks millions of years old (Hinze et al., 2013).

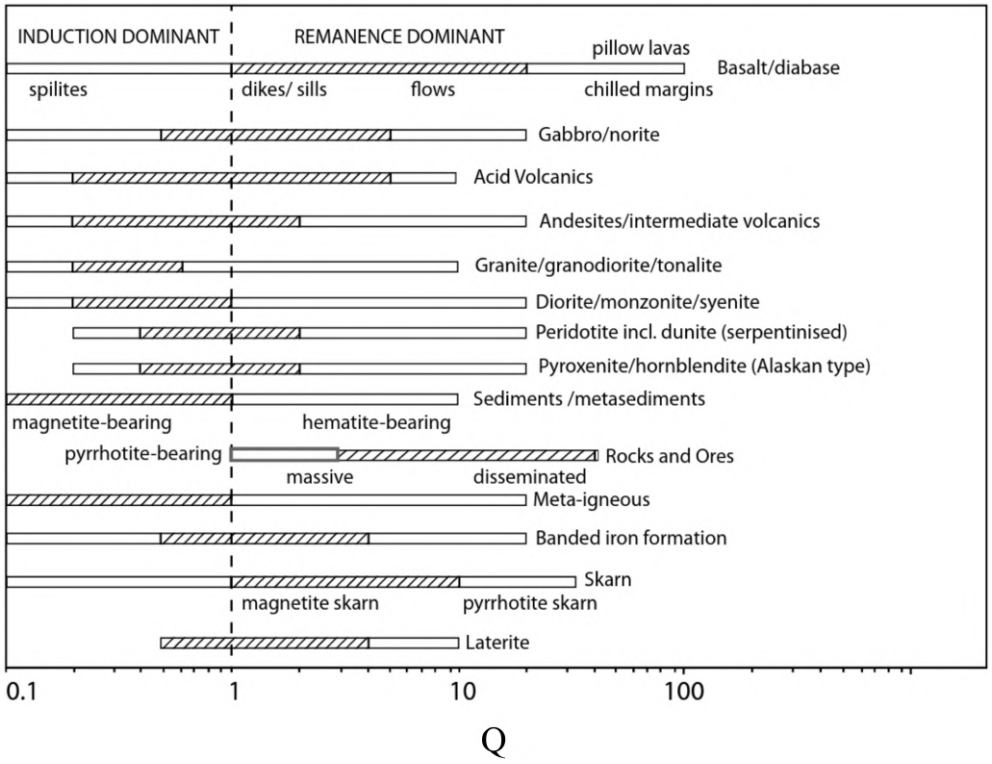

Figure 1.4 - Ranges of the Koenigsberger ratio Q for various rock types. Diagonally ruled segments indicate ranges typically observed in nature. After Clark and Emerson (1991).

1.3.3 Magnetization of rocks

The primary rock-forming minerals contained in Earth rocks are mainly diamagnetic and paramagnetic (Schön, 1996), hence rock magnetization is strongly controlled by the content of ferrimagnetic minerals. Typical ferrimagnetic minerals contained in rocks belong to the ternary system FeO-Fe_2O_3-TiO_2 and can be subdivided in the (i) titanomagnetite and (ii) titanohematite mineral series (see Figure 1.5; Hinze et al., 2013).

The first series concerns the solid solution between the mineral species ulvöspinel (Fe_2TiO_4) and magnetite (FeO-Fe_2O_3), that are the most magnetically significant minerals (Blakely, 1996). The solid solution tends to exsolve after cooling of magmatic fuses under normal geological condition in magnetite and both ilmenite ($FeTiO_3$), that is paramagnetic, and ulvöspinel, at ambient conditions. An interesting properties of this series is related to its Curie temperature, showing a decrease with increasing content of titanium. As an example, the titanium content in magnetite is capable to widen its Curie temperature in a range between 500 and 560 °C (Hinze et al., 2013).

The second series refers to the solid solution between the two end-members ilmenite and hematite (Fe_2O_3), which are not ferrimagnetic. In fact, generally the solid solution has ferrimagnetic properties whether the titanium content ranges between 45 and 90%, occurring in the case of rapid cooling of rocks. An interesting ferrimagnetic mineral of this series is maghemite (γFe_2O_3), that forms under low temperature oxidation ($< 200\,°C$), whose solid solutions with magnetite show magnetic properties similar to it (Hinze et al., 2013).

Other important ferrimagnetic minerals are some species of iron sulfides, in particular pyrrhotite (Fe_7S_8) and greigite (Fe_3S_4). Pyrrhotite has a Curie temperature of 320°C and can be found in basic volcanic rocks (Whitney and Stormer, 1983) and in low-grade metamorphic zones (Rochette, 1987), whereas Greigite Curie temperature is 350°C and it typically occurs in organic-bearing lakes and, also, marine sediments at depth greater than a few meters (Tar-

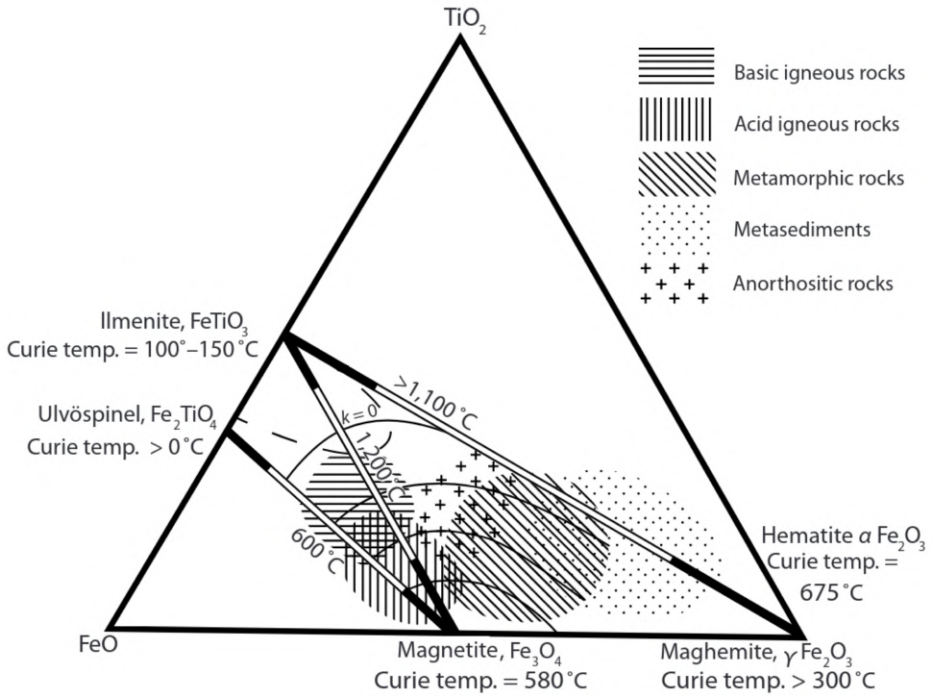

Figure 1.5 - Overview of magnetic properties and compositions of minerals belonging to the FeO-TiO_2-Fe_2O_3 ternary system. Ferrimagnetic series are shown as bars, whose solid parts indicate complete solubility of end-members at room temperature. The white parts of bars represent known solubility gaps at indicated temperatures. The magnetic susceptibility increase toward the base of the ternary system, as shown by contour lines. Mineral composition of igneous, metamorphic and sedimentary rocks tend to cluster in some specific regions of the ternary system, albeit they often overlap. After Grant (1985a).

ling and Hrouda, 1993). Both the mineral species can also be produced by sulfate-reducing bacteria (Hinze et al., 2013).

Since all the basic concepts related to magnetism have just been clarified, now it is the time to take a closer look at the actual magnetization of the sedimentary, igneous, and metamorphic rocks, keeping in mind that, as already explained, an exhaustive association between magnetization and rock types is hard to be found.

The magnetization of igneous rocks depends on their composition, oxidation state, hydrothermal alteration and metamorphism (Hinze et al., 2013), and the complex relation among these factors makes further difficult to define a general correlation between rocks types and magnetic properties. From a compositional point of view, these rocks can be

primarily distinguished in (i) felsic, (ii) mafic and (iii) ultramafic. Felsic rocks are the main constituent of upper crust, mafic rocks of both lower continental and oceanic crusts and ultramafic rocks dominate in the upper mantle. Hence, a large part of the lithosphere, namely the shallower portion cooler that the Curie temperatures characteristic of its ferrimagnetic minerals, is magnetized. At a first approximation, felsic rocks are generally characterized by lower contents of ferrimagnetic minerals as iron and titanium oxides with respect to mafic ones. Nevertheless, titanomagnetite tends to be richer in titanium in the latter rocks, resulting in weaker magnetizations and Curie temperatures (Hinze et al., 2013). The rate of cooling also controls, as already explained, the stability fields of ferrimagnetic solid solutions. Fast cooling leads to avoid exsolution of solid solutions resulting in lower magnetic susceptibilities of minerals and Curie temperatures, albeit the fine-grained crystallization of minerals tends to increase the Koenigsberger ratio Q. Alteration by oxidation is recognized to break down magnetization of rocks thanks to the transformation of original igneous ferromagnetic minerals to diamagnetic and paramagnetic species. This phenomenon affects mafic volcanic rocks in particular at subaerial conditions. Hydrothermal alteration commonly affects igneous rocks in volcanic environment, attenuating their strong magnetization owing to the substitution of original magmatic-source ferrimagnetic minerals with non-ferrimagnetic species (e.g., Bouligand et al., 2014; Finn et al., 2022, 2007; Finn and Morgan, 2002).

For what concern metamorphism, it may significantly increase magnetization of rocks. Examples are the contact metamorphism caused by high-temperature fluids from a plutonic intrusion and the serpentinization of ultramafic rocks, the latter inducing the formation of magnetite with a stable CRM as above mentioned (Saad, 1969a,b). However, the literature shows opposite results about the change in magnetic properties with increasing metamorphism grade, making it difficult to derive exhaustive considerations (e.g., Grant, 1985a,b; Haggerty, 1979).

As regards sedimentary rocks, they are significantly less magnetic that igneous rocks and the most abundant magnetic carrier is magnetite, although titanohematite may be dominant in some lithologies (e.g., Reynolds, 1977). However, their magnetic properties depend on the provenance of the sediments; for example, sediments derived from erosion of igneous rocks will lead to more magnetic sedimentary rocks with respect to sediments from detriment of other sedimentary rocks. In addition, weathering of ferrimagnetic minerals during and after erosion of rock sources further decreases the magnetization of forming sedimentary rocks. In contrast to common sedimentary rocks, Archean and Early Proterozoic iron formations, also called banded iron formations (BIF), are constituted by significant quantities of magnetite (> 10 % by weight) making them among the most magnetic rocks (Bath, 1962; Jahren, 1963).

Chapter 2

Potential fields modeling theory

2.1 Introduction

Modeling of gravity and magnetic data plays a fundamental role to appraise the density and magnetization variability expected in the subsurface, and then to unravel its geological architecture. At this point, the first question that comes to mind is: "what does modeling in geophysics actually mean?". Basically, modeling represents a procedure to estimate physical parameters of interest starting from measured geophysical data and independent geological and geophysical information (Blakely, 1996). In jargon, the physical parameters of interest are called model parameters and in gravity and magnetic modeling are generally the density and the susceptibility/magnetization, respectively, of buried geological bodies and/or their geometries. The geophysical data are observable parameters measured at certain locations in space, in our case the gravity and magnetic anomalies observed during a survey. The geological and geophysical information obtained independently from our survey is so-called *a priori* (or prior) information and contributes to a better estimation of the model parameters. An example of prior information is the direct measurement of density and magnetic susceptibility from rock samples, or their inference from field surface geological information, and so on.

Now, it becomes clear that in order to estimate the model parameters from the observable data, a relationship between them should exists. This relationship is a mathematical formalism based on the theory describing the geophysical problem we are facing, that generally is well known. In our case, these theories allows us to calculate the gravity and magnetic responses at given locations of a certain density and magnetization distribution in the subsurface. Nevertheless, they are not unique but depend on the way the subsurface is parameterized, that is on the particular choice of model parameters we are interested in. This phase, called model parameterization, is crucial as it conditions the subsequent modeling stage.

After this brief premise, in the following sections we provide a clear explanation about what modeling means in geophysics, introducing the key definitions of *model parameterization*, *forward problem* and *inverse problem*.

2.2 Model parameterization

With the term model parameterization, we mean the starting phase in geophysical modeling required to define the minimal set of model parameters whose values completely characterize the geophysical problem under study (Tarantola, 2005). The geophysical problem depends on the target of our study, ranging from local scale studies, like the characterization of an ore deposit or a geothermal system, to regional scale investigations addressing the crustal and lithospheric structure of a continent.

Such parameterization can be either continuous or discrete, depending on the way we would like to consider our geophysical problem. We are interested to the second one, since our purpose is to discretize the continuous reality surrounding us so that any kind of calculation can be managed by a computer. The way we perform this discretization depends on the geological "object" we would like to model and the related model parameters we are interest to estimate. For example, an horizontal dike could be parameterized though a prismatic body with vertical polygonal cross-section, but model parameters would be either its physical

properties (i.e., density and/or magnetization) or the shape of its polygonal cross-section (its vertices to be precise), depending on what we already know about our geophysical problem and what instead we do not know and then we would like to estimate.

Using the above mentioned polygon-based model parameterization, which has become very popular in potential fields geophysics since the late '50 (e.g., Talwani et al. (1959) and Talwani and Heirtzler (1962) for the gravity and magnetic case respectively), the gravity and magnetic responses of a 3D geological object can be calculated through its polygonal section, taken along a 2D profile perpendicular to its elongation, that can be both finite and infinite. Among its merits, this approach allows us to (i) parameterize a wide range of geological scenarios, (ii) manage modeled bodies in a simple way compared to other parameterization types, (iii) decrease the amount of model parameters and (iv) achieve model in which density and/or magnetization contrasts are better geometrically defined. Nevertheless, such approach is not appropriate to be used were physical properties of the modelled objects are inferred to vary in a complex 3D way or when their shape do not have a quite regular polygonal section. In addition, the mathematical formulae relating measured data and model parameters show a strong non-linearity both for the gravity and the magnetic case, discouraging an exploitation for inverse methods despite its considerable strengths. As mentioned in the introduction of this thesis, such limitation has been overcome developing an innovative inversion method involving this type of model parameterization, that is presented in chapter 4 we present .

Another widespread parameterization approach proposed by Bhattacharyya (1964) and Nagy (1966) for the magnetic and gravity case, respectively, involves a discretization of the target geological object by prismatic cells characterized by homogeneous physical properties, the latter representing the model parameters. The geological object can be discretized both in 2D and 3D; in the 2D case, the parameterization is performed along a profile representing a cross-section of the geological object, and each prismatic cell is infinitely extended in the

direction perpendicular to the profile direction; in the 3D case, the parameterization is figured out by finitely extended prismatic cells arranged in all directions, making the approach more suitable in case of complex 3D density / magnetization distributions. The great advantage of the cell-based approach is that the relation between data and model parameters is linear both for the gravity and the magnetic case, whereas the disadvantage is to have a greater number of model parameters to estimate, particularly for high-resolution discretization involving smaller prismatic cells. This aspect becomes more clear looking at Figure 2.1, showing a section of a geological scenario involving a cubical density anomaly buried in the subsurface, parameterized through the above discussed 2D polygon- and cell-based approaches.

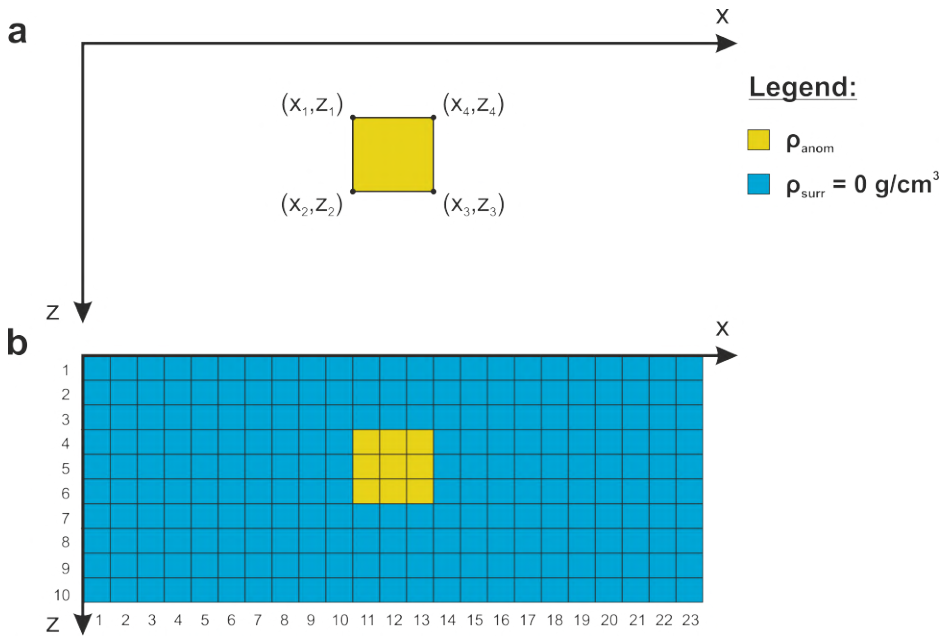

Figure 2.1 - (a) Polygon-based parameterization approach. (b) Prism-based parameterization approach.

Since the densities of the anomalous body and of the surroundings are ρ_2 and ρ_1, respectively, then the density contrast due to the anomalous body is $\rho_{\text{anom}} = \rho_2 - \rho_1$, with the surroundings sets to 0 (i.e., $\rho_{\text{surr}} = \rho_1 - \rho_1 = 0$ g/cm^3). Then, we have a total amount of $23 \times 10 = 230$ model parameters (i.e., 230 density contrasts) for the 2D cell-based approach, whereas either 1 or 4 for the polygon-based one, depending on the model parameters chosen (i.e., density

or vertices of the polygon). Considering a 3D cell-based approach, the number of model parameters should be even greater (i.e., $23 \times 10 \times n$, where n is related to the third dimension). Nevertheless, the considerable strengths above explained of this parameterization type have been exploited in sub-section 5.4.2 to develop an *ad hoc* inversion method, whose results allowed us to reconstruct the internal framework on the Mount Melbourne Volcanic Field, located in Antarctica (see chapter 5).

In the latter decades, several other parameterization approaches have been developed in order to allow researchers to model the majority of geological scenarios. In fact, beyond to the simpler cell- and prism-based parameterization approaches, the rapid gain in available computing resources allowed scientists to develop ever more accurate parameterization strategies. An example is the polyhedron-based one, that represents the current frontier to develop innovative inversion methods able to characterize those geological scenarios in which the physical properties are expected to vary in a complex 3D way (e.g., Ren et al., 2020, 2022, and references therein).

As a final remark, it is crucial to notice that the choice of the proper model parameterization closely depends on the geophysical problem we would like to tackle, on the accuracy desired and the computational resources available, making the parameterization phase probably the most tricky in geophysical modeling.

2.3 Forward problem

From a mathematical viewpoint, to solve a *forward problem* means to predict the data parameters $\mathbf{d}$ that would correspond to a given model $\mathbf{m}$ (Menke, 2018; Tarantola, 2005), as described by the following relation (2.1)

$$\mathbf{d} = \mathbf{g}(\mathbf{m}) \quad , \tag{2.1}$$

that is a short notation for a set of equation $d^i = g^i(m^1, m^2, \ldots)(i = 1, 2, \ldots)$, where $\mathbf{g}(\cdot)$ is called forward operator and $(m^1, m^2, \ldots)$ is a particular set of model parameters, depending on the type of model parameterization performed. The operator $\mathbf{g}(\cdot)$ represents the mathematical theory linking our model to its calculated response. In case the relationship between data and model parameters is linear, then equation (2.1) reduces to

$$\mathbf{d} = \mathbf{G}\,\mathbf{m} \quad , \tag{2.2}$$

where $\mathbf{d}$ and $\mathbf{m}$ are vectors and $\mathbf{G}$ the forward matrix.

From a theoretical viewpoint, $\mathbf{d}$ and $\mathbf{m}$ represent points in two separate abstract spaces, called *data space* and *model space*, and their components $(d^1, d^2, d^3, \ldots)$ and $(m^1, m^2, \ldots)$ the coordinates of these points in their respective spaces (Tarantola, 2005). These concepts will come in handy to better understand some results presented throughout this thesis.

At this point, some clarifications need to be made about the meaning of *forward problem*. In fact, beyond to the definition provided above from Tarantola (2005) (that will be followed hereinafter), there is another common meaning well exemplified by Blakely (1996). For this purpose, let us imagine to perform a gravity and magnetic survey to characterize the unknown density and magnetization distribution in the subsurface of a study area, that has been properly parameterized. Since the target is to estimate these distributions, we can start to propose an initial model for them and calculate the related gravity and magnetic effects. Obviously, this initial model will be less or more accurate as a function of the *a priori* knowledge available on the subsurface geological framework. Then, the next steps are to tentatively adjust this model in order to improve the fit between observed and calculated data. We refer to such a procedure as *forward modeling*. The typical workflow characterizing it is depicted by the diagram of Figure 2.2.

In this regard, it is important to notice that models achieved through this procedure are not unique. It means that, particularly in more complex geological scenarios, several

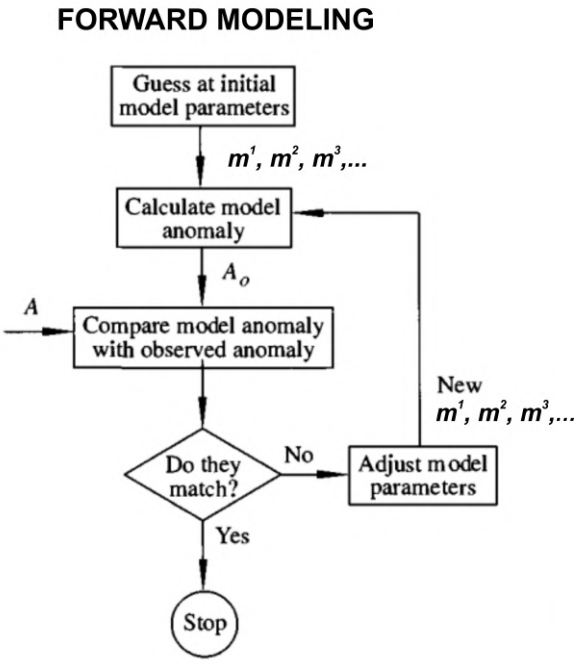

Figure 2.2 - Sketch showing the procedure phases performed in a forward modeling approach. Modified from Blakely (1996).

different models are equally capable of explaining the measured data. Such a phenomenon can be a great limitation particularly when a little prior information are available to constrain modeling results. For this reason, the inverse problem comes into play to tackle geophysical modeling from another perspective, as explained in the following section 2.4.

2.4 Inverse problem

Let us imagine we are in the same situation described in the previous section, in which we have collected a gravity and magnetic dataset in a survey area with the aim of characterizing the unknown density and magnetization distribution expected in the subsurface.

Then, instead of proposing a starting initial model and progressively modify it through a trial-and-error approach, our problem might be to calculate directly the model parameters of interest from the observable parameters, i.e., the gravity and magnetic data collected,

exploiting the forward problem just defined. According to the nomenclature proposed by Tarantola (2005), such a problem is called *inverse problem* and the related procedure *inverse modeling*.

2.4.1 Why is the inverse problem so hard to solve?

Put this way, the problem seems simple to deal with. In fact, one could imagine to solve the inverse problem simply inverting equation (2.1), that is finding the inverse of the forward operator $\mathbf{g}^{-1}$, as follows

$$\mathbf{m} = \mathbf{g}^{-1}(\mathbf{d}) \quad , \tag{2.3}$$

or in the linear case

$$\mathbf{m} = \mathbf{G}^{-1}\mathbf{d} \quad . \tag{2.4}$$

Unfortunately, the forward operator may not be invertible, and then equations (2.3)-(2.4) would not exist.

Looking at the linear case in equation (2.4) for simplicity, the matrix $\mathbf{G}^{-1}$ exists if and only if (i) $\det(\mathbf{G}) \neq 0$ and (ii) $\mathbf{G}$ is square. In this situation, the matrix $\mathbf{G}$ shows only a trivial null space, that is $\mathbf{G}\mathbf{m}_0 = \mathbf{0}$ if and only if $\mathbf{m}_0 = \mathbf{0}$; as a result, the solution $\mathbf{m}$ would be unique. It should be noticed that $\mathbf{G}$ is usually non square, since the number of data and model parameters might not match ($\mathbf{G}$ is a matrix $m \times n$, where m and n are the lengths of the vectors $\mathbf{d}$ and $\mathbf{m}$, respectively). Moreover, $\det(\mathbf{G}) = 0$ implies that $\text{rank}(\mathbf{G}) \neq n$, thus theoretically infinite vectors $\mathbf{m}_0$ would lie in the null space of $\mathbf{G}$ such that $\mathbf{G}\mathbf{m}_0 = \mathbf{0}$. This means that any linear combinations of $\mathbf{m}_0$ can be added to a certain model $\mathbf{m}$ that satisfies equation (2.2) without changing the values of $\mathbf{d}$, resulting in infinite possible solution models

m. As we have already mentioned, potential fields modeling methods can severely suffer from this issue.

In addition, the inverse problem is unstable, since a small change in measurements **d** can lead to a tremendous change in the estimated model **m** (Aster et al., 2005). In this purpose, the noise ε plays an important role because it makes small and uncontrollable changes to the data. Basically, noise is caused by imprecise instrument readings or numerical round-off, so it is a random phenomenon which cannot be exactly modeled. Hence, measured data **d** should be separated in hypothetical perfect data $\mathbf{d}_{\text{true}}$ plus the noise effect ε, i.e.,

$$\begin{aligned} \mathbf{d} &= \mathbf{d}_{\text{true}} + \varepsilon = \\ &= \mathbf{g}(\mathbf{m}_{\text{true}}) + \varepsilon \quad , \end{aligned} \tag{2.5}$$

where $\mathbf{d}_{\text{true}}$ should be reproduced through the forward operator $\mathbf{g}(\cdot)$ from actual model parameters $\mathbf{m}_{\text{true}}$. Another source of error relies on an approximate mathematical theory of the problem, that is described by $\mathbf{g}(\cdot)$. Owing to noise in the data and approximate mathematical theory, **m** could either not exist or be completely no-sense (Aster et al., 2005). However, the inversion process can be "stabilized" by means of *regularization*, for instance by adding prior information to constrain the estimation of model parameters. This procedure can be done with different approaches, as explained in section 2.4.2.

To summarize, the solution **m** of an inverse problem could not exist, or could not be unique in the case it exists, and it is usually unstable. Such characteristics make the inverse problem *ill-conditioned* following the definition coined by Hadamard (1902).

2.4.2 How to tackle an inverse problem

After the general overview provided above, aiming to make the readers clear how difficult may be to tackle an inverse problem, the question that spontaneously arises is: "how can an inverse problem be solved?". To this end, let us introduce a quantity called *data residuals*, defined as (e.g., Aster et al., 2005)

$$\mathbf{r} = \mathbf{d} - \mathbf{G}\,\mathbf{m} = \mathbf{d} - \mathbf{d}_{\text{pre}} \quad , \tag{2.6}$$

providing a measure of the misfit between observed data and data predicted (i.e., calculated) for a certain model $\mathbf{m}$. For this purpose, let us define the concept of *norm*. The norm $\|\mathbf{r}\|$ for some powers of n, indicated with the symbol L_n, is defined as (e.g., Menke, 2018)

$$\begin{aligned} L_1 \text{ norm} &= \|\mathbf{r}\|_1 = \left[\sum_i |r^i|^1\right] \quad , \\ L_2 \text{ norm} &= \|\mathbf{r}\|_2 = \left[\sum_i |r^i|^2\right]^{1/2} \quad , \\ &\vdots \\ L_n \text{ norm} &= \|\mathbf{r}\|_n = \left[\sum_i |r^i|^n\right]^{1/n} \quad . \end{aligned} \tag{2.7}$$

The aim of the inverse problem is to minimize the residual (or misfit) function $\|\mathbf{r}\|_n$, since it represents an objective function capable of providing a measure of the distance between observed and calculated data (Aster et al., 2005; Menke, 2018; Tarantola, 2005). Among all, the L_2 norm is of special interest for its geometrical and statistical meanings (Menke, 2018; Tarantola, 2005). From a geometrical viewpoint, it represents the euclidean distance between observed and calculated data, whereas from a statistical viewpoint reflects the normal (i.e., Gaussian) distribution characterizing the residuals. Such viewpoints define two "school of thought" and related approaches to tackle an inverse problem, that are the *deterministic* and

probabilistic one, respectively. The aim of the deterministic approach is to provide a single "optimal solution" to the inverse problem (e.g., Aster et al., 2005; Menke, 2018), whereas the probabilistic one to retrieve/characterize the *a posteriori* (or posterior) probability density function (PDF) of the model parameters, upon which uncertainty estimations and statistical analyses on the model parameters can be performed (e.g., Tarantola, 2005). In is interesting to notice that, as shown in the next sub-section 2.4.2.1, the deterministic and probabilistic approaches match in case the forward problem is linear and the residuals Gaussian. The two approaches are described in details below, considering the case the forward problem is either linear or non-linear.

2.4.2.1 Linear case

Starting from the definition of the data residuals in equation (2.6), now our purpose is to find the solution $\mathbf{m}$ minimizing its L_2 norm. In the case of a linear inverse problem and Gaussian residuals (Figure 2.3), $\|\mathbf{r}\|_2$ is defined as follows

$$\|\mathbf{r}\|_2 = \left[(\mathbf{d}-\mathbf{G}\,\mathbf{m})^T\ \mathbf{C}_\mathrm{D}^{-1}\ (\mathbf{d}-\mathbf{G}\,\mathbf{m})\right]^{1/2} \quad , \tag{2.8}$$

where the letter T stands for transpose and $\mathbf{C}_\mathrm{D}$ represents the matrix covariance of the observed data, indicating their degree of correlation. By definition, this matrix must be symmetric and positive semi-definite.

With these concepts in mind, in the next paragraphs we show how to solve the linear inverse problem both from a deterministic and a probabilistic viewpoint.

Deterministic approach Following our aim to minimize the misfit function $\|\mathbf{r}\|_2$, we can start squaring it to simplify the calculations, obtaining

$$\|\mathbf{r}\|_2^2 = (\mathbf{d}-\mathbf{G}\,\mathbf{m})^T\ \mathbf{C}_\mathrm{D}^{-1}\ (\mathbf{d}-\mathbf{G}\,\mathbf{m}) \quad . \tag{2.9}$$

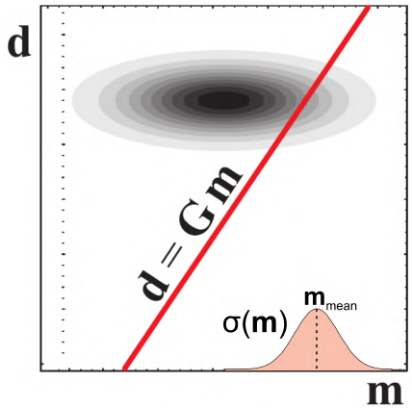

Figure 2.3 - Sketch representing an inverse problem characterized by forward problem $\mathbf{d} = \mathbf{G}\mathbf{m}$ linear and posterior PDF of the model parameters $\sigma(\mathbf{m})$ Gaussian. The mean model from the probabilistic viewpoint is nothing more that the optimal model from the deterministic one. Modified from Tarantola (2005).

Renaming $\|\mathbf{r}\|_2^2$ as $R(\mathbf{m})$, in order to highlight the dependency of the misfit function from the model parameters, and doing some calculations, equation (2.9) becomes

$$R(\mathbf{m}) = \mathbf{m}^T \mathbf{G}^T \mathbf{C}_\mathrm{D}^{-1} \mathbf{G}\mathbf{m} + \mathbf{d}^T \mathbf{C}_\mathrm{D}^{-1} \mathbf{d} - \mathbf{d}^T \mathbf{C}_\mathrm{D}^{-1} \mathbf{G}\mathbf{m} - \mathbf{G}^T \mathbf{m}^T \mathbf{C}_\mathrm{D}^{-1} \mathbf{d} \quad . \tag{2.10}$$

Now, the right way to proceed is to set the derivative of the misfit function $R(\mathbf{m})$ with respect to $\mathbf{m}^T$ (for convenience) to zero (e.g., Menke, 2018), as

$$\frac{\partial R}{\partial \mathbf{m}^T} = 0 \iff \mathbf{G}^T \mathbf{C}_\mathrm{D}^{-1} \mathbf{G}\mathbf{m} - \mathbf{G}^T \mathbf{C}_\mathrm{D}^{-1} \mathbf{d} = 0 \quad , \tag{2.11}$$

and by manipulating equation (2.11), we can finally derive the analytical expression for $\mathbf{m}$

$$\mathbf{m} = \left(\mathbf{G}^T \mathbf{C}_\mathrm{D}^{-1} \mathbf{G}\right)^{-1} \left(\mathbf{G}^T \mathbf{C}_\mathrm{D}^{-1} \mathbf{d}\right) \quad . \tag{2.12}$$

Now, it should be noticed that the above solution can be extremely biased with respect to $\mathbf{m}_\mathrm{true}$ (Aster et al., 2005) due to the non-uniqueness and instability issues arising in particular in potential fields inverse problems. Hence, regularization can help to constrain the inversion

process toward a solution closer to the expected $\mathbf{m}_{\text{true}}$. Different approaches exist, but the common *modus operandi* is to find the solution $\mathbf{m}$ minimising not only the misfit function $R(\mathbf{m})$, but

$$\text{argmin} \quad R(\mathbf{m}) + \alpha \|T(\mathbf{m})\|_2^2 \quad , \tag{2.13}$$

where $T(\mathbf{m})$ is the regularization term and α a constant that sizes its "weight". For instance, in the common *Tikhonov* regularization $T(\mathbf{m})$ is represented by the model parameters $\mathbf{m}$ themselves (e.g., Aster et al., 2005). Another interesting approach is to consider as regularization term the vector $(\mathbf{m} - \mathbf{m}_{\text{prior}})$, where $\mathbf{m}_{\text{prior}}$ reflects our *a priori* knowledge on the model parameters (Tarantola, 2005). Such approach is particularly common in the probabilistic approach to inverse problems, as we discuss in the next paragraph.

Probabilistic approach From a probabilistic viewpoint, an inverse problem can be written in terms of PDFs, able to deal with measurement uncertainties and modelization imperfections and, in general, to describe a "state of information". According to this approach and assuming Gaussian PDFs, the inverse problem can be set up as follows

$$\begin{aligned} \sigma(\mathbf{m}) &= k L(\mathbf{m}) \rho(\mathbf{m}) = \\ &= k \exp(-R(\mathbf{m})) \rho(\mathbf{m}) = \\ &= k \exp(-S(\mathbf{m})) \quad , \end{aligned} \tag{2.14}$$

where $\sigma(\mathbf{m})$ is the posterior PDF of the model parameters we want to characterize, k is a constant, $\exp(-R(\mathbf{m}))$ is the *Likelihood* term, i.e., the PDF related to the L_2 norm of the residuals, and $\rho(\mathbf{m})$ the PDF describing our *a priori* knowledge on the model parameters (Figure 2.3). Hence, $\sigma(\mathbf{m})$ can be interpreted as a product between the states of information

related to the theory behind our problem and the model parameters, following the theoretical framework derived by Mosegaard and Tarantola (2002) starting from the probability theory developed by Bayes (1763).

Since in a product between exponentials with the same base the exponents add up, we can group together the Likelihood and the prior PDFs in the new term $\exp(-S(\mathbf{m}))$, with $S(\mathbf{m})$ defined in matrix form as (Tarantola, 2005)

$$\begin{aligned} S(\mathbf{m}) &= \frac{1}{2}(\mathbf{d}-\mathbf{G}\,\mathbf{m})^T\,\mathbf{C}_\mathrm{D}^{-1}\,(\mathbf{d}-\mathbf{G}\,\mathbf{m}) + \left(\mathbf{m}-\mathbf{m}_\mathrm{prior}\right)^T\,\mathbf{C}_\mathrm{M}^{-1}\,\left(\mathbf{m}-\mathbf{m}_\mathrm{prior}\right) \iff \\ 2\,S(\mathbf{m}) &= \mathbf{m}^T\,\mathbf{G}^T\,\mathbf{C}_\mathrm{D}^{-1}\,\mathbf{G}\,\mathbf{m} + \mathbf{d}^T\,\mathbf{C}_\mathrm{D}^{-1}\,\mathbf{d} - \mathbf{d}^T\,\mathbf{C}_\mathrm{D}^{-1}\,\mathbf{G}\,\mathbf{m} - \mathbf{G}^T\,\mathbf{m}^T\,\mathbf{C}_\mathrm{D}^{-1}\,\mathbf{d} + \\ &+ \mathbf{m}^T\,\mathbf{C}_\mathrm{M}^{-1}\,\mathbf{m} - \mathbf{m}^T\,\mathbf{C}_\mathrm{M}^{-1}\,\mathbf{m}_\mathrm{prior} \quad , \end{aligned} \tag{2.15}$$

where $\mathbf{C}_\mathrm{M}$ represents the matrix covariance of the *a priori* model parameters, indicating their degree of correlation. By definition, as $\mathbf{C}_\mathrm{D}$ this matrix must be symmetric and positive semi-definite. For the sake of clarity, we consider twice the term $S(\mathbf{m})$, as this manipulation is analogous to the square elevation of $\|\mathbf{r}\|_2$ leading to the misfit function $R(\mathbf{m})$ shown in paragraph 2.4.2.1.

Now, what we would like to do is to find the $\mathbf{m}$ that maximize $\sigma(\mathbf{m})$, namely the model $\mathbf{m}$ with the highest probability density (given $\mathbf{d}$ observations). To maximize $\sigma(\mathbf{m})$, it should be minimized $S(\mathbf{m})$, analogously to the previous paragraph "Linear case - Deterministic approach",

$$\frac{\partial S}{\partial \mathbf{m}^T} = 0 \iff \mathbf{G}^T\,\mathbf{C}_\mathrm{D}^{-1}\,\mathbf{G}\,\mathbf{m} - \mathbf{G}^T\,\mathbf{C}_\mathrm{D}^{-1}\,\mathbf{d} + \mathbf{C}_\mathrm{M}^{-1}\,\mathbf{m} - \mathbf{C}_\mathrm{M}^{-1}\,\mathbf{m}_\mathrm{prior} = 0 \quad , \tag{2.16}$$

and finally, the expression for $\mathbf{m}$ is

$$\mathbf{m} = \left(\mathbf{G}^T \mathbf{C}_\mathrm{D}^{-1} \mathbf{G} + \mathbf{C}_\mathrm{M}^{-1}\right)^{-1} \left(\mathbf{G}^T \mathbf{C}_\mathrm{D}^{-1} \mathbf{d} + \mathbf{C}_\mathrm{M}^{-1} \mathbf{m}_\mathrm{prior}\right) \quad . \tag{2.17}$$

As shown in Figure 2.3, the above found $\mathbf{m}$ model can be interpreted as the mean of the posterior PDF of the model parameters $\sigma(\mathbf{m})$, whose posterior covariance $\tilde{\mathbf{C}}_\mathrm{M}$ can be demonstrated to be (see Tarantola, 2005)

$$\tilde{\mathbf{C}}_\mathrm{M} = \left(\mathbf{G}^T \mathbf{C}_\mathrm{D}^{-1} \mathbf{G} + \mathbf{C}_\mathrm{M}^{-1}\right)^{-1} \quad . \tag{2.18}$$

Comparing equation (2.17) with equation (2.12), it becomes clear that the mean model from the probabilistic approach and the optimal model from the deterministic one match perfectly (barring the covariance matrix $\mathbf{C}_\mathrm{M}$, that is related to the injection of prior information).

Since a Gaussian PDF is completely characterized by mean and covariance, then $\sigma(\mathbf{m})$ is fully characterized by $\mathbf{m}$ and $\tilde{\mathbf{C}}_\mathrm{M}$ (Tarantola, 2005). This statement makes now clear as, from a probabilistic viewpoint, the solution to the inverse problem is not just the mean/optimal model, but the posterior PDF of the model parameters $\sigma(\mathbf{m})$.

To conclude, the linear probabilistic inverse problem just presented has been exploited to develop the inversion method presented in section 5.4.2.

2.4.2.2 Non-linear case

When the mathematical theory linking data to model parameters is non-linear, the Gaussian misfit function $R(\mathbf{m})$ assumes the following form

$$R(\mathbf{m}) = \left[(\mathbf{d} - \mathbf{g}(\mathbf{m}))^T \, \mathbf{C}_\mathrm{D}^{-1} \, (\mathbf{d} - \mathbf{g}(\mathbf{m}))\right] \quad , \tag{2.19}$$

thus, at a first glance, linear algebra cannot come to help us to finding the solution to the inverse problem. In addition, the function $R(\mathbf{m})$ might show more local minima, owing to the non-linearity of $\mathbf{g}(\mathbf{m})$.

In the next paragraphs, we show how these complications can be overcome following again a deterministic and probabilistic pathway.

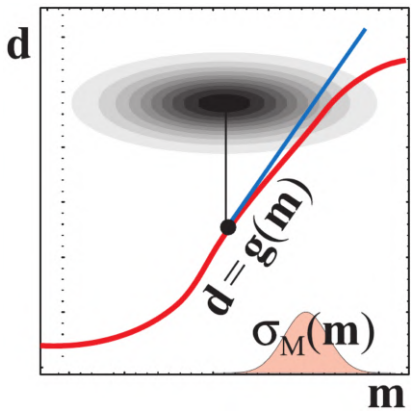

Figure 2.4 - Sketch representing an inverse problem characterized by forward problem $\mathbf{d} = \mathbf{g}(\mathbf{m})$ non-linear and posterior PDF of the model parameters $\sigma(\mathbf{m})$ approximately Gaussian. After Tarantola (2005).

Deterministic approach As shown in Figure 2.4, when the misfit function $R(\mathbf{m})$ is not far from being Gaussian, the way to take again advantage of linear algebra is to linearize the function $\mathbf{g}(\mathbf{m})$ around some model $\mathbf{m}_n$ through its Taylor series (truncated at the second-order term), i.e.,

$$\mathbf{g}(\mathbf{m}) \simeq \mathbf{g}(\mathbf{m}_n) + \dot{\mathbf{G}}(\mathbf{m}-\mathbf{m}_n) + \frac{1}{2}(\mathbf{m}-\mathbf{m}_n)^T \ddot{\mathbf{G}}(\mathbf{m}-\mathbf{m}_n) \quad , \tag{2.20}$$

where

$$\dot{G}_{n\alpha}^{\ i} = \left(\frac{\partial g^i}{\partial m^\alpha}\right)_{\mathbf{m}_n} \quad , \tag{2.21}$$

$$\ddot{G}_{n\alpha\beta}^{\ i} = \left(\frac{\partial \dot{G}^i}{\partial m^\beta}\right)_{\mathbf{m}_n} = \left(\frac{\partial^2 g^i}{\partial m^\alpha \partial m^\beta}\right)_{\mathbf{m}_n} \quad , \tag{2.22}$$

are the first and second derivatives of the function $\mathbf{g}(\mathbf{m})$ with respect to the model parameters on the point $\mathbf{m}_n$, respectively (see Tarantola, 2005). Nevertheless, such a linearization

requires that the function $\mathbf{g}(\mathbf{m})$ is at least C^2 class, and the derivatives can be computed either analytically or numerically (e.g., by finite-difference approximation). As far as (2.22), its calculation can be difficult to obtain, thus as we see below it is commonly approximate. If the above conditions are satisfied, then also the derivatives of the function $R(\mathbf{m})$ or $S(\mathbf{m})$ presented in sub-section 2.4.2.1 can be readily obtained. Here we continue the derivation considering $S(\mathbf{m})$, since injecting some prior information can help to find the global minimum in non-linear problem, known to show more that one local minima (Menke, 2018). Then, as shown by Tarantola (2005), the function $S(\mathbf{m})$ reduces to

$$\begin{aligned} 2S(\mathbf{m}) = (\mathbf{g}(\mathbf{m}) - \mathbf{d})^T \mathbf{C}_\mathrm{D}^{-1} (\mathbf{g}(\mathbf{m}) - \mathbf{d}) + \\ + (\mathbf{m} - \mathbf{m}_\mathrm{prior})^T \mathbf{C}_\mathrm{M}^{-1} (\mathbf{m} - \mathbf{m}_\mathrm{prior}) \quad , \end{aligned} \tag{2.23}$$

whereas its first derivative

$$\left(\frac{\partial S}{\partial \mathbf{m}} \right)_n = \dot{\mathbf{G}}_n^T \mathbf{C}_\mathrm{D}^{-1} (\mathbf{g}(\mathbf{m}_n) - \mathbf{d}) + \mathbf{C}_\mathrm{M}^{-1} (\mathbf{m}_n - \mathbf{m}_\mathrm{prior}) \quad , \tag{2.24}$$

and its second derivative

$$\left(\frac{\partial^2 S}{\partial \mathbf{m}^2} \right)_n = \dot{\mathbf{G}}_n^T \mathbf{C}_\mathrm{D}^{-1} \dot{\mathbf{G}}_n + \mathbf{C}_\mathrm{M}^{-1} + \ddot{\mathbf{G}}_n^T \mathbf{C}_\mathrm{D}^{-1} (\mathbf{g}(\mathbf{m}_n) - \mathbf{d}) \quad . \tag{2.25}$$

As already mentioned, the term $\ddot{\mathbf{G}}_n$ in expression (2.25) can be difficult to calculate, thus it is commonly neglected obtaining a simplified (and approximate) expression for (2.25)

$$\left(\frac{\partial^2 S}{\partial \mathbf{m}^2} \right)_n \simeq \left(\frac{\partial^2 S}{\partial \mathbf{m}^2} \right)_n^{\text{approx}} = \dot{\mathbf{G}}_n^T \mathbf{C}_\mathrm{D}^{-1} \dot{\mathbf{G}}_n + \mathbf{C}_\mathrm{M}^{-1} \quad . \tag{2.26}$$

Equations (2.24) - (2.25) represent the gradient and Hessian of the function $S(\mathbf{m})$, respectively; from a mathematical viewpoint, the gradient of a function at a certain point $\mathbf{m}_n$ indicates the direction of its maximum slope at that point, whereas the Hessian gives the same information but about the gradient. Hence, they can be employed to construct algorithms capable of finding the minimum of the function $S(\mathbf{m})$, progressively approaching it through a series of iterations. The model $\mathbf{m}_n$ achieved at iteration n will serve then for the $n+1$ iteration, and so on until the minimum is reached. The most common algorithms exploiting this philosophy are the following (Tarantola, 2005):

- Steepest descent algorithm:

$$\begin{aligned} \mathbf{m}_{n+1} &= \mathbf{m}_n - \mu_n \mathbf{C}_\mathrm{M} \left(\frac{\partial S}{\partial \mathbf{m}} \right)_n = \\ &= \mathbf{m}_n - \mu_n \left(\mathbf{C}_\mathrm{M} \dot{\mathbf{G}}_n^T \mathbf{C}_\mathrm{D}^{-1} (\mathbf{d}_n - \mathbf{d}_\mathrm{obs}) + (\mathbf{m}_n - \mathbf{m}_\mathrm{prior}) \right) \quad ; \end{aligned} \tag{2.27}$$

- Newton algorithm:

$$\begin{aligned} \mathbf{m}_{n+1} &= \mathbf{m}_n - \mu_n \left(\frac{\partial^2 S}{\partial \mathbf{m}^2} \right)_n \left(\frac{\partial S}{\partial \mathbf{m}} \right)_n = \\ &= \mathbf{m}_n - \mu_n \left(\dot{\mathbf{G}}_n^T \mathbf{C}_\mathrm{D}^{-1} \dot{\mathbf{G}}_n + \mathbf{C}_\mathrm{M}^{-1} + \ddot{\mathbf{G}}_n^T \mathbf{C}_\mathrm{D}^{-1} (\mathbf{d}_n - \mathbf{d}_\mathrm{obs}) \right)^{-1} \cdot \\ &\cdot \quad \left(\dot{\mathbf{G}}_n^T \mathbf{C}_\mathrm{D}^{-1} (\mathbf{d}_n - \mathbf{d}_\mathrm{obs}) + \mathbf{C}_\mathrm{M}^{-1} (\mathbf{m}_n - \mathbf{m}_\mathrm{prior}) \right) \quad ; \end{aligned} \tag{2.28}$$

- Quasi-Newton algorithm:

$$\begin{aligned}\mathbf{m}_{n+1} &= \mathbf{m}_n - \mu_n \left(\frac{\partial^2 S}{\partial \mathbf{m}^2}\right)_n \left(\frac{\partial S}{\partial \mathbf{m}}\right)_n^{\text{approx}} = \\ &= \mathbf{m}_n - \mu_n \left(\dot{\mathbf{G}}_n^T \mathbf{C}_\text{D}^{-1} \dot{\mathbf{G}}_n + \mathbf{C}_\text{M}^{-1}\right)^{-1} \cdot \\ &\cdot \quad \left(\dot{\mathbf{G}}_n^T \mathbf{C}_\text{D}^{-1} (\mathbf{d}_n - \mathbf{d}_\text{obs}) + \mathbf{C}_\text{M}^{-1} (\mathbf{m}_n - \mathbf{m}_\text{prior})\right) \quad , \end{aligned} \tag{2.29}$$

where $\mathbf{d}_n = \mathbf{g}(\mathbf{m}_n)$ represents the calculated data at each iteration. The coefficient μ_n is an *ad hoc* parameter that allows to size the "jump" performed at each iteration; its value should be chosen as a compromise between keeping small the number of iterations and approaching gradually the minimum of the function $S(\mathbf{m})$ to avoid divergence. Values are generally below 1 for the steepest descent algorithm and close to 1 for the Newton and Quasi-Newton ones. It is interesting to notice that the Hessian or its approximation in the Newton and Quasi-Newton algorithms act as the inverse of the covariance matrix $\mathbf{C}_\text{M}$ in the steepest descent algorithm, but differently from this one reflects the local metric of the misfit function $S(\mathbf{m})$.

To the category of the Quasi-Newton algorithms belongs the so-called Broyden-Fletcher-Goldfarb-Shanno (BFGS) algorithm (Fletcher, 1987) and its variants, such as the Limited-memory BFGS (L-BFGS; Nocedal and Wright, 2006), used in chapter 4 to highlight the strengths of the HMC inversion method presented in the same chapter.

Probabilistic approach We have seen in paragraph "Linear case - Probabilistic approach" that a linear inverse problem can be treated in terms of PDFs and, in case they are Gaussian, the solution $\sigma(\mathbf{m})$ is a posterior PDF fully characterized by a mean model $\mathbf{m}$, representing the optimal model obtained using the deterministic approach, and a posterior covariance matrix $\mathbf{C}_\text{M}$, providing a measure of its uncertainty. In these conditions, the deterministic and probabilistic viewpoints of the inverse problems substantially coincide.

However, as already explained, the non-linearity of the forward problem $\mathbf{g}(\mathbf{m})$ may lead to the misfit function $R(\mathbf{m})$ no longer being Gaussian, that is showing several local minima

and then multi-modal PDF. As a result, even the posterior $\sigma(\mathbf{m})$ is no longer Gaussian, making the concept of "mean solution" to the inverse problem critical (Figure 2.5).

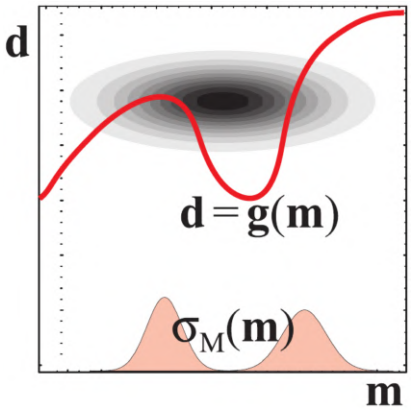

Figure 2.5 - Sketch representing an inverse problem characterized by forward problem $\mathbf{d} = \mathbf{g}(\mathbf{m})$ non-linear and posterior PDF of the model parameters $\sigma(\mathbf{m})$ non-Gaussian, requiring a Markov Chain Monte Carlo algorithm to be characterized. After Tarantola (2005).

In addition, when the amount of model parameters is large (i.e., multi-dimensional model space, that is the case of the majority of inverse problems), the posterior $\sigma(\mathbf{m})$ of the model parameters is impossible to be graphically represented. High-dimensional model spaces are also affected by a significant emptiness (Tarantola, 2005), that is the peaks of $\sigma(\mathbf{m})$ may be far from each others.

Then, a different strategy is necessary to explore and characterize $\sigma(\mathbf{m})$ compared to what we have seen so far. This strategy is referred to as *sampling* and is performed by methods called *Markov Chain Monte Carlo* (MCMC, Tarantola, 2005). As depicted in Figure 2.6, these methodologies sample the posterior PDF of the model parameters $\sigma(\mathbf{m})$ generating independent points (or samples) of it, each of them representing a different model solution $\mathbf{m}$. Then, the final result will be a "collection of models" $\{\mathbf{m}_n \,|\, n \in \mathbb{N}\}$ representative of the posterior $\sigma(\mathbf{m})$. Basically, what performs the sampling is the so-called sampler, an algorithm that obeys certain probabilistic rules. Many flavours of samplers exist, each of them defining a different MCMC method designed to be more suitable for the inverse problem we are interested to solve. Examples of samplers are the Gibb's, rejection, sequential realization,

Metropolis and Metropolis-Hastings algorithms (see Tarantola, 2005, for a general overview on this argument).

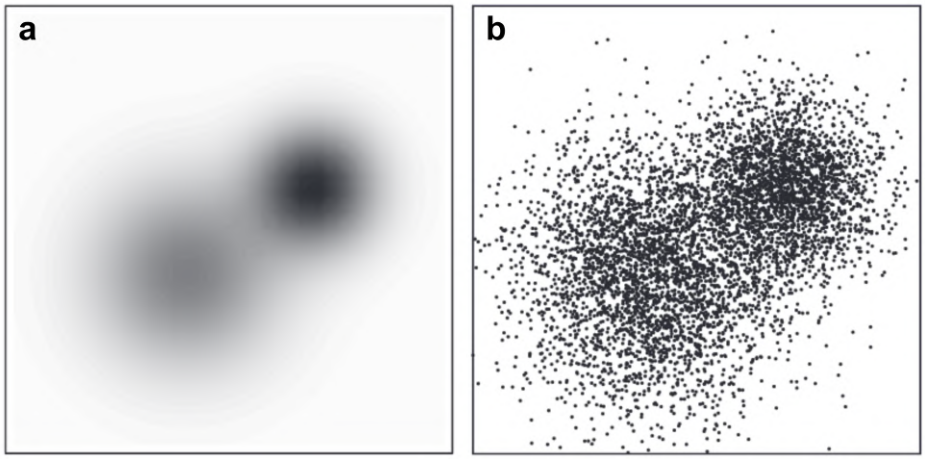

Figure 2.6 - (a) Two-dimensional PDF. (b) Characterization of a two-dimensional PDF by its sampling. Modified from Tarantola (2005).

The Metropolis algorithm (Metropolis et al., 1953) is used by the Hamiltonian Monte Carlo strategy (HMC), a particularly efficient MCMC approach which integrates, during the sampling, the information derived from the calculation of the gradient of the posterior $\sigma(\mathbf{m})$, capable of steering the inversion process toward high-probability area in the model space (Duane et al., 1987; Fichtner et al., 2019; Neal, 2012). In HMC, the Metropolis sampler is used to accept or reject a "jump" in the model space from a point $\mathbf{m}_n$ to the new point $\mathbf{m}_{n+1}$, according to the value assumed by the likelihood function $L(\mathbf{m})$, as follows

- if $L(\mathbf{m}_{n+1}) \geq L(\mathbf{m}_n) \implies$ the proposed move is accepted;
- if $L(\mathbf{m}_{n+1}) < L(\mathbf{m}_n) \implies$ the proposed move is randomly either rejected or accepted, in the latter case with a probability calculated as $P_{n \to n+1} = \dfrac{L(\mathbf{m}_{n+1})}{L(\mathbf{m}_n)}$.

The HMC strategy just presented has been exploited to develop the methodology to invert gravity and magnetic data in case of 2D/2.75D polygonal bodies discussed in chapter 4, which has proven to be an excellent tool to manage both the non-linearity and the non-uniqueness

issues affecting this inverse problem. Moreover, more details about the theoretical framework of HMC are provided in section 4.3.1.

Part II

2D to 2.75D polygon-based parameterization approaches

Chapter 3

Magnetic Anomalies Caused by 2D Polygonal Structures With Uniform Arbitrary Polarization

Abstract

Since the '60s of the last century, the calculation of the magnetic anomalies caused by 2D uniformly polarized bodies with polygonal cross-section has been mainly performed using the popular algorithm of Talwani and Heirtzler (1962, 1964). Recently, Kravchinsky et al. (2019) claimed errors in the above algorithm formulation, proposing new corrective formulas and questioning the effectiveness of almost 60 years of magnetic calculations. Here we show that the two approaches are equivalent and Kravchinsky et al.'s formulas simply represent an algebraic variant of those of Talwani and Heirtzler. Moreover, we analyze a large amount of random magnetic scenarios, involving both changing-shape polygons and a realistic geological model, showing a complete agreement among the magnetic responses of the two discussed algorithms and the one proposed by Won and Bevis (1987).

3.1 Introduction

Modeling of magnetic anomalies is a fundamental tool in exploration geophysics. Since the appearance of early electronic computers, calculation of the magnetic field from models of the subsurface and the related inverse problem have played a major role in the geological interpretation of magnetic anomalies.

An early mathematical formulation for anomalies due to 2D polygonal structures of uniform polarization is found in Talwani and Heirtzler (1962, 1964). Their algorithm remains the most used and cited to date. Thanks to its wide applicability, Talwani and Heirtzler's approach has become popular, both for expeditious interpretation of magnetic data and as a forward engine for inverse methods. Moreover, the aforementioned 2D formulation can be extended to 3D bodies (Plouff, 1975, 1976; Talwani, 1965). More recently, Won and Bevis (1987) proposed an evolution of the original formulation by Talwani and Heirtzler which avoids the use of trigonometric functions, achieving a speed up of the calculation of magnetic anomaly.

Another popular approach, which considers 2D or 3D prism-shaped bodies instead of polygonal-shaped ones, is that proposed in Bhattacharyya (1964). Such approach leads to a formulation where the subsurface is modeled as a set of prismatic bodies, often a set of rectangular cells, characterized by constant magnetic properties.

Despite the fact that in recent years forward calculations have moved toward the computation of magnetic anomalies caused by 3D bodies, hand in hand with the rapid increase in CPU speed, 2D modeling still represents a widely utilized tool to quickly and intuitively gain a better understanding of the subsurface and is particularly effective for bodies striking perpendicularly to the profile. Moreover, the much lower computational requirements for 2D calculations make them viable for simple interpretations of the magnetic signatures (e.g., in a trial and error approach) and to performing analysis directly on the field (e.g., on a laptop).

Since the introduction of the abovementioned algorithms, the 2D approach has evolved to overcome the simplistic assumption of a uniform polarization in magnetized bodies, trying to consider both demagnetization effects and non-uniform magnetization (Bhattacharyya and Chan, 1977; Bhattacharyya and Navolio, 1975, 1976; Blokh, 1980; Kostrov, 2007; Ku, 1977; Mariano and Hinze, 1993). Unfortunately, the mathematical models considered often represent a simplified approximation of the complexities of experimentally observed spatial variation of rock magnetization. For a more detailed presentation of the main developments in forward magnetic calculation methods, readers are referred to Kostrov (2007) and Nabighian et al. (2005).

Very recently, Kravchinsky et al. (2019) suggested the evidence of omissions and errors in the formulation of Talwani and Heirtzler (1962, 1964) that would lead to mistakes in the calculation of magnetic anomalies, proposing a modified algorithm to avoid that.

In this chapter, we compare the original formulations of Talwani and Heirtzler (1962, 1964), Won and Bevis (1987), and the newer Kravchinsky et al. (2019) both from analytical and numerical points of view. For the former, the algorithms have been analyzed in order to highlight algebraic differences and similarities, while for the latter they have been tested and compared by using a variety of randomly generated scenarios involving both induced and remanent magnetization on shape-changing polygons, to detect possible numerical differences or failing scenarios. In detail, we start by illustrating the three formulations of the algorithms in section 3.2 and then we discuss in deep the similarities and differences in section 3.3. We finally show that, after fixing some issues in Kravchinsky et al. (2019), their formulation and that of Talwani and Heirtzler (1962, 1964) are essentially the same algorithm, and that all three algorithms, that is, including Won and Bevis (1987), produce the same results.

In addition, the rectified Kravchinsky et al.'s algorithm together with the other ones discussed in this work are released in a set a set of open-source packages written in Python and Julia languages (see Appendix 3.D for more details).

3.2 Algorithm Formulations

Let us consider a three-dimensional non-magnetic space in which a body infinitely extends in y direction. The common aim of all formulations is the calculation of the magnetic field of this body at observation points located along a profile aligned to the x direction at a certain height (the positive z axis is assumed pointing downward). The starting assumption is that our body can be considered as discretized by an infinite number of uniformly magnetized elementary volumes with infinitesimal dimensions dx, dy, and dz. Within this assumption, the magnetic field generated by the body can be mathematically expressed in terms of a line integral around its periphery, represented in two dimensions as its polygonal cross-section (Figure 3.1a). The specific procedures for each formulation are summarized in the subsections below. For the respective detailed derivations, the reader is referred to Kravchinsky et al. (2019), Talwani and Heirtzler (1962, 1964), and Won and Bevis (1987).

3.2.1 Talwani and Heirtzler

The formulation of Talwani and Heirtzler (1962, 1964) starts from the definition of the magnetic potential Ω

$$d\Omega = \frac{\mathbf{M}\cdot\mathbf{R}}{R^3}\,dxdydz \quad , \tag{3.1}$$

relative to an elementary volume with uniform magnetization $\mathbf{M}$ and distance $\mathbf{R}$ from the observation point with coordinates (x_0, z_0). By integrating expression (3.1) from negative

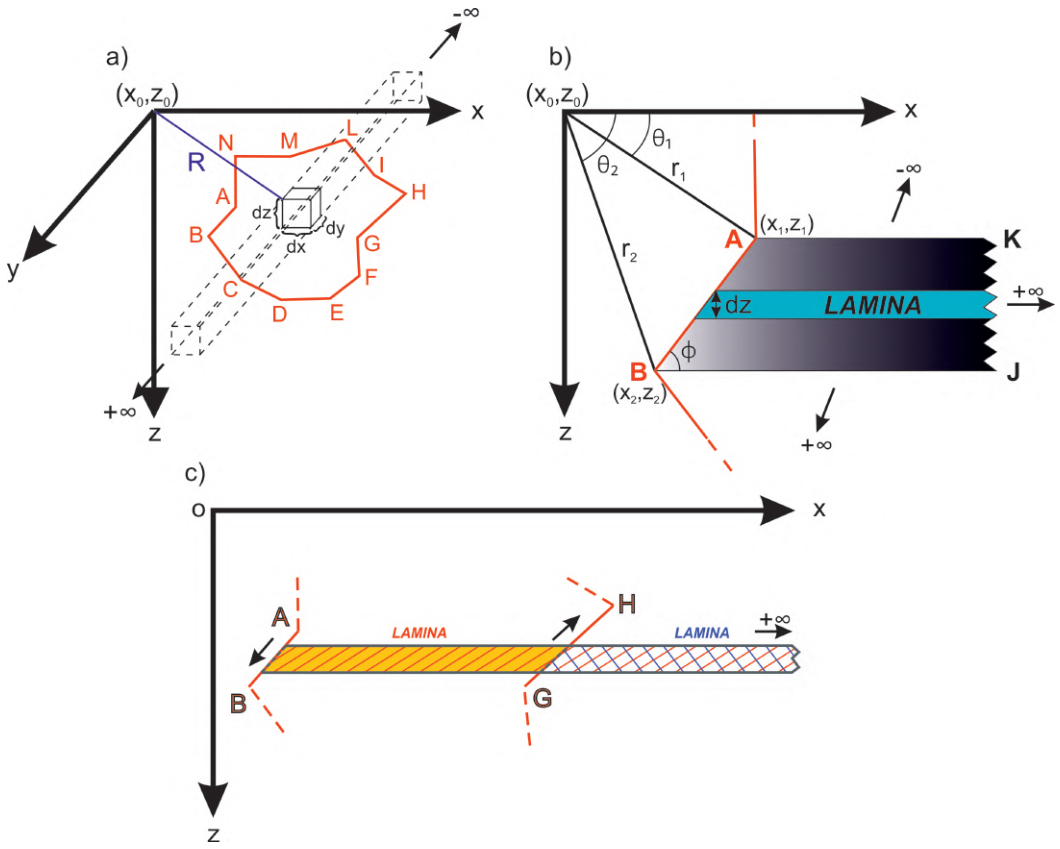

Figure 3.1 - (a) Elementary volume with uniform magnetization immersed in a non-magnetic space. This volume can be extended in the space to define an infinitely elongated body in the y direction. The polygon in red represents the cross-section of this body, that we consider for computing the magnetic field relative to the entire body. Modified from Kravchinsky et al. (2019). (b) Sketch of all the parameters involved in the calculation of the vertical B_z and horizontal B_x magnetic strength in Talwani and Heirtzler's algorithm. The semi-infinite lamina of thickness dz expands to form a semi-infinite prism with section $ABJK$ built on the side AB of the body. Modified from Kravchinsky et al. (2019). (c) Representation of the laminas with thickness dz built along the polygon sides AB and GH drawn in Figure (a). Moving in a counterclockwise order (black arrows), the lamina along the side AB, defining a semi-infinite infinitesimal prism elongated in the positive x direction (red), provides a positive field, whereas the lamina on the side CD provides a negative field, smaller in absolute value owing to the less extended semi-infinite infinitesimal prism defined along this side (blue). The resulting magnetic anomaly, obtained as scalar sum between the total fields caused by the two laminas, is relative to the area in yellow inside the polygon.

to positive infinity in the y direction, we achieve the magnetic potential due to an infinitely elongated prism (Figure 3.1a). The vertical B_z and horizontal B_x components of the magnetic strength of this prism can be obtained differentiating its magnetic potential with respect to x and z directions (the derivative of the magnetic potential along y is null not appearing this variable in the expression of the potential (see Talwani and Heirtzler, 1962). Now, integrating B_z and B_x from x to positive infinity, we obtain new expressions for B_z and B_x

$$B_z = 2\,\frac{M_x z - M_z x}{(x^2+z^2)}\,dz \quad , \tag{3.2}$$

$$B_x = 2\,\frac{M_x x - M_z z}{(x^2+z^2)}\,dz \quad , \tag{3.3}$$

that are relative to a semi-infinite lamina with thickness d_z (Figure 3.1b). M_x and M_z represent the components of the magnetization vector $\mathbf{M}$ along the x and z axes. Whether $\mathbf{M}$ is characterized by induced magnetization only, its own inclination and declination correspond to those of the Earth magnetic field, while in the case of coexistence of induced and remanent magnetization the resultant $\mathbf{M}$ is the vectorial sum of both contributions (Figures 3.2a and 3.2b).

Now, let us imagine for instance to extend this lamina along the polygon side AB shown in Figure 3.1b: integrating (3.2–3.3) from z_1 to z_2, representing the z coordinates of the side vertices taken in a counterclockwise order, we obtain a revised expression for B_z and B_x

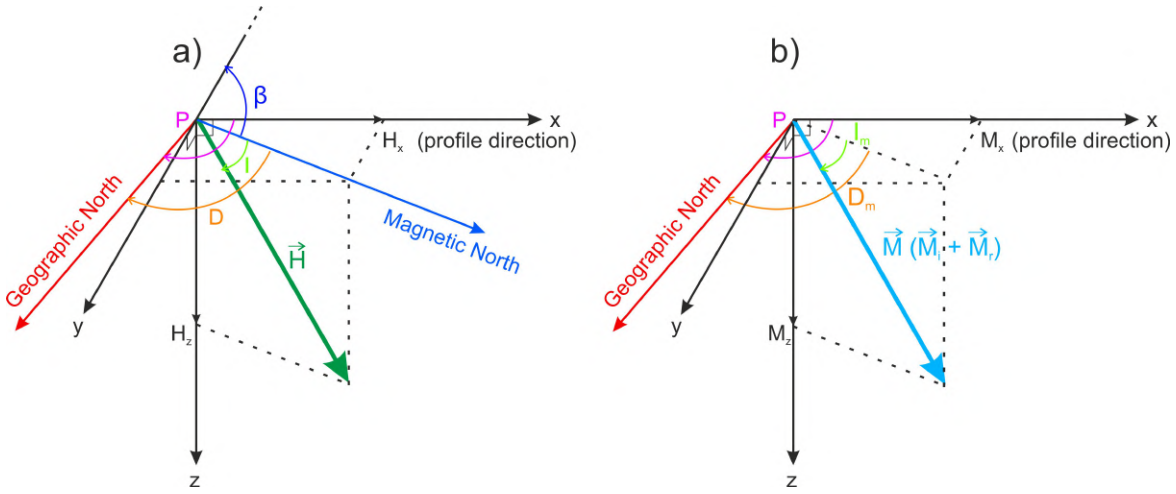

Figure 3.2 - (a) Total Earth magnetic field **H**, characterized by changing inclination I and declination D as a function of profile location upon Earth surface. I is defined as the angle made by **H** with the horizontal plane and D as the angle between the Magnetic and the Geographic Norths. In detail, I may vary from $\pm 90^\circ$ (respectively at North and South Poles) to 0° (at the equator) and D from 180° to -180°. The angle P define the orientation of the profile direction (x axis) along with the computation of the magnetic field is performed. β is the angle between the magnetic north and the negative direction of the body elongation ($-y$). I, D, and P are taken clockwise, whereas β counterclockwise. (b) Total magnetization vector **M**, defined as the vectorial sum of induced $\mathbf{M}_\mathrm{i}$ and remanent $\mathbf{M}_\mathrm{r}$ magnetization. It is characterized by own inclination I_m and declination D_m. In the case of induced magnetization solely, then $I_\mathrm{m} = I$ and $D_\mathrm{m} = D$.

$$
\begin{aligned}
B_z &= 2\,\sin(\phi)\Big\{M_x\left[(\theta_2-\theta_1)\cos(\phi)+\sin(\phi)\ln\left(\frac{r_2}{r_1}\right)\right]+ \\
&\quad -M_z\left[(\theta_2-\theta_1)\sin(\phi)-\cos(\phi)\ln\left(\frac{r_2}{r_1}\right)\right]\Big\} \quad , \qquad (3.4)\\
B_x &= 2\,\sin(\phi)\Big\{M_x\left[(\theta_2-\theta_1)\sin(\phi)-\cos(\phi)\ln\left(\frac{r_2}{r_1}\right)\right]+ \\
&\quad +M_z\left[(\theta_2-\theta_1)\cos(\phi)+\sin(\phi)\ln\left(\frac{r_2}{r_1}\right)\right]\Big\} \quad , \qquad (3.5)
\end{aligned}
$$

where

$$
r_1=\sqrt{x_1^2+z_1^2}\;;\; r_2=\sqrt{x_2^2+z_2^2} \quad , \qquad (3.6)
$$

and the following angles

$$
\theta_1=\arctan\left(\frac{z_1}{x_1}\right)\;;\;\theta_2=\arctan\left(\frac{z_2}{x_2}\right) \quad , \qquad (3.7)
$$

$$
\phi=\arctan\left(\frac{z_2-z_1}{x_1-x_2}\right) \quad . \qquad (3.8)
$$

Notice that x_1, x_2, z_1, and z_2 are respectively the x and z coordinates of the side vertices with respect to an observation point (x_0, z_0) where the magnetic anomaly is calculated (Figure 3.1b). Besides, the side vertices are taken in a counterclockwise order.

Equations (3.4) and (3.5) represent the vertical and horizontal components of the magnetic strength due to a semi-infinite prism with section $ABKJ$ (K and J located at infinity) built on the side AB (Figure 3.1b). These equations can be rewritten in a simplified fashion as

$$B_z = 2\left(M_x Q - M_z P\right) \quad , \tag{3.9}$$

$$B_x = 2\left(M_x P + M_z Q\right) \quad , \tag{3.10}$$

in which the terms P and Q are

$$P = \frac{z_{21}x_{21}}{z_{21}^2 + x_{21}^2}\ln\frac{r_2}{r_1} + \frac{z_{21}^2}{z_{21}^2 + x_{21}^2}\left(\theta_2 - \theta_1\right) \quad , \tag{3.11}$$

$$Q = \frac{z_{21}^2}{z_{21}^2 + x_{21}^2}\ln\frac{r_2}{r_1} - \frac{z_{21}x_{21}}{z_{21}^2 + x_{21}^2}\left(\theta_2 - \theta_1\right) \quad , \tag{3.12}$$

where

$$x_{21} = x_2 - x_1 \; ; \; z_{21} = z_2 - z_1 \quad . \tag{3.13}$$

In the case $z_{21} = 0$, both P and Q become zero and therefore the side provides no magnetic contribution.

Now, the total field scalar anomaly is obtained as vectorial projection of B_z and B_x along the direction of the Earth magnetic field as follows

$$T = B_z \sin(I) + B_x \cos(I)\sin(P - D) \quad , \tag{3.14}$$

where I and D are respectively the inclination and declination of the Earth magnetic field, whereas P is the angle between the Geographic North and the profile direction along with the magnetic field of the body is computed (Figure 3.2a).

Finally, since the polygon consists of n sides, the overall total field scalar anomaly is computed by summing over the contributions T relative to each side in a counterclockwise order. A simplified representation of the physical meaning of the latter operation is illustrated in Figure 3.1c.

3.2.2 Kravchinsky et al.

Kravchinsky et al. (2019) suggested the existence of some mathematical omissions and errors in the original formulation of Talwani and Heirtzler (1962, 1964), with consequently possible failure of magnetic anomaly calculations. Nevertheless, this new formulation derives closely from that of Talwani and Heirtzler (1962, 1964), starting from the definition of the magnetic potential in the case of SI units (modified by a factor $\frac{1}{4}\pi$ with respect to 3.1). The mathematical derivation partially differs during the integration from z_1 to z_2 leading to the Talwani and Heirtzler's corresponding (3.2) and (3.3), owing to a different definition of x, leading to the following new modified terms P and Q (Kravchinsky et al., 2019)

$$P = \frac{z_{21}x_{21}}{z_{21}^2+x_{21}^2}\ln\frac{r_2}{r_1}+\delta\frac{z_{21}^2}{z_{21}^2+x_{21}^2}\Big(\alpha_2-\alpha_1\Big) \quad , \tag{3.15}$$

$$Q = \frac{z_{21}^2}{z_{21}^2+x_{21}^2}\ln\frac{r_2}{r_1}-\delta\frac{z_{21}x_{21}}{z_{21}^2+x_{21}^2}\Big(\alpha_2-\alpha_1\Big) \quad , \tag{3.16}$$

where the meanings of r_1, r_2, x_{21}, and z_{21} are defined in (3.6–3.13).

Now recalling (3.13), then

$$g=\frac{x_{21}}{z_{21}} \quad , \tag{3.17}$$

and

$$\begin{cases} -1 & \text{if } x_1 < gz_1 \\ 1 & \text{if } x_1 > gz_1 \quad , \end{cases} \tag{3.18}$$

$$\alpha_1 = \arctan\left(\frac{\delta\,(z_1 + gx_1)}{x_1 - gz_1}\right) \quad , \tag{3.19}$$

$$\alpha_2 = \arctan\left(\frac{\delta\,(z_2 + gx_2)}{x_2 - gz_2}\right) \quad . \tag{3.20}$$

The new relations (3.15-3.16) appear very similar to the previous equations (3.11) and (3.12) and the major difference seems to be related to the different expression of the angles α_1 and α_2 in place of Talwani's θ_1 and θ_2 (cfr. equations 3.7-3.19-3.20). In addition, the formulas of the angles α_1 and α_2 present also a δ term in order to remove the absolute value at $x_1 - gz_1$ and $x_2 - gz_2$, respectively (cfr. Kravchinsky et al., 2019, supporting information).

Now, the computation of the vertical and horizontal components of the magnetic strength B_z and B_x is achieved by means of the following equations

$$B_z = \frac{1}{2\pi}\,(M_x Q - M_z P) \quad , \tag{3.21}$$

$$B_x = \frac{1}{2\pi}\,(M_x P + M_z Q) \quad , \tag{3.22}$$

which differs from Talwani and Heirtzler's ones only of a factor $\frac{1}{4}\pi$ owing to the utilization of SI instead of emu units.

At this point, the computation of the scalar total field magnetic anomaly of the entire body should be carried out using equation (3.14) for each polygon side in a counterclockwise order as for Talwani and Heirtzler's algorithm. On the contrary, the authors (Kravchinsky et al., 2019) specify a clockwise order that, from a physical point of view, corresponds to having a semi-infinite polygon in the opposite x direction built for each side, resulting in a

negative scalar total field ($-T$) contribution. In Appendix 3.A.1 we explain how such issue has been corrected.

3.2.3 Won and Bevis

Won and Bevis (1987) proposed a faster approach to compute the magnetic anomaly thanks to the substitution of trigonometric functions with simpler relations referred to the vertex coordinates of the polygon (e.g., Grant and West, 1965). Moreover, this formulation allows to perform magnetic calculation even in the case of side vertices crossing the x axis.

However, the theory behind this algorithm differs from that previously examined, being the formulation derived by means of the Poisson relation (Won and Bevis, 1987). This relation links the gravitational attraction to the scalar magnetic potential of a body, taking advantage from the similarities between them. For instance, both have magnitude that is inversely proportional to the square of the distance to the relative sources (Blakely, 1996). The Poisson relation can be differentiated to obtain the magnetic strength vector $\mathbf{B}$ as follows

$$\mathbf{B} = \frac{|\mathbf{M}|}{G\rho} \frac{\partial}{\partial \alpha} \left(\mathbf{g}^{'} \right) \quad , \tag{3.23}$$

where $|\mathbf{M}|$ is the magnetization module, G the gravitational constant, ρ the body density, and $\mathbf{g}^{'}$ the gravitational attraction related to the body. The term $\frac{\partial}{\partial \alpha}$ is defined as follows

$$\frac{\partial}{\partial \alpha} \equiv \sin(I_m) \frac{\partial}{\partial z} + \sin(\beta) \cos(I_m) \frac{\partial}{\partial x} \quad , \tag{3.24}$$

where I_m represents the inclination of the magnetization vector and β the strike of the body measured counterclockwise from magnetic north to the negative y axis (Figure 3.2a). This relation is used to achieve the magnetic strength components of a polygon side along z and x, that are

$$B_z = \frac{|\mathbf{M}|}{G\rho}\left(\sin(I_m)\frac{\partial g_z^{'}}{\partial z}+\cos(I_m)\sin(\beta)\frac{\partial g_z^{'}}{\partial x}\right) \quad , \tag{3.25}$$

$$B_x = \frac{|\mathbf{M}|}{G\rho}\left(\sin(I_m)\frac{\partial g_x^{'}}{\partial z}+\cos(I_m)\sin(\beta)\frac{\partial g_x^{'}}{\partial x}\right) \quad , \tag{3.26}$$

where $g_x^{'}$ and $g_z^{'}$ are the x and z components of the gravitational attraction of the body, defined as

$$g_x^{'} = 2G\rho X \; ; \; g_z^{'} = 2G\rho Z \quad , \tag{3.27}$$

with X and Z representing line integrals along the polygon side (refer to Won and Bevis 1987 for details).

Recalling (3.6-3.7-3.13-3.17), the partial derivatives of X and Z with respect to x and z are respectively

$$\frac{\partial X}{\partial x} = \frac{x_{21}z_{21}}{x_{21}^2+z_{21}^2}\left[\frac{1}{g}\Big(\theta_1-\theta_2\Big)-\ln\frac{r_2}{r_1}\right]+P \quad , \tag{3.28}$$

$$\frac{\partial X}{\partial z} = -\frac{x_{21}^2}{x_{21}^2+z_{21}^2}\left[\frac{1}{g}\Big(\theta_1-\theta_2\Big)-\ln\frac{r_2}{r_1}\right]+Q \quad , \tag{3.29}$$

$$\frac{\partial Z}{\partial x} = -\frac{x_{21}z_{21}}{x_{21}^2+z_{21}^2}\left[\Big(\theta_1-\theta_2\Big)+\frac{1}{g}\ln\frac{r_2}{r_1}\right]+Q \quad , \tag{3.30}$$

$$\frac{\partial Z}{\partial z} = -\frac{x_{21}^2}{x_{21}^2+z_{21}^2}\left[\Big(\theta_1-\theta_2\Big)+\frac{1}{g}\ln\frac{r_2}{r_1}\right]-P \quad , \tag{3.31}$$

where now

$$P = \frac{x_1 z_2 - x_2 z_1}{x_{21}^2 + z_{21}^2} \left[\frac{x_1 x_{21} - z_1 z_{21}}{r_1^2} - \frac{x_2 x_{21} - z_2 z_{21}}{r_2^2} \right] \quad , \tag{3.32}$$

$$Q = \frac{x_1 z_2 - x_2 z_1}{x_{21}^2 + z_{21}^2} \left[\frac{x_1 z_{21} - z_1 x_{21}}{r_1^2} - \frac{x_2 z_{21} - z_2 x_{21}}{r_2^2} \right] \quad . \tag{3.33}$$

As in the previous derivations, the total field scalar anomaly of the side is obtained as a projection of B_z and B_x onto the Earth magnetic field

$$T = B_z \sin(I) + B_x \cos(I) \sin(\beta) \quad . \tag{3.34}$$

Contrary to the two preceding algorithms, now the computation of the total field scalar magnetic anomaly of the body using (3.34) should be carried out in clockwise order.

3.3 Discussion

3.3.1 Analytical Results

The three formulations discussed in this study aim to the same objective of calculating the magnetic anomaly due to a body with uniform magnetization and polygonal section. Among these, those of Kravchinsky et al. (2019) and Talwani and Heirtzler (1962, 1964) present similar derivations, with some differences. In principle, Kravchinsky et al. (2019) addressed some mathematical errors and omissions in the original derivation of Talwani and Heirtzler, revealing some inconsistencies in magnetic anomaly calculation. However, after analyzing the two formulations, some inaccuracies in Kravchinsky et al. (2019) have been found. These issues are related to (a) the order of calculation around the polygon sides (clockwise/counterclockwise), (b) the use of the cosine theorem formula, and (c) the

projection of B_z and B_x along the Earth magnetic field vector. A detailed discussion of these findings is provided in Appendix 3.A.

Regarding to the corrections brought to Talwani and Heirtzler (1962, 1964) by Kravchinsky et al. (2019), they mainly concern: (a) a modification of the definitions of the angles θ_1 and θ_2 and (b) an addition of a δ term in order to account for an absolute value which appears in their derivation.

In the following, we illustrate how the two algorithms, after removing the inaccuracies in Kravchinsky et al. (2019), can be reconciled to a single approach, showing their equivalence from an analytic point of view. For this purpose, let us rewrite expressions (3.19-3.20) substituting the term δ with an absolute value at both the denominators in the argument of the arctangents, since $x_1 - gz_1 = x_2 - gz_2$ (refer to the supporting information of Kravchinsky et al. (2019) for an explanation)

$$\alpha_1 = \arctan\left(\frac{z_1 + gx_1}{|x_1 - gz_1|}\right) \quad , \tag{3.35}$$

$$\alpha_2 = \arctan\left(\frac{z_2 + gx_2}{|x_2 - gz_2|}\right) \quad , \tag{3.36}$$

where the term g is the same than the one presented in equation (3.17). Then, by canceling out x_1 and x_2 both in the numerator and denominator of the argument of the respectively arctangents α_1 and α_2, we can distinguish two cases:

1. If $x_1 - gz_1 = x_2 - gz_2 > 0$ (that is $\delta = 1$ in 3.19-3.20)

$$\alpha_1 = \arctan\left(\frac{z_1+gx_1}{x_1-gz_1}\right) = \arctan\left(\frac{\frac{z_1}{x_1}+g}{1-\frac{z_1}{x_1}g}\right) \quad , \tag{3.37}$$

$$\alpha_2 = \arctan\left(\frac{z_2+gx_2}{x_2-gz_2}\right) = \arctan\left(\frac{\frac{z_2}{x_2}+g}{1-\frac{z_2}{x_2}g}\right) \quad . \tag{3.38}$$

2. If $x_1 - gz_1 = x_2 - gz_2 < 0$ (that is $\delta = -1$ in 3.19-3.20)

$$\alpha_1 = \arctan\left(-\frac{z_1+gx_1}{x_1-gz_1}\right) = \arctan\left(-\frac{\frac{z_1}{x_1}+g}{1-\frac{z_1}{x_1}g}\right) \quad , \tag{3.39}$$

$$\alpha_2 = \arctan\left(-\frac{z_2+gx_2}{x_2-gz_2}\right) = \arctan\left(-\frac{\frac{z_2}{x_2}+g}{1-\frac{z_2}{x_2}g}\right) \quad . \tag{3.40}$$

Now, using the mathematical relation combining sums of arctangents in a unique arctangent expression

$$\arctan(A)+\arctan(B) = \begin{cases} \arctan\left(\dfrac{A+B}{1-AB}\right) & \text{if } AB<1 \\ \arctan\left(\dfrac{A+B}{1-AB}\right)+(\text{sign of } A)\pi & \text{if } AB>1 \end{cases} \quad , \tag{3.41}$$

then we can rewrite (3.37 $\rightarrow$ 3.40) as

$$\alpha_1 = \arctan\left(\frac{g+\frac{z_1}{x_1}}{1-g\frac{z_1}{x_1}}\right) = \arctan(g) + \arctan\left(\frac{z_1}{x_1}\right) \quad , \tag{3.42}$$

$$\alpha_2 = \arctan\left(\frac{g+\frac{z_2}{x_2}}{1-g\frac{z_2}{x_2}}\right) = \arctan(g) + \arctan\left(\frac{z_2}{x_2}\right) \quad , \tag{3.43}$$

when the product $\frac{z_1}{x_1}g = \frac{z_2}{x_2}g < 1$, and

$$\begin{aligned} \alpha_1 &= \arctan\left(-\frac{g+\frac{z_1}{x_1}}{1-g\frac{z_1}{x_1}}\right) = -\arctan\left(\frac{g+\frac{z_1}{x_1}}{1-g\frac{z_1}{x_1}}\right) \\ &= -\arctan(g) - \arctan\left(\frac{z_1}{x_1}\right) + (\text{sign of } g)\pi \quad , \end{aligned} \tag{3.44}$$

$$\begin{aligned} \alpha_2 &= \arctan\left(-\frac{g+\frac{z_2}{x_2}}{1-g\frac{z_2}{x_2}}\right) = -\arctan\left(\frac{g+\frac{z_2}{x_2}}{1-g\frac{z_2}{x_2}}\right) \\ &= -\arctan(g) - \arctan\left(\frac{z_2}{x_2}\right) + (\text{sign of } g)\pi \quad , \end{aligned} \tag{3.45}$$

when $\frac{z_1}{x_1}g = \frac{z_2}{x_2}g > 1$.

As it is apparent, the terms $\arctan\left(\frac{z_1}{x_1}\right)$ and $\arctan\left(\frac{z_2}{x_2}\right)$ are exactly equivalent to the expressions of θ_1 and θ_2 in Talwani and Heirtzler (1962, 1964) (see Figure 3.B.1 in Appendix 3.B for details concerning the angles involved in Kravchinsky et al. (2019) formulation). Hence, canceling out each term $\arctan(g)$, in the case (1) the difference $\alpha_2 - \alpha_1$ will always be algebraically the difference $\theta_2 - \theta_1$, whereas in (2) $\alpha_2 - \alpha_1$ will be equal to $-(\theta_2 - \theta_1)$. Recalling now the expressions (3.11–3.12) for P and Q in Talwani and Heirtzler (1962, 1964),

$$P = \frac{z_{21}x_{21}}{z_{21}^2+x_{21}^2}\ln\frac{r_2}{r_1}+\frac{z_{21}^2}{z_{21}^2+x_{21}^2}\Big(\theta_2-\theta_1\Big) \quad , \tag{3.46}$$

$$Q = \frac{z_{21}^2}{z_{21}^2+x_{21}^2}\ln\frac{r_2}{r_1}-\frac{z_{21}x_{21}}{z_{21}^2+x_{21}^2}\Big(\theta_2-\theta_1\Big) \quad , \tag{3.47}$$

and the homologous (3.15-3.16) in Kravchinsky et al. (2019),

$$P = \frac{z_{21}x_{21}}{z_{21}^2+x_{21}^2}\ln\frac{r_2}{r_1}+\delta\frac{z_{21}^2}{z_{21}^2+x_{21}^2}\Big(\alpha_2-\alpha_1\Big) \tag{3.48}$$

$$Q = \frac{z_{21}^2}{z_{21}^2+x_{21}^2}\ln\frac{r_2}{r_1}-\delta\frac{z_{21}x_{21}}{z_{21}^2+x_{21}^2}\Big(\alpha_2-\alpha_1\Big) \quad , \tag{3.49}$$

we can observe that the formulations differ for another term δ multiplying the difference $\alpha_2-\alpha_1$. If we are in the case (2), equations (3.44) and (3.45), we have $\delta=-1$, then the difference $\alpha_2-\alpha_1$ again leads back to $\theta_2-\theta_1$.

Hence, contrary to what pointed out by the authors, we have demonstrated that the formulation of Kravchinsky et al. (2019) does not differ from that of Talwani and Heirtzler (1962, 1964), rather it simply represents an algebraic variant, leading to identical results in terms of computed magnetic anomalies. For this reason, either formulations can be considered as a single approach and used without any distinctions. As a final consequence, the presumed analytical errors in the Talwani and Heirtzler's formulas has been disproved.

Regarding the Won and Bevis' formulation, it is not easily comparable in details to the other two from an analytical point of view, being derived from different assumptions and theoretical approach. However, in the following sub-section we compare it from a numerical point of view in order to understand whether its calculated magnetic response is always in agreement with that of the other algorithms.

3.3.2 Numerical Results

Two different numerical tests have been implemented using the above algorithm formulations (i.e., considering our rectified version for that of Kravchinsky et al. 2019) in order to achieve two different purposes, namely (a) to detect possible issues and irregularities in magnetic anomaly computation in a wide variety of random magnetic scenarios, and (b) to assess the results in a more realistic geological context upon sane magnetic scenarios, more helpful for geophysical applications.

The former purpose has been accomplished by means of a random changing-shape generation of up to five polygons repeated for 1000000 iterations (i.e., magnetic scenarios). In detail, both induced $\mathbf{M}_\mathrm{i}$ and $\mathbf{M}_\mathrm{r}$ remanent magnetization modules changing have been limited in a range between 0 and 50 $\mathrm{A/m}$, their inclination and declination respectively between -90° and 90° and between -180° and 180°. One hundred observation points have been located evenly spaced at a constant clearance of 10 m (toward up) along a profile 100 m long. Figure 3.3a shows one of these iterations (for the relative frequency of the magnetic properties tested see Figure 3.C.1).

During the test, a huge amount of combinations between the above magnetic properties have been sampled, showing in all cases full agreement between the three algorithms. Moreover, none anomalous or failing magnetic computations have been detected.

For what concern the second purpose, it has been carried out for the same number of iterations in a more realistic geological context like that modeled in Armadillo et al. (2020). The bodies modeled are three polygons with fixed geometries, representing a horst tectonic structure (Figure 3.3b). In this test, the random variation of both induced and remanent magnetization module has been restricted up to 5 $\mathrm{A/m}$, representing a realistic value for geophysical studies. The range of variation for the others magnetic properties is the same of the former test. The external bodies extend respectively up to -100000 and 100000 m in x direction to avoid “border effects”. Being these bodies represented by the same lithotype, we

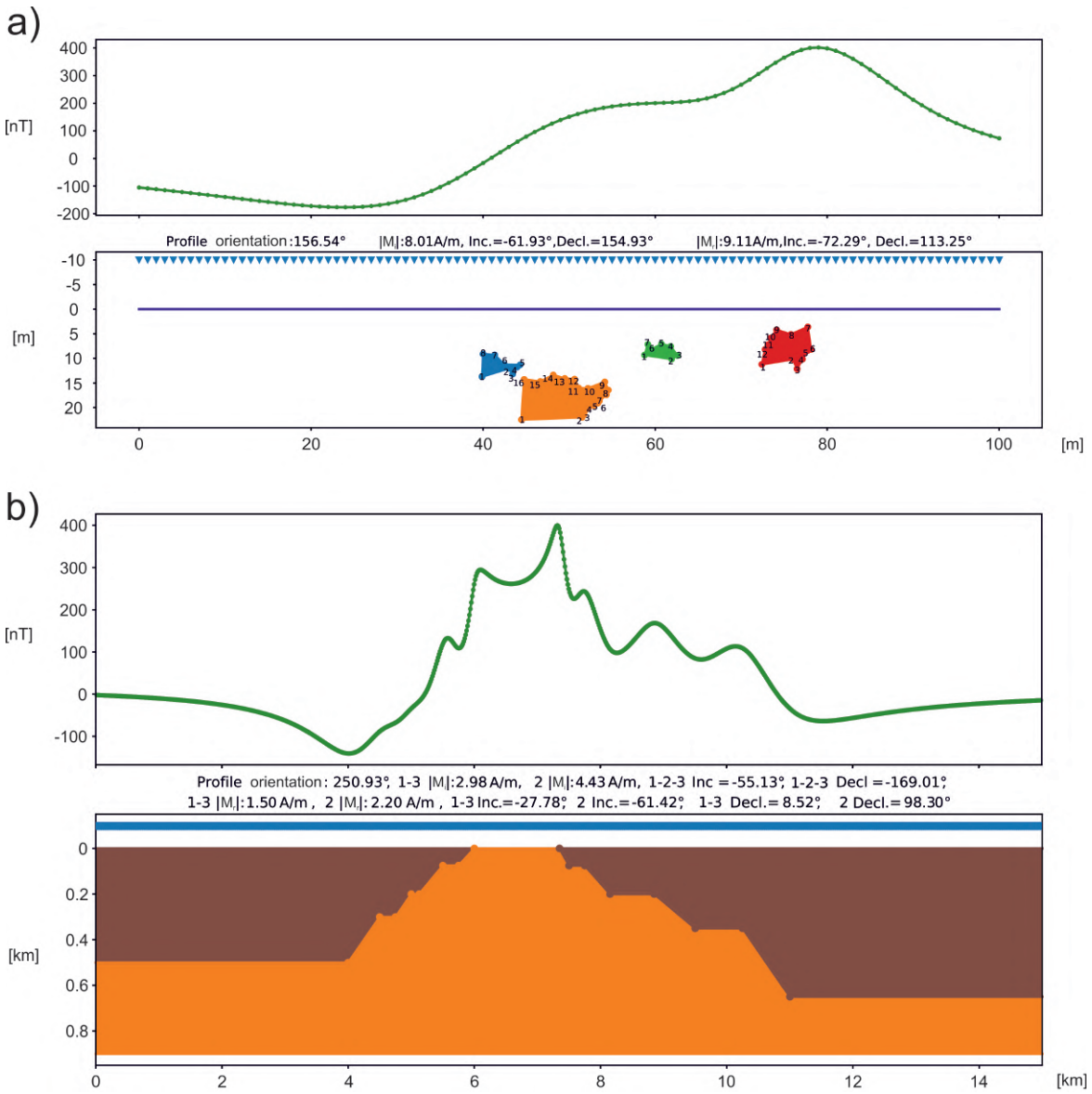

Figure 3.3 - (a) Magnetic responses (green curves), expressed in nT, due to four randomly generated polygons upon a magnetic scenario using the three algorithms of Kravchinsky et al. (2019), Talwani and Heirtzler (1962, 1964), and Won and Bevis (1987). In this forward model, representing an iteration of the former numerical test described in the main text, $|\mathbf{M}_i|$ and $|\mathbf{M}_r|$ represent the induced and remanent magnetization vector modules, whereas the abbreviation Inc. and Decl. their inclinations and declinations, respectively. The numbers around each polygon described the order and verse of calculation performed on its segments. The inverted triangles depict the observation points where the magnetic anomaly is calculated. (b) Forward magnetic model representing an iteration of the second numerical test in the case of a geological horst structure upon a random magnetic scenario. The body in orange (body 2) represents the horst body, surrounded by two other identical bodies (bodies 1 and 3 from left to right, in brown) for geological consistency. For the meaning of the abbreviations refer to the caption of the above Figure (a).

have assigned to them the same induced $\mathbf{M}_i$ and remanent $\mathbf{M}_r$ magnetization modules and the respective inclinations and declinations. For geological consistency, the central body is characterized by induced magnetization with same inclination and declination of that of the lateral bodies, but different module $|\mathbf{M}_i|$. In addition, it is characterized by different remanent magnetization module, inclination and declination. During each iteration, the magnetic properties randomly are changed following the rules described. One thousand observation points have been located evenly spaced at a constant clearance of 100 m (toward up) along a profile 15000 m long. Figure 3.3b presents one iteration relative to this analysis.

Even in this test, in all sampled cases there has been full agreement between the results of all the algorithms, with differences in magnetic anomalies in each observation point next to the machine precision of the computer utilized for these tests.

As result of both our numerical and analytical tests, we might confirm that the three formulations lead to the same results and no algorithm is advantageous over the other two, showing always to operate correctly and without abnormal behaviors. Moreover, the speed up in magnetic calculation originally obtained by Won and Bevis (1987) no longer has any advantage considering the much higher computing power of modern computers.

3.4 Conclusions

In this chapter, we have reviewed and compared the available formulations used to compute the magnetic anomaly caused by a 2D uniformly polarized body with polygonal section, both from an analytical and a numerical point of view. During the analytical analysis we have demonstrated that the formulation of Kravchinsky et al. (2019) does not differ from that of Talwani and Heirtzler (1962, 1964), being simply an algebraic variant. Indeed, the angle differences $\alpha_2 - \alpha_1$ in Kravchinsky et al. (2019) reduces in all cases to the difference $\theta_2 - \theta_1$ in Talwani and Heirtzler (1962, 1964). In addition, we have revealed and fixed some inaccuracies in Kravchinsky et al. (2019), that are: (a) the order of calculation around the

polygon sides, (b) the use of the cosine theorem formula, and (c) the projection of B_z and B_x along the Earth magnetic field vector, leading in case (b) often immediate termination of the algorithm during the numerical tests. During these tests, we have generated a huge number of magnetic scenarios in two different ways and purposes, namely (a) to investigate possible irregularities in magnetic anomaly computation for random-changing polygon numbers and geometries, and (b) to evaluate the utilization of the algorithms in realistic geological/tectonic contexts like that presented in Armadillo et al. (2020). In all cases, the three algorithms have behaved in the same manner without criticality, computing in all the sampled scenarios the same magnetic anomaly response. For this reason, the reader is free to follow the three approaches described without any preference.

Appendices

Introduction

Some physical inaccuracies have been found in the formulation of Kravchinsky et al. (2019) leading to failing magnetic anomaly calculation, that are in Appendix 3.A.1 the order of calculation around the polygon sides, in 3.A.2 the use of the cosine theorem formula and in 3.A.3 the projection of the vertical B_z and horizontal B_x magnetic strengths along the Earth magnetic field vector. In addition, Appendix 3.B illustrates the actual geometrical meaning of the angles involved in Kravchinsky et al. (2019) formulation and in 3.C the frequency of the magnetic properties sampled in the first numerical test described in the sub-Section 3.3.2 of the main text. Finally, Appendix 3.D provides more information about the code packages developed in the context of this work.

Appendix 3.A Inaccuracies found in Kravchinsky et al.'s derivation

3.A.1 Sense of calculation around polygons

The authors claimed that the calculation of the magnetic anomaly of a polygon should be performed considering its sides and vertices in a clockwise order. Following this approach, the resultant total magnetic anomaly T calculated for a polygon side will have a wrong opposite sign. In fact, from a physical point of view, it should correspond to having a semi-infinite lamina upon the polygon side in the opposite x direction, resulting in a negative scalar total field $(-T)$ contribution. Hence, the application of a minus sign to the formulas of B_z and B_x is required to rectify the results. On the contrary, considering the polygon sides and vertices in a counterclockwise order should avoid correcting the formulation. In fact, even Talwani and Heirtzler (1962, 1964) pointed out that considering the sides and vertices

clockwise their formulas for B_z and B_x should be changed adding a minus sign to obtain correct results.

3.A.2 Cosine theorem formula

The authors used the cosine theorem formula to calculate the module of the total magnetization vector **M**, called **J** by them, in the case of both induced and remanent magnetization as follow (p. 7349 in Kravchinsky et al. 2019)

$$J = J_i^2 + J_r^2 - 2J_iJ_r\cos(\Delta) \quad , \tag{3.50}$$

where Δ should represent the angle between J_i and J_r (Figure 3.A.1). However, using the formula (3.50), the result will be wrong. For this reason, the angle between J_r and J_i should be substituted by its conjugate $180^\circ - \Delta$ (Figure 3.A.1), leading to the correct formula

$$J = J_i^2 + J_r^2 - 2J_iJ_r\cos(180^\circ - \Delta) \quad , \tag{3.51}$$

or alternatively,

$$J = J_i^2 + J_r^2 + 2J_iJ_r\cos(\Delta) \quad . \tag{3.52}$$

Moreover, in some cases, this error may affect the calculation of the inclination A and declination B of J, defined as

$$A = \arcsin\left(\frac{J_i\sin(I) + J_r\sin(I_r)}{J}\right) \quad , \tag{3.53}$$

$$B = \arccos\left(\frac{J_i\cos(I)\cos(D) + J_r\cos(I_r)\cos(D_r)}{J\cos(A)}\right) \quad , \tag{3.54}$$

where I and D are the inclination and the declination of the Earth magnetic field (and also of the induced magnetization vector), whereas I_r and D_r the inclination and declination of the remanent magnetization vector respectively. In fact, when J becomes very small the argument of the trigonometric functions (3.53-3.54) may go out of domain $[-1,1]$, making it impossible the successful execution of the algorithm.

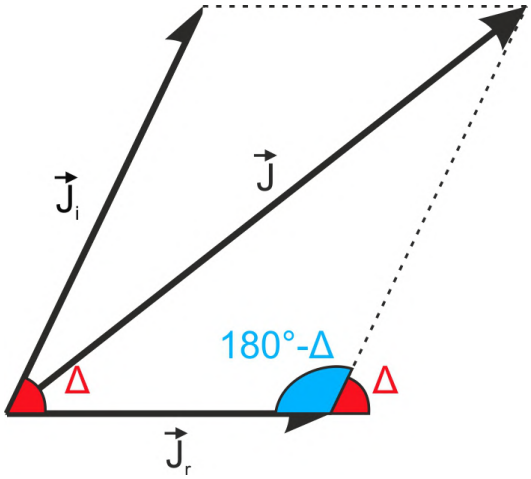

Figure 3.A.1 - Geometrical meaning of the Cosine theorem formula.

3.A.3 Projection onto the Earth's magnetic field

Kravchinsky et al. (2019) calculate the scalar total magnetic anomaly T of a polygon characterized both by induced and remanent magnetization as a projection of the vertical B_z and horizontal B_x magnetic strengths along the Earth magnetic field as follow

$$T = B_z \sin(A) + B_x \cos(A) \cos(C - B) \quad , \tag{3.55}$$

where A and B are the inclination and declination of the magnetization vector J (eq. 3.53-3.54) and C is the angle between the Geographic North and the direction of the profile along with the magnetic calculation is done. The above formula is correct only in case of induced magnetization alone, since in that case the angles A and B are equal to the inclination I and

declination D of the Earth magnetic field. Hence, the general formula to calculate T must perform the projection of B_z and B_x along the Earth magnetic field vector

$$T = B_z \sin(I) + B_x \cos(I) \cos(C - D) \quad . \tag{3.56}$$

Appendix 3.B Geometrical meaning of angles involved in Kravchinsky et al.'s formulae

The illustration 3.B.1 shows the graphical representation of the actual geometrical meaning of the angles involved in Kravchinsky et al. (2019) and Talwani and Heirtzler (1962, 1964) formulations. Let us remember the meaning of the following quantities,

$$\theta_1 = \arctan\left(\frac{z_1}{x_1}\right) ; \theta_2 = \arctan\left(\frac{z_2}{x_2}\right) ; g = \frac{x_{21}}{z_{21}} \quad . \tag{3.57}$$

As discussed in the main text, the angle difference $\alpha_2 - \alpha_1$ in Kravchinsky et al. (2019) always algebraically reduces to the difference $\theta_2 - \theta_1$ in Talwani and Heirtzler (1962, 1964).

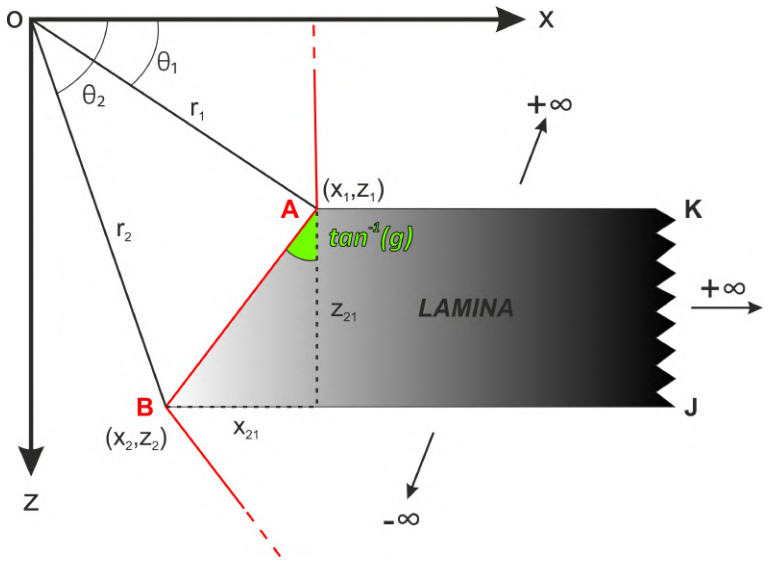

Figure 3.B.1 - Meaning of the angle g involved in the Kravchinsky et al.'s derivation.

Appendix 3.C Statistics about numerical tests discussed in the main text

In Figure 3.C.1 we show the statistics relative to the former numerical tests described in section 3.3.2. In detail, in the rose diagrams we illustrate the amount of inclination and declination values of the induced and remanent magnetization vectors sampled during 1000000 iterations, whereas in the histograms the quantity of the induced and remanent magnetization vectors modules. As you can see, virtually every possible magnetic scenario was generated during the test.

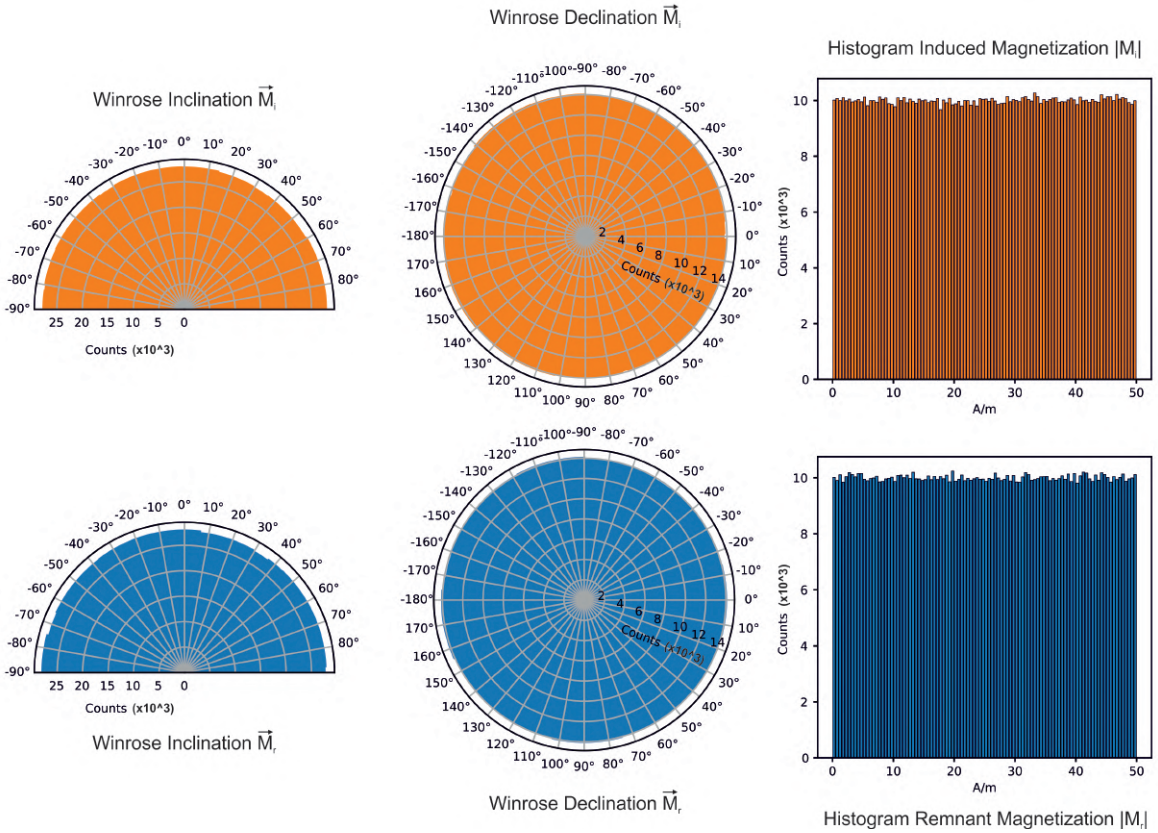

Figure 3.C.1 - Statistics on the 2D numerical test of Figure 3.3 in the main text.

Appendix 3.D Description of the software

The algorithms discussed in the main text have been implemented both in the Python and Julia languages in the open-source code packages pyMag2Dpoly and Mag2Dpoly. In the same code packages, all the inaccuracies found on the algorithm of Kravchinsky et al. (2019) about the sense of calculation around polygons, the use of the cosine theorem formula and the projection of polygons magnetic contributions onto the Earth's magnetic field have been fully fixed.

Chapter 4

Hamiltonian Monte Carlo Probabilistic Joint Inversion of 2D (2.75D) Gravity and Magnetic Data

Abstract

Two-dimensional modeling of gravity and magnetic anomalies in terms of polygonal bodies is a popular approach to infer possible configurations of geological structures in the subsurface. Alternatively to the traditional trial-and-error manual fit of measured data, here we illustrate a probabilistic strategy to solve the inverse problem. First we derive a set of formulae for solving a 2.75-dimensional forward model, where the polygonal bodies have a given finite lateral extent, and then we devise a Hamiltonian Monte Carlo algorithm to jointly invert gravity and magnetic data for the geometry and properties of the polygonal bodies. This probabilistic approach fully addresses the nonlinearity of the forward model and provides uncertainty estimation. The result of the inversion is a collection of models which represent the posterior distribution, analysis of which provides estimates of sought properties and may reveal different scenarios.

4.1 Introduction

Potential field data in the form of gravity and magnetic anomalies have been used for long to characterize the structure of the subsurface, ranging from applications to the small scale as in the context of exploration geophysics (e.g., Hinze et al., 2013; Li and Oldenburg, 1998, 2000; Nabighian et al., 2005; Zunino et al., 2009) to the continental scale, particularly to estimate heat flux or to infer crustal thickness (e.g., Baranov et al., 2018; Li et al., 2017; Llubes et al., 2018; Martos et al., 2017; Maule et al., 2005; Milano et al., 2020; Pappa et al., 2019; Scarponi et al., 2021; van der Meijde et al., 2013). Particularly popular for the easiness of use and interpretation are two-dimensional (2D) models, which allow the study of vertical cross-sections through the Earth. This approach has limitations with respect to fully 3D models (e.g., Blakely, 1996), nonetheless, it is capable of producing results which are easy to handle, compare with other geological information, and efficient from a computational point of view. Alternative approaches include trans-dimensional partitioning of the space in 3D (Ghalenoei et al., 2022), where spatial resolution is adapted locally.

For 2D models, there are essentially two main ways to parameterize the subsurface Blakely (1996): a cell-based approach, where the subsurface is subdivided into a finite number of homogeneous cells (e.g., Banerjee and Das Gupta, 1977; Bhattacharyya, 1964; Li and Oldenburg, 1998, 2000; Li et al., 2010; Nagy, 1966) and a polygon-based parameterization where contrasts in density or magnetization are represented by polygons (geological bodies) inside which density and magnetization are constant (e.g., Talwani and Heirtzler, 1964; Talwani et al., 1959). If the structures present in the subsurface can be approximated by such polygonal bodies, then this approach becomes advantageous with respect to cell-based parameterizations in that the number of model parameters is strongly reduced and the body is treated as a single entity. The cell-based approach, in contrast, requires a large number of cells to well represent a single homogeneous geological body and therefore in terms of numerical implementation it has large memory imprint and requires large matrix-vector

products. Other adaptive approaches in the context of trans-dimensional inversion are also possible (Hawkins and Sambridge, 2015; Luo, 2010; Ray, 2021), which aim at discovering parsimonious parameterizations.

In case of a polygonal parameterization of the subsurface, the typical workflow consists of manually adjusting the shapes of the polygons until a good fit with the observed data is obtained (e.g., de Moura et al., 2019; Kuang et al., 2022; Scheiber-Enslin et al., 2014; Tominaga et al., 2016). This procedure is performed by visualising on the screen a plot of the observed and calculated data together with a plot of the polygons whose vertices/edges are then displaced until a geologically plausible model that matches the observed data is found. Sometimes a mixed approach is applied (e.g., Witter et al., 2018), where inversion is iteratively applied to manually adjusted forward models constrained by surface geology and rock property data. The issue with such approaches is two-fold: (1) the results are strongly subjective, in that different users will produce different results lacking any metric for comparison and (2) the non-uniqueness and uncertainty of the inverse problem are not taken into account, giving the impression that one single solution is enough. Moreover, purely deterministic approaches are likely to fail to converge to a meaningful solution because of the nonlinearity of the forward model, as for the example we show in this work. Potential field data inversion, in fact, suffers from a strong non-uniqueness (e.g., Blakely, 1996), therefore constraints either on material properties or geometrical structure are required to obtain plausible solutions. Moreover, because of that, uncertainty quantification becomes necessary for appraisal of the solution.

To overcome the above mentioned issues, we present here a probabilistic strategy (Mosegaard and Tarantola, 2002; Tarantola, 2005) to perform a joint gravity and magnetic inversion capable of addressing the nonlinearity of the forward model and providing uncertainty quantification. To solve such inverse problem we thus resort to sampling the posterior distribution using the Hamiltonian Monte Carlo method (HMC) (Duane et al., 1987;

Fichtner et al., 2019; Neal, 2012). The algorithm strives to explore the model space according to the posterior distribution, producing a collection of posterior models. Such collection can then be analysed to answer a variety of questions, such as, for instance, the probability of a certain geological body to have a certain thickness or the probability of a certain parts of a polygon to be in a certain region. The main strength of HMC lies in the ability to exploit information about the shape of the posterior in order to steer the sampling trajectory towards high probability regions.

In the following we first describe how to perform forward calculations for both gravity and magnetic cases and then we illustrate our sampling strategy based on the HMC algorithm to solve the joint inversion problem. To validate our methodology we first perform a set of synthetic tests and then we show an application to a real data set.

4.2 The 2D to 2.75D gravity and magnetic anomaly problem

Algorithms to compute gravity and magnetic anomalies for 2D polygonal bodies based on line integrals (Hubbert, 1948) date back to Talwani et al. (1959) and Talwani and Heirtzler (1964). Since then, such formulations have been the basis for the majority of the computer programs performing such calculations (a review can be found in chapter 3).

In this work, we focus on an extension of purely 2D polygonal forward problems to 2.5D and 2.75D. In the 2D case, the polygonal bodies are assumed to extend to infinity in both directions normal to the plane where the polygon lies. Such setup may be difficult to apply in a realistic framework, where geological bodies have a finite extent which strongly influences the measured signal. For this reason, a 2.5D modelling strategy has been developed, which takes into account a finite lateral extension (extrusion) of the polygonal bodies. The label 2.5D refers to the situation in which such lateral extension is the same on both sides with respect to the polygons, while 2.75D refers to models where the lateral extension normal to the plane of the polygon is different for the two sides. Formulae for 2.5D and 2.75D have

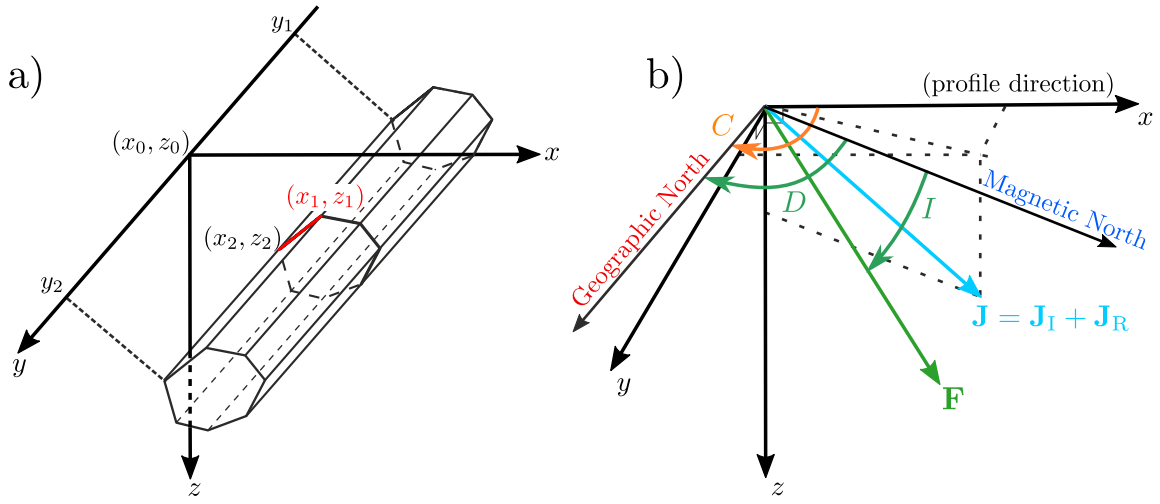

Figure 4.1 - Geometrical setup for 2.75D anomaly calculations. See main text for details.

been presented across the 70s to the 80s (see, e.g., Cady, 1980; Rasmussen and Pedersen, 1979; Shuey and Pasquale, 1973).

The geometrical setup for the 2.75D problem is illustrated in Figure 4.1a, where the polygon(s) lies in the x,z plane, while y denotes the axis along which the body extends for a finite length. Formulae for the 2.75D gravity and magnetic anomalies in the original formulation case Campbell (1983); Rasmussen and Pedersen (1979) are cumbersome so, for convenience, we provide here a slightly modified version which appears simpler to read and implement. A detailed derivation can be found in the Appendix 4.A. The formulae that we are presenting below are used to compute the gravity and magnetic response for a polygonal body which extends along the y axis from the position y_1 to y_2. The following formulae, modified from Rasmussen and Pedersen (1979), are for a single polygonal body. In case of presence of multiple polygons, the contributions are added up. The two points (x_i, z_i) and (x_{i+1}, z_{i+1}) represent the endpoints of an edge of the polygon. The order in which the vertices are taken is very important. In our case, with reference to Figure 4.1, the first point (x_1, z_1) must refer to the beginning of the segment in the anti-clockwise direction and the other point (x_2, z_2) to the end of the segment, again considering the anti-clockwise direction.

In the following we assume that the polygon has N vertices and that for the case $i = N$ we have $x_{N+1} = x_1$ and $z_{N+1} = z_1$.

The formula for the vertical gravitational attraction of a polygon as the result of a summation over all the edges is given by

$$g_z = -\rho\, G \sum_{i=1}^{N} \Big\{ \cos(\phi)\,(y_2\, s_2 - y_1\, s_1) + \left(\frac{x_i\, z_{i+1} - z_i\, x_{i+1}}{\sqrt{x_{21}^2 + z_{21}^2}} \right) \times \Big[\cos(\phi)\,(a_2 - a_1) - \sin(\phi)\,(l_1 + l_2) \Big] \Big\} \quad , \tag{4.1}$$

where $G \approx 6.67 \cdot 10^{-11}\ \mathrm{Nm^2/kg^2}$ is the gravitational constant and ρ is the density (contrast) of the polygonal body (in $\mathrm{kg/m^3}$). For the magnetic case, instead, there are three components which need to be calculated to get the final total field anomaly (modulus), which are given by

$$\begin{aligned} B_x &= \sum_{i=1}^{N} \Big\{ -\sin(\phi) \Big[(l_1 + l_2)\,(\cos(\phi) J_x + \sin(\phi) J_z) \\ &\quad -(a_2 - a_1)\,(\cos(\phi) J_z - \sin(\phi) J_x) - J_y\,(q_1 - q_2) \Big] \Big\}, \qquad (4.2) \\ B_y &= \sum_{i=1}^{N} \Big\{ J_y\,(a_2 - a_1) - (q_1 - q_2)\,(\cos(\phi) J_z - \sin(\phi) J_x) \Big\}, \qquad (4.3) \\ B_z &= \sum_{i=1}^{N} \Big\{ \cos(\phi) \Big[(l_1 + l_2)\,(\cos(\phi) J_x + \sin(\phi) J_z) \\ &\quad -(a_2 - a_1)\,(\cos(\phi) J_z - \sin(\phi) J_x) - J_y\,(q_1 - q_2) \Big] \Big\}. \qquad (4.4) \end{aligned}$$

The final formula for the total field anomaly is then

$$\begin{aligned} \Delta T &= \frac{1}{4\pi} \Big[B_x \cos(I_{\mathrm{ind}}) \cos(C - D_{\mathrm{ind}}) \\ &\quad + B_y \cos(I_{\mathrm{ind}}) \sin(I_{\mathrm{ind}}) + B_z \sin(I_{\mathrm{ind}}) \Big] \quad , \end{aligned} \tag{4.5}$$

where J_x, J_y and J_z, are the components of the magnetization ($\mathrm{A/m}$) of the polygonal body, I_{ind} and D_{ind} the inclination and inclination of the inducing regional field ($\mathbf{F}$), respectively, and,

finally, C the angle with respect to the direction of the geographical North (see Figure 4.1b). $\mathbf{J}$ is computed as the vector sum of induced and remnant magnetization.

The quantities appearing above in the gravity and magnetic case are given by the following definitions,

$$l_1 = \ln\left(\frac{r_1\,(\sqrt{r_2^2+y_1^2}-y_1)}{r_2\,(\sqrt{r_1^2+y_1^2}-y_1)}\right), \quad l_2 = \ln\left(\frac{r_1\,(\sqrt{r_2^2+y_2^2}+y_2)}{r_2\,(\sqrt{r_1^2+y_2^2}+y_2)}\right), \tag{4.6}$$

$$s_1 = \ln\left(\frac{u_2+\sqrt{r_2^2+y_1^2}}{u_1+\sqrt{r_1^2+y_1^2}}\right), \quad s_2 = \ln\left(\frac{u_2+\sqrt{r_2^2+y_2^2}}{u_1+\sqrt{r_1^2+y_2^2}}\right), \tag{4.7}$$

$$q_1 = \frac{1}{2}\ln\left(\frac{(\sqrt{r_2^2+y_1^2}-u_2)\,(\sqrt{r_1^2+y_1^2}+u_1)}{(\sqrt{r_2^2+y_1^2}+u_2)\,(\sqrt{r_1^2+y_1^2}-u_1)}\right), \tag{4.8}$$

$$q_2 = \frac{1}{2}\ln\left(\frac{(\sqrt{r_2^2+y_2^2}-u_2)\,(\sqrt{r_1^2+y_2^2}+u_1)}{(\sqrt{r_2^2+y_2^2}+u_2)\,(\sqrt{r_1^2+y_2^2}-u_1)}\right), \tag{4.9}$$

$$a_1 = \arctan\left(\frac{u_2\,y_1}{w\sqrt{r_2^2+y_1^2}}\right) - \arctan\left(\frac{u_1\,y_1}{w\sqrt{r_1^2+y_1^2}}\right), \tag{4.10}$$

$$a_2 = \arctan\left(\frac{u_2\,y_2}{w\sqrt{r_2^2+y_2^2}}\right) - \arctan\left(\frac{u_1\,y_2}{w\sqrt{r_1^2+y_2^2}}\right), \tag{4.11}$$

where

$$x_{21} = x_{i+1} - x_i, \quad z_{21} = z_{i+1} - z_i, \tag{4.12}$$

$$u_1 = \cos(\phi)\,x_i + \sin(\phi)\,z_i, \tag{4.13}$$

$$u_2 = \cos(\phi)\,x_{i+1} + \sin(\phi)\,z_{i+1}, \tag{4.14}$$

$$w = -\sin(\phi)\,x_i + \cos(\phi)\,z_i, \tag{4.15}$$

$$\phi = \arctan\left(\frac{z_{21}}{x_{21}}\right), \quad r_1 = \sqrt{u_1^2+w^2}, \quad r_2 = \sqrt{u_2^2+w^2}\,. \tag{4.16}$$

The formulae above allow us to solve the forward problem, i.e., to compute the gravity and magnetic anomalies given the position of the vertices of the polygons and their density and magnetization and are those implemented in our software.

4.3 Probabilistic joint inversion using the Hamiltonian Monte Carlo method

4.3.1 Hamiltonian Monte Carlo scheme

Under fairly general assumptions and within the framework of the probabilistic approach (Mosegaard and Tarantola, 2002), where information is treated in terms of probability density functions (PDF), the solution to an inverse problem can be written as

$$\sigma(\mathbf{m}) = k L(\mathbf{m}) \rho(\mathbf{m}), \tag{4.17}$$

where $\mathbf{m}$ represents the model parameters, k a normalization constant, $\sigma(\mathbf{m})$ is the posterior PDF, $L(\mathbf{m})$ the likelihood function representing the degree of fit between observed and calculated data and $\rho(\mathbf{m})$ the prior information on model parameters (see, e.g., Tarantola, 2005). Characterizing the posterior PDF is the target of the inversion process. Moreover, within this approach, it is possible to easily integrate different kinds of geophysical information (Hansen et al., 2016), hence performing a joint inversion of gravity and magnetic anomalies is a natural choice. In this work the likelihood function, including gravity and magnetic data, is defined as

$$\begin{aligned} L(\mathbf{m}) = k^{\text{grav}} \exp\left(-\frac{1}{2} \left(\mathbf{g}^{\text{grav}}(\mathbf{m}) - \mathbf{d}^{\text{grav}}\right)^{\mathrm{T}} \left(\mathbf{C}_{\mathrm{D}}^{\text{grav}}\right)^{-1} \left(\mathbf{g}^{\text{grav}}(\mathbf{m}) - \mathbf{d}^{\text{grav}}\right) \right) \\ \times k^{\text{mag}} \exp\left(-\frac{1}{2} \left(\mathbf{g}^{\text{mag}}(\mathbf{m}) - \mathbf{d}^{\text{mag}}\right)^{\mathrm{T}} \left(\mathbf{C}_{\mathrm{D}}^{\text{mag}}\right)^{-1} \left(\mathbf{g}^{\text{mag}}(\mathbf{m}) - \mathbf{d}^{\text{mag}}\right) \right), \end{aligned} \tag{4.18}$$

where $\mathbf{g}(\mathbf{m})$ is the forward model for gravity ($\cdot^{\text{grav}}$) and magnetic ($\cdot^{\text{mag}}$) anomalies, $\mathbf{d}$ the observed (measured) data, $\mathbf{C}_{\text{D}}$ a covariance matrix representing the uncertainty on the measured data.

The model parameters $\mathbf{m} = \{\mathbf{m}^{\text{vert}}, \mathbf{m}^{\text{grav}}, \mathbf{m}^{\text{mag}}\}$ are defined as being either the position of the vertices of the polygonal bodies (see previous section) or the values of induced and remanent magnetization, density or all of them. In case the vertices are considered unknown model parameters, the relationship between $\mathbf{m}^{\text{vert}}$ and the computed data $\{\mathbf{g}^{\text{mag}}(\mathbf{m}), \mathbf{g}^{\text{grav}}(\mathbf{m})\}$ is strongly nonlinear, hence sampling methods are required to characterize the posterior PDF. Such nonlinearity, in fact, may produce a multi-modal posterior PDF with different local maxima, which might not be easily dealt with using conventional optimization methods. An example of this is discussed in section 4.4.1. Moreover, potential field inverse problems suffer from a strong intrinsic non-uniqueness that allows different models to produce the exact same observable data (e.g., Blakely, 1996; Hinze et al., 2013). Because of this, the idea is to explore as much as possible the model space for plausible solutions, given the constraint of a finite number of iterations. Prior information derived from geological knowledge of the area under study and laboratory measurements on rock samples thus play a fundamental role to reduce the ambiguity for potential field data.

In light of the above, in order to characterize $\sigma(\mathbf{m})$, we sample it using a Monte Carlo algorithm which produces a large collection of models. Sampling in this case means producing a collection of models whose "density" in the model space is proportional to the actual value of the posterior PDF (Tarantola, 2005). Statistical analysis is then performed on such collection to extract information about features of interest, for example by computing expectations. To maximize efficiency, we sample the posterior using with the HMC method (Duane et al., 1987; Fichtner et al., 2019; Neal, 2012), which combines the sampling strategy with information derived from the gradient of the misfit function (the negative logarithm of the posterior distribution) with respect to the model parameters. The use of information

derived from the gradient may substantially increase the efficiency of the algorithm compared to other traditional techniques such as the random walk Metropolis algorithm (RWM) (Metropolis et al., 1953; Mosegaard and Tarantola, 1995; Robert, 2015). The gradient, in fact, helps steering the exploration of the posterior PDF towards areas of high probability and allows for longer moves compared to RWM, at the expense of being able to compute such gradient efficiently (Fichtner et al., 2019).

The HMC strategy is based on an analogy with a physical system described in terms of potential and kinetic energy, where a multi-dimensional particle moves frictionless on a landscape defined by the potential energy $U(\mathbf{m})$, where $\mathbf{m}$ represents the position and $\mathbf{p}$ the momentum of the particle, related to the kinetic energy $K(\mathbf{p})$. The coordinates of the particle (position) are the model parameters, while the potential energy equals the misfit of the posterior PDF, $U(\mathbf{m}) = -\log(\sigma(\mathbf{m}))$. The kinetic energy is usually defined as being the negative logarithm of a Gaussian PDF, i.e., $K(\mathbf{p}) = -\log(\mathcal{N}(\mathbf{m},\mathbf{M})) = \frac{1}{2}\mathbf{p}^{\mathrm{T}}\mathbf{M}^{-1}\mathbf{p}$, where $\mathbf{M}$ is the mass matrix, a covariance matrix representing the scaling and correlations of the momentum variables. The system preserves the value of the Hamiltonian $H(\mathbf{m},\mathbf{p}) = U(\mathbf{m}) + K(\mathbf{p})$ and evolves according to the Hamiltonian dynamics, given by the following equations:

$$\frac{\partial \mathbf{m}}{\partial t} = \frac{\partial H}{\partial \mathbf{p}}, \quad \frac{\partial \mathbf{p}}{\partial t} = -\frac{\partial H}{\partial \mathbf{m}}, \tag{4.19}$$

where t represents a fictitious time. Equations (4.19) need to be integrated in time to calculate the motion of the particle and hence to update position and momentum in time. The evolution of the position in time represents the trajectory in the model space of the visited models. The HMC algorithm proceeds at each iteration by sampling a value for the momentum from its distribution and then updating position and momentum using the Hamiltonian dynamics for a certain amount of time. Position and momentum at the end of the trajectory are then used as candidate values for the new state of the Markov chain. Theoretically the Hamiltonian is conserved in such system, however, in practice, numerical integration using the leap-frog or

any other practical scheme (Neal, 2012) introduces some errors which require the use of a Metropolis step (Metropolis et al., 1953) where a probabilistic rule decides whether to accept the new candidate state or fall back to the previous one. The properties of the Hamiltonian dynamics and the leap-frog integration scheme guarantee that the *detailed balance* property is satisfied and hence the algorithm is a proper sampler (Neal, 2012).
Summarizing, at each iteration the algorithm performs a certain number of steps in time solving the Hamiltonian dynamics numerically and then uses position (model parameters) and momentum at the end of the trajectory as candidate values for the next state of the chain. Details on how the algorithm works can be found in Betancourt 2017, Fichtner et al. 2019, and Neal 2012.

The mass matrix $\mathbf{M}$ is a very important tuning parameter for HMC (see, e.g., Fichtner et al., 2021), since it provides an estimate of the perturbations to be applied to the momentum and hence the position (see equation 4.19) and enables the user to control the smoothness of the proposed updates, as we will see in section 4.4.1. In addition, two other parameters control the numerical integration of the Hamiltonian dynamics: the step length ε and the number of leap-frog iterations L.

4.3.2 Software implementation and computation of the gradient with automatic differentiation

The inverse approach described in this chapter has been implemented in a set of open source software packages written in the Julia language (Bezanson et al., 2017) (details are provided in Appendix 4.C). These packages are part of a larger project dubbed "HMCLab" aiming at providing a set of geophysical forward problems which can be used to set up HMC inversions, which is the subject of a paper in preparation (Zunino A., Gebraad L., Ghirotto A. and Fichtner A., pers. comm.). For the inversions shown in this work we use a particular flavor of HMC, namely the NUTS algorithm (also part of HMCLab) (Hoffman and Gelman,

2014), which aims at self-tuning the step length and number of iterations of the leap-frog scheme.

The critical step for a successful HMC algorithm is the capability of computing the gradient of the potential energy efficiently enough such that the algorithm can perform the desired number of iterations in a reasonable amount of time. In our case, computing derivatives of the forward models with respect to vertices position by hand is rather cumbersome, so, for convenience, we resort to the technique of automatic differentiation (AD) (Gebremedhin and Walther, 2020; Griewank and Walther, 2008; Sambridge et al., 2007). AD is a computational technique which allows us to automatically generate the derivative of a user-provided function, commonly happening on-the-fly, for almost any code in a given language where this tool is available. Such procedure is also useful in case there are any changes in the functions solving the forward problem in that the derivatives would be readily available. There are two flavors of AD: forward and reverse mode, which differ in the way they traverse the chain rule used to decompose the derivative of the function of interest. Our code can use either of them, however, in our examples, we found the forward mode to be more stable and efficient. Trial runs should be conducted by the user for any particular problem to determine the best strategy.

One important issue that may arise when updating the shape of the polygons using the gradient is that of physically impossible geometries (self-intersecting polygons, etc.). We provide information on how we deal with that in Appendix 4.B.

4.4 Results

In this section we describe two synthetic and one real data examples of joint inversion with HMC. Additionally, we show an attempt to solve the first synthetic example with a deterministic method. In the following, for simplicity, the prior $\rho(\mathbf{m})$ is assumed to be an

unbounded, uniform PDF, however, any other form of prior information could be used within this algorithm.

4.4.1 Numerical experiments

The first numerical experiment we present is a 2.75D joint inversion of a gravity and magnetic anomaly profile consisting of 100 observation points at an altitude of 100 meters for a total of 100 measurements of the total magnetic field and 100 measurements of the vertical gravitational attraction. The "observed" data in this synthetic test were calculated from a hexagonal- and a tilted rectangle-shaped polygonal bodies (Figure 4.2a in black), mimicking a blob anomaly and a dike intrusion, with the addition of Gaussian correlated noise to simulate the error on realistic measurements (see Figure 4.2a for the geometry of the problem). The lateral extent of the model is estimated to be 5 km in the positive y direction and 1 km in the negative direction. In this example we assume to know the values of induced magnetization ($|\mathbf{J}|_{\text{ind}} = 2\text{A/m}$, $I_{\text{ind}} = 45°$, $D_{\text{ind}} = 0°$), remanent magnetization ($|\mathbf{J}|_{\text{rem}} = 0$) and density contrast ($1000\,\text{kg/m}^3$) of the polygonal bodies and therefore we invert only for the position of the vertices. Inverting for all possible parameters with little constraints is difficult because of the strong trade-off among them, which will likely generate such a wide spectrum of models to become difficult to interpret.

We first attempt to perform an inversion using a completely deterministic, gradient-based method, specifically a L-BFGS method (Nocedal and Wright, 2006). The parameters used and the starting model are the same than those used for the HMC examples. Figure 4.2 shows the found "optimal" model after 372 iterations in orange. The shape of this solution is far from the reference model and geologically implausible, although the fit to the observed data is good. This shows how difficult it is to obtain a reliable solution with a deterministic method and, comparing with the following results, how much information may be missed with a single "best" solution for this kind of problems.

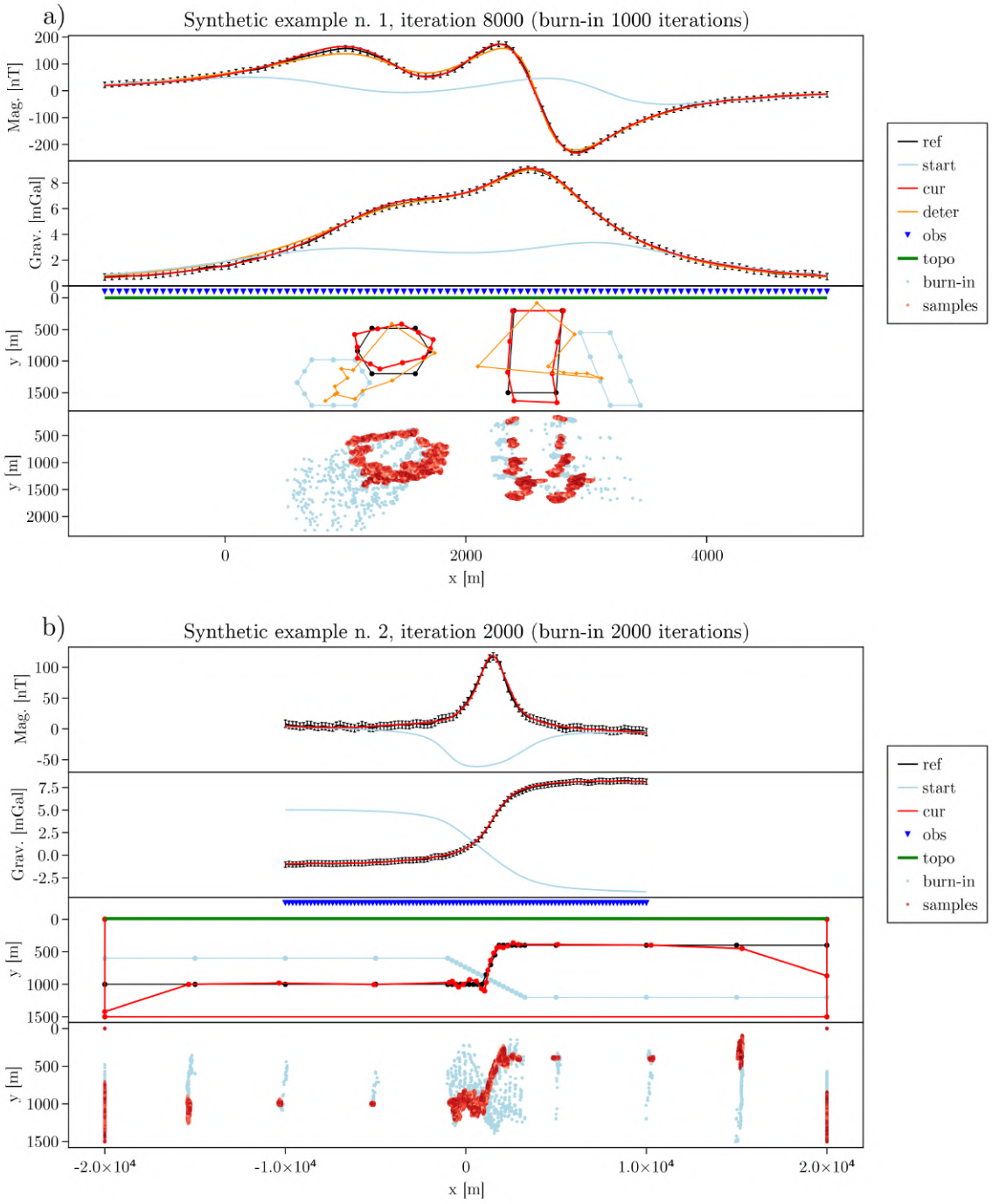

Figure 4.2 - Selected models and data at given iterations from the joint inversion synthetic tests. The labels "ref", "start", "cur" and "deter" refer to the reference, starting model, current model and the deterministic solution, respectively, and their gravity and magnetic responses. Panel (a) depicts the first synthetic test involving two polygonal bodies. The observed magnetic and gravity data are shown in the first and second plot from the top, while the polygonal bodies in the third. The fourth plot from the top shows the position of the vertices across the iterations during and after the burn-in phase, where darker red means a better fit to the observed data (higher posterior PDF). Panel (b) depicts the second synthetic test mimicking a fault region. The structure of the plots is the same than for panel (a).

We now discuss the inversion using HMC, specifically using the NUTS algorithm (see above). The starting model (Figure 4.2a in light blue) consists of and exagonal polygon located deeper and to the left of the reference model (Figure 4.2a in black) and a dike-like polygon tilted in the opposite direction than the reference model. Notice that the reference model is parameterized with $6+4$ (exagon plus rectangle, respectively) parameters, while the actual inverse problem is overparameterized with $12+8$ parameters to simulate a more realistic setup where the number of edges is unknown. Starting from the initial model, we ran 10000 iterations. The diagonal of the mass matrix $\mathbf{M}$ (see above) was set to a range of values corresponding to a correlation length of the model parameters of roughly 300 m, which is the variation we expect to see in the solutions. Moreover, in this example, we assume that we have a rough idea of the shapes of the anomalous bodies we expect to be in the subsurface. To inject such kind of information into the inverse algorithm, we introduce some correlation in the mass matrix $\mathbf{M}$, i.e., we have non-zero off-diagonal terms. The result is that the update to a vertex position influences also the position of the other vertices by an amount proportional to the off-diagonal values of the mass matrix. An approximately similar kind of information could also be injected into the algorithm by employing a Gaussian prior PDF by specifying an appropriate covariance matrix.

The results show that the algorithm, despite starting rather far from the reference model, converges to a good solution after about only 200 iterations, with a very large decrease of the misfit. We show in Figure 4.2a) bottom plot all the positions of the vertices during the iterations. The ones belonging to the burn-in phase of the algorithm are marked in light blue, while the following values (samples) in red. As expected in potential field problems, the top part of the polygons is better constrained than the bottom (Figure 4.2a) because of a higher sensitivity at shallower depths.

For the second synthetic example (see Figure 4.2b) we invert a combination of gravity (100 observations) and magnetic data (100 observations) for the position of the vertices

assuming again known induced magnetization ($|\mathbf{J}|_{\text{ind}} = 1\text{A/m}$, $I_{\text{ind}} = 45°$, $D_{\text{ind}} = 0°$ for the first body and $|\mathbf{J}|_{\text{ind}} = 2\text{A/m}$, $I_{\text{ind}} = 45°$, $D_{\text{ind}} = 0°$ for the second body), remanent magnetization ($|\mathbf{J}|_{\text{ind}} = 0$) and density contrast ($-150\text{kg/m}^3$ for the first body and 250kg/m^3 for the second body). The observation points are at an altitude of 250 m and the model extends from the surface to about 1500 m of depth. Again, correlated Gaussian noise has been added to the "observations". From the geometrical point of view, instead, the problem is quite different. In this case the geological setup we are mimicking is that of a fault between two layers of different properties (see Figure 4.2b). The fault model extends along x much more than the span of observation points in order to avoid strong edge effects on the calculated signal. In this case the y direction extends to infinity and hence we use a 2D approach. The starting model features a fault which is longer and tilted the opposite way with respect to the reference model (Figure 4.2b).

Starting from the initial model, we ran 10000 iterations using the NUTS algorithm. The algorithm takes about 300 iterations to flip the angle of the fault to the reference one and then starts to produce models that are close to the reference model. This example shows how the algorithm is capable of finding good models even if the starting model is far away from the reference one. Figure 4.2b bottom plot shows the position of the vertices throughout the iterations, showing only relatively small variations, indicating that for this data set, assuming approximately known material properties, there is a limited range of variations which fit the observed data to a good degree.

4.4.2 Real data example

Finally, we present a 2.75D inversion of a gravity and magnetic anomaly relative to an inferred cooled magmatic pluton located in the Rufiji Through, a E-W trending graben structure cutting the Tanzanian southeastern coastal sedimentary basin (Armadillo et al., 2020). In such a context, the use of a more realistic 2.75D formulation to compute the forward gravity

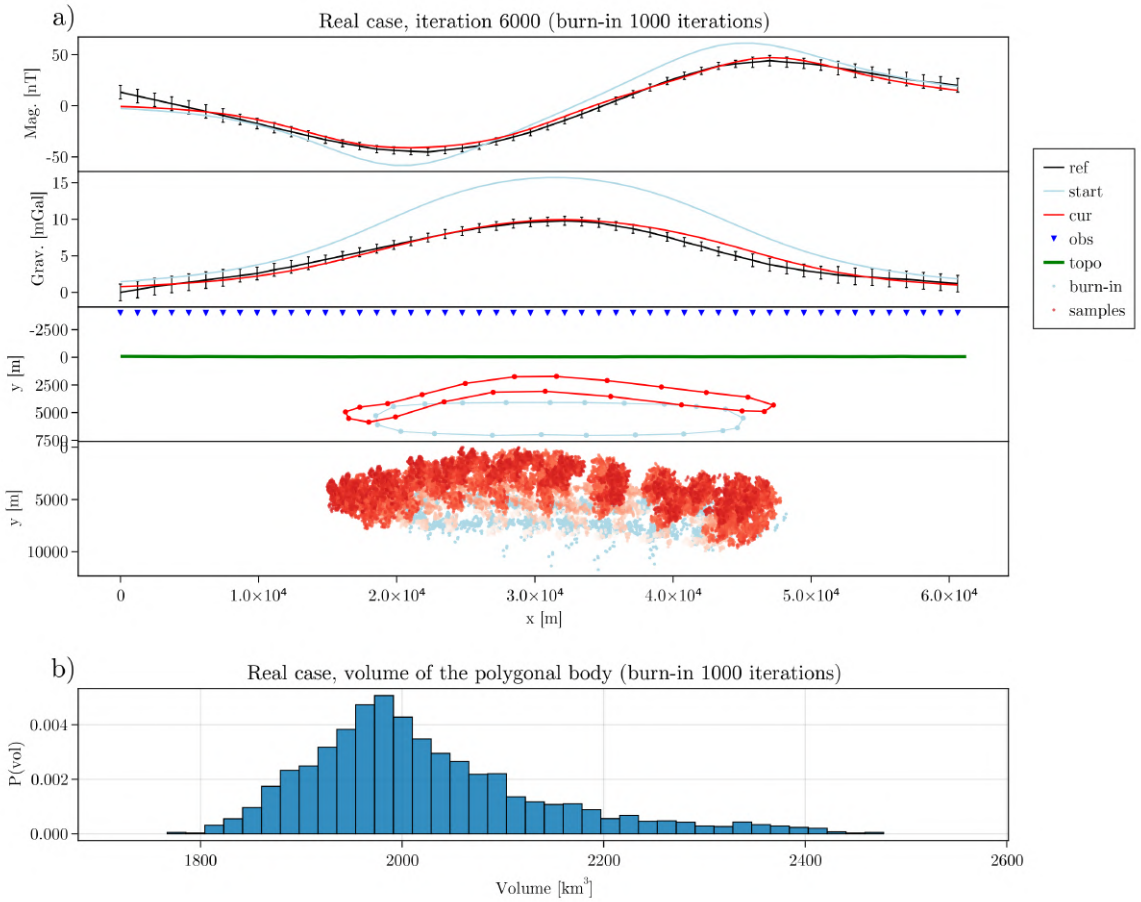

Figure 4.3 - Real data set inversion illustration. The plots relative to panel a) are analogous to those for figure 4.2a). Panel b) shows a histogram of the volume of the polygonal body calculated from the collection of the posterior models.

and magnetic response is crucial, as the target body is of finite lateral extension and therefore the pure 2D hypothesis would no longer hold true. The data sets used are the World Gravity Map (WGM) compilation (Bonvalot et al., 2012) and the total field magnetic anomaly data EMAG2 (Meyer and Saltus, 2016). The gravity data has been upward continued at 4 km to match the height of the magnetic data set and obtain similar sensitivity. This processing has been performed in order to reduce the high-frequency content of the signal and reach a balance with the magnetic data in terms of information content. The 2D gravity anomaly map (see Figure 3 in Armadillo et al. (2020)), shows an almost perfect circular shape, whereas the magnetic one presents a dipolar pattern with axis aligned approximately to the current Earth's Magnetic Field direction. This evidence suggests the pluton presents dominant induced magnetization or even remnant magnetization aligned to the current Earth's Magnetic Field.

The data sets have been sampled at 100 points evenly spaced along a profile ∼60 km long crossing the anomaly with an angle of 0 degrees with respect to the Geographic North, in close accordance with the declination of the present day Earth's Magnetic Field in that place (i.e., -2.38 degrees). This orientation of the profile has been chosen in order to better sample the dipolar pattern in the magnetic data. We ran 10000 iterations of the NUTS algorithm, starting from a plausible polygonal body given the available geophysical information for the area (see Figure 4.3a). The lateral extent (along y) of the model is estimated to be 25 km in both directions (equivalent to a 2.5D approach). In this case we invert for both the position of the vertices and the magnetic and gravity properties (starting with $|\mathbf{J}|_{\text{ind}} = 1.235\,\text{A/m}$, $I_{\text{ind}} = -37.45°$, $D_{\text{ind}} = -2.39°$; $|\mathbf{J}|_{\text{rem}} = 0\,\text{A/m}$, $\rho = 250\,\frac{kg}{m^3}$). However, as explained above, the strong trade-off among these parameters allows only for an inversion with a limited range of variability of such rock properties. The results of the inversion show a range of possible locations of the polygonal body, either deeper than the starting model (in the first phase of sampling) or shallower but with a pronounced curved shape for the rest of the iterations. In panel b) of Figure 4.3 we show a histogram of the probability of the volume of the polygonal

body to be in a certain range, which has been calculated analysing the collection of posterior models (samples). The plausibility of such result is obviously dependent on how realistic are the initial assumptions (e.g., knowledge of rock properties). This is an example of the kind of information that can be provided by the probabilistic method also thanks to the 2.75D formulation of the forward model, which allows for a finite lateral extent of the prismatic bodies under study. This property, useful in different contexts such as sedimentary basins, could not be calculated using the purely 2D formulation.

4.5 Conclusion

In this chapter we addressed the problem of inverting jointly gravity and magnetic anomaly data with a 2.75D (including 2D and 2.5D) parameterization in terms of polygonal bodies. The position of the vertices of the polygons is nonlinearly related to the gravity and magnetic response measurable on or above the Earth's surface. Because of this, the inverse problem results nonlinear even for a classic Gaussian misfit function. Our inversion method therefore relies on a sampling strategy that aims at characterizing the posterior distribution rather than searching for single optimal model. In light of the above we have shown how to set up a joint gravity and magnetic inversion using the Hamiltonian Monte Carlo method, which provides as a final solution a collection of sample models amenable to statistical analysis. Both the controlled synthetic tests and the application to real data presented in this chapter show that a probabilistic inversion is feasible and can provide useful quantitative information about the subsurface. We have implemented the methodology described in this chapter in a set of open source software packages which are publicly available.

Appendices

Introduction

The Appendices below contain a detailed mathematical description and derivation of the formulae used in the related main text, an illustration of potential geometrical issues for polygons and a description of the software.

Appendix 4.A 2.75D gravity and magnetic anomalies formulae derivation

The first popular formalism to compute the vertical gravitational attraction and the total scalar magnetic anomaly of a 2D polygonal structure were proposed by Talwani et al. (1959) and Talwani and Heirtzler (1964), respectively. These works rely on the theory of the line integral of Hubbert (1948), thanks to which the gravity and magnetic response of a laterally infinitely elongated prismatic body of uniform physical properties (i.e., density and magnetization) can be calculated at requested observation points along a profile. The 2D polygonal assumption, very common in potential field modelling, allows to 1) decrease dramatically the model complexity and 2) better define the spatial geometry of the causative body. Following the above mentioned early 2D formalisms, Shuey and Pasquale (1973), Rasmussen and Pedersen (1979) and Cady (1980) proposed new formulations for the so-called *End Corrections* to allow geophysicists to model prismatic bodies with finite lateral extent (normal to the polygonal bodies), but still represented by polygonal sections as used for the 2D case. Later on, Campbell (1983) found a sign error in the formulation for the magnetic case of Rasmussen and Pedersen (1979), coding a rectified version of the algorithm in the computer program *NEWMAG*.

In the most general case, the basic assumption for *End Corrections* is to divide a prismatic body in two prismatic semi-bodies elongated perpendicularly to the profile direction from $y = y_1 < 0$ to $y = 0$ and from $y = 0$ to $y = y_2 > 0$ respectively (Figure 4.A.1). Hence, we can

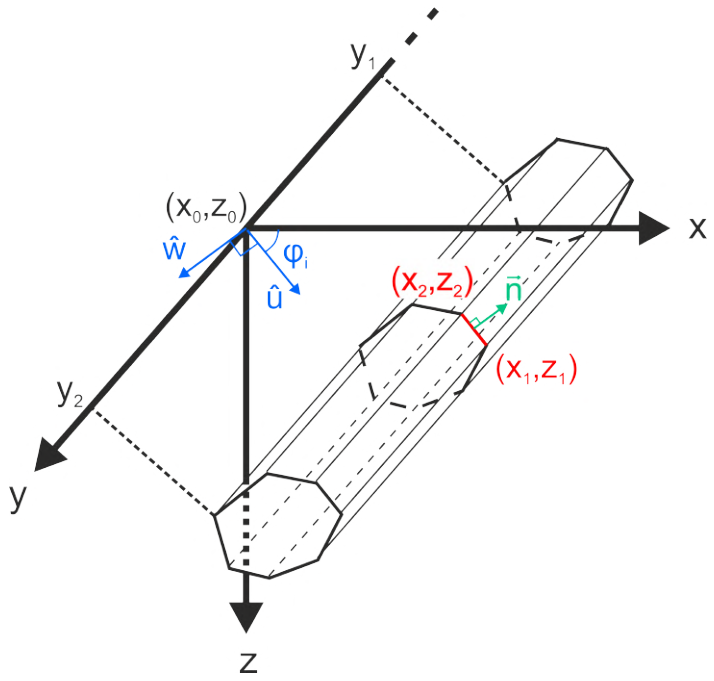

Figure 4.A.1 - Geometrical setup for 2.75D anomaly calculations.

distinguish two cases as a function of the elongation of the two semi-prisms with respect to the position of the profile (i.e., $y = 0$), namely i) symmetric bodies (2.5D), when $-y_1 = y_2$, and asymmetric bodies (2.75D), if $-y_1 \neq y_2$. Obviously, for $y_1 \to -\infty$ and $y_2 \to +\infty$ the numerical results of the 2.5D approach converge to those from the purely 2D case.

We present here a simplified version of the original formulations of Rasmussen and Pedersen (1979) for the 2.5/2.75D gravity case and that from Campbell (1983) for the corresponding magnetic case. To obtain the correct numerical solution, these formulae must be used in the case of counter-clockwise circuiting around the polygonal section, with respect to the positive-downward z direction. While testing our numerical implementation following the *NEWMAG* algorithm against the prismatic approach from Bhattacharyya (1964), we have found a sign error in Campbell (1983) which affects the magnetic calculations. The rearranged formulae and details about their derivations are discussed in the following.

4.A.1 Mathematical background

In this section we present the mathematical background and the common terms used for the gravity and magnetic derivations. Let us start with the definition of the coordinate system (u,y,w), rotated by a ϕ_i angle with respect to the Cartesian system (x,y,z), expressed in meters. This rotation is performed according to the orientation of the vector $\vec{n}$ representing the normal to the i-th polygonal face defining the 2.5/2.75D prism (Figure 4.A.1). By construction, the vector $\vec{n}$ always lies on the $x-z$ plane and is aligned to the $\vec{w}$ direction. For a polygon side represented by the coordinate pairs (x_1,y_1) and (x_2,y_2), taken in a counter-clockwise order with respect to a downward positive z axis, we can now define the new coordinates for the vertices as follow

$$u_1 = \cos(\phi)x_1 + \sin(\phi)z_1 \quad , \tag{4.20}$$

$$u_2 = \cos(\phi)x_2 + \sin(\phi)z_2 \quad , \tag{4.21}$$

$$w_{1,2} = w = -\sin(\phi)x_1 + \cos(\phi)z_1 \quad , \tag{4.22}$$

where the coordinates system rotation angle (ϕ) relative to that side is

$$\phi = \arctan\left(\frac{z_{21}}{x_{21}}\right) \quad , \tag{4.23}$$

and

$$x_{21} = x_2 - x_1, \quad z_{21} = z_2 - z_1. \tag{4.24}$$

In agreement with the original formulation, we define also two additional quantities

$$r_1 = \sqrt{u_1^2 + w^2} \text{ and } r_2 = \sqrt{u_2^2 + w^2}. \tag{4.25}$$

At this point, we can show the common mathematical expressions for gravity and the magnetic cases,

$$l_1 = \ln\left(\frac{r_1\,(\sqrt{r_2^2+y_1^2}-y_1)}{r_2\,(\sqrt{r_1^2+y_1^2}-y_1)}\right), \quad l_2 = \ln\left(\frac{r_1\,(\sqrt{r_2^2+y_2^2}+y_2)}{r_2\,(\sqrt{r_1^2+y_2^2}+y_2)}\right), \tag{4.26}$$

$$a_1 = \arctan\left(\frac{u_2\,y_1}{w\sqrt{r_2^2+y_1^2}}\right) - \arctan\left(\frac{u_1\,y_1}{w\sqrt{r_1^2+y_1^2}}\right) \quad , \tag{4.27}$$

$$a_2 = \arctan\left(\frac{u_2\,y_2}{w\sqrt{r_2^2+y_2^2}}\right) - \arctan\left(\frac{u_1\,y_2}{w\sqrt{r_1^2+y_2^2}}\right) \quad . \tag{4.28}$$

In order to perform right magnetic and gravity calculations, we need to add a check for the two terms a_1 and a_2 as follow

$$\begin{cases} a_1 = a_1 - 2\pi & \text{if } a_1 > \pi \\ a_1 = a_1 + 2\pi & \text{if } a_1 < -\pi \end{cases} , \tag{4.29}$$

$$\begin{cases} a_2 = a_2 - 2\pi & \text{if } a_2 > \pi \\ a_2 = a_2 + 2\pi & \text{if } a_2 < -\pi \end{cases} . \tag{4.30}$$

Other specific terms are related to the gravity and magnetic case respectively,

$$s_1 = \ln\left(\frac{u_2+\sqrt{r_2^2+y_1^2}}{u_1+\sqrt{r_1^2+y_1^2}}\right), \tag{4.31}$$

$$s_2 = \ln\left(\frac{u_2+\sqrt{r_2^2+y_2^2}}{u_1+\sqrt{r_1^2+y_2^2}}\right), \tag{4.32}$$

$$q_1 = \frac{1}{2}\ln\left(\frac{(\sqrt{r_2^2+y_1^2}-u_2)(\sqrt{r_1^2+y_1^2}+u_1)}{(\sqrt{r_2^2+y_1^2}+u_2)(\sqrt{r_1^2+y_1^2}-u_1)}\right), \tag{4.33}$$

$$q_2 = \frac{1}{2}\ln\left(\frac{(\sqrt{r_2^2+y_2^2}-u_2)(\sqrt{r_1^2+y_2^2}+u_1)}{(\sqrt{r_2^2+y_2^2}+u_2)(\sqrt{r_1^2+y_2^2}-u_1)}\right). \tag{4.34}$$

4.A.2 Gravity case

Rasmussen and Pedersen (1979) showed explicitly how to calculated the vertical attraction in the 2.5D case. However, as pointed out by the same authors, this formula results from the sum of the integral expression called I_1 (see Rasmussen and Pedersen, 1979) calculated twice using the value $y_{1,2}$ for the symmetrical body elongation choosen. Hence, the gravity calculation in the 2.75D case can be simply obtained by summing the contribution of the expression I_1 calculated for the y_1 and y_2 terms respectively. Then, this formulae can be now written as the fully explicit expression below, where we show the gravitational attraction resulting from a single edge of a polygon

$$g_z = -\rho\, G\left[\cos\phi\,(y_2\,s_2 - y_1\,s_1) + \left(\frac{x_1\,z_2 - z_1\,x_2}{\sqrt{x_{21}^2+z_{21}^2}}\right)(\cos\phi\,(a_2-a_1) - \sin\phi\,(l_1+l_2))\right], \tag{4.35}$$

where ρ is the uniform density (contrast) of the prism (expressed in $\frac{\mathrm{Kg}}{\mathrm{m}^3}$) and $G \approx 6.67 \cdot 10^{-11}\frac{\mathrm{Nm}^2}{\mathrm{Kg}^2}$ is the gravitational constant. Using directly eq. 4.35, the value of g_z is expressed in $\frac{m}{s^2}$, so to obtain the response in mGal it needs to be multiplied by a 10^5 factor. Finally,

the gravity response at each observation point for the entire prismatic body is achieved summing the contribution, calculated using the formula 4.35 above, relative to each side of the polygonal section taken in a counter-clockwise order. In case of more prisms, the overall gravity response is performed simply summing all the contributions related to each prism.

4.A.3 Magnetic case

In analogy with the gravity case, Rasmussen and Pedersen (1979) presented the analytic expressions required for the total field magnetic anomaly calculation only for the symmetric case. Unfortunately, for the 2.75D case, the equations for the three components of the magnetic field produced by the body (B_x, B_y, B_z) cannot be derived directly from the symmetric case as discussed for the gravity one. In fact, the term $(q_2 - q_1)$ indicated in Campbell (1983) as ΔI_4 differs from zero in the asymmetric case, complicating the analytical expressions for B_x, B_y and B_z. For this reason, the formulae need to be derived summing certain integral expressions described in Rasmussen and Pedersen (1979) for both the two semi-prisms, merging the individual results to achieve the magnetic response due to the entire 2.75D body. In addition, the same term $(q_2 - q_1)$ shows an error sign affecting the magnetic anomaly calculation, and need to be substituted by its opposite $(q_1 - q_2)$. Below we show the rectified explicit analytic formulae for B_x, B_y and B_z, again, for a single edge of a polygonal body,

$$\begin{aligned} B_x &= -\sin\phi \Big[(l_1 + l_2)(\cos\phi J_x + \sin\phi J_z) \\ &- (a_2 - a_1)(\cos\phi J_z - \sin\phi J_x) - J_y (q_1 - q_2) \Big] \quad , \qquad (4.36) \\ B_y &= J_y (a_2 - a_1) - (q_1 - q_2)(\cos\phi J_z - \sin\phi J_x) \quad , \qquad (4.37) \\ B_z &= \cos\phi \Big[(l_1 + l_2)(\cos\phi J_x + \sin\phi J_z) \\ &- (a_2 - a_1)(\cos\phi J_z - \sin\phi J_x) - J_y (q_1 - q_2) \Big] \quad , \qquad (4.38) \end{aligned}$$

where J_x , J_y and J_z represent the three components of the magnetization vector **J** obtained as vector sum of induced and remnant contributions (unit in A/m). The three components of the magnetic field produced by the body need to be projected onto the Earth's magnetic field vector, characterized by inclination I_{ind} and declination D_{ind}, to achieve the total field magnetic anomaly (expressed in nT) as follow

$$\Delta T = \frac{1}{4\pi}\Big[B_x \cos(I_{\text{ind}})\cos(C - D_{\text{ind}}) + B_y \cos(I_{\text{ind}})\sin(I_{\text{ind}}) + B_z \sin(I_{\text{ind}})\Big] \quad , \qquad (4.39)$$

where C represents the angle measured from the geographic North to the profile direction, taken clockwise. As for the gravity case, the contribution from each side of the polygon must be added up to compute the response at the observation point and, in case of multiple polygons, their contribution must also be added up.

Appendix 4.B Geometrical issues: when updates using the gradient produce physically impossible models

The update of the position of the vertices of the polygonal bodies is performed during the leap-frog iterations and depend on the gradient of potential and kinetic energy. Such updates may produce geometrical configurations which are physically impossible, either because polygons self-intersect or because polygons intersect each other, which cannot happen from a geological point of view. The crude algorithm is unaware of these physical constraints, therefore, from time to time, during the HMC iterations such situations may arise. Unfortunately, it is not possible to find a simple closed-form mathematical solution to this problem, so we resort to perform a set of checks after each update of the model parameters

(position) and, in case the geometry results invalid, we stop the trajectory within NUTS and avoid using the last model as a candidate for an update.

Appendix 4.C Description of the software

There are a total of three packages providing the framework to perform HMC joint inversion of magnetic and gravity data for 2D polygonal bodies: (1) GeoPolygons, which handles the polygons in terms of vertices and bodies and provides a set of functions to control the meaningfulness of the geometrical structure, (2) MagGrav2Dpoly, which provides the routines for the forward and gradient magnetic and gravity calculations, and (3) HMCsampler.jl, which contains the functions to perform the actual HMC sampling for arbitrary problems. The Julia code for these packages can be found at https://gitlab.com/JuliaGeoph.

Part III

3D prism-based parameterization approach

Chapter 5

The sub-ice structure of Mt. Melbourne Volcanic Field (Antarctica) uncovered by High-Resolution Aeromagnetic data

Abstract

The Mt. Melbourne Volcanic Field (MVF) is a quiescent volcanic complex located in Northern Victoria Land, Antarctica, mostly covered by ice. Its inner structure and evolution are still debated, due to the paucity of outcrops and the lack of detailed multi-disciplinary investigations. Here we present a novel high-resolution aeromagnetic dataset, revealing strong long-wavelength negative anomalies superimposed by short-wavelength positive ones forming characteristic radial patterns. Automatic lineament detection, through the Hough transform technique applied to the tilt derivative of our magnetic dataset, shows prevailing N-S-, NW-SE- and NNE-SSW-trending structural features, which combined with the few structural field observations contribute to define the deformation pattern. Pre-existing and novel magnetic property measurements, coupled with available geochronological data, are used to constrain a two-step 3D magnetic inversion. A layer-structured Parker-Oldenburg's inversion was utilized to model the deep and long-wavelength component of the magnetic field, whereas a linear inversion based on a set of shallower prisms was used to model the short-wavelength components. The final 3D model shows widespread reversely-polarized volcanics, which are locally intruded and superimposed by swarms of normally-polarized dikes and lava flows. These results backdate the onset of spread volcanic activity at the Matuyama magnetic epoch, i.e., between 2.58 and 0.78 Ma.

5.1 Introduction

Antarctica represents the last frontier in Earth geological exploration, where the thick ice sheet mostly prevents direct observation of the subglacial geology and tectonics affecting the continent. In this context, half a century of aero-magnetic investigations has offered a unique way to image structures, lithologies and volcanic features buried beneath the ice sheet, helping scientists to study the geological framework of the entire continent (e.g., Ebbing et al., 2021; Ferraccioli et al., 2009a,b, 2005; Golynsky et al., 2018; Goodge and Finn, 2010; Jordan et al., 2022; Kim et al., 2022). Only few High-Resolution Aero-Magnetic datasets (HRAM) are available in Antarctica (e.g., Armadillo et al., 2012; Damaske et al., 2014; Ferraccioli et al., 2005; Ghidella et al., 2013; Jordan et al., 2014; Mieth et al., 2014; Ruppel et al., 2017; Wilson et al., 2007), which allowed the investigation of specific areas of geological interest to be carried out in greater detail. A HRAM survey in a volcanic environment, for example, is fundamental not only to reveal the volcanic edifice but also to map the magmatic setting, including alteration related to hydrothermal activity and the pattern of volcano-tectonic deformations, with important implications for contributing to the reconstruction of the volcanic history (e.g., Bouligand et al., 2014; Finn et al., 2022, 2007; Finn and Morgan, 2002).

A site of particular interest where a novel HRAM is available is the sub-ice Mt. Melbourne Volcanic Field (MVF), a quiescent volcanic complex located in Northern Victoria Land whose most recent volcanic activity is estimated between 1862 and 1922 (Lyon, 1986). This field, placed along the Transantarctic Mountains rift shoulder at the boundary with the western side of the West Antarctic Rift System (WARS) (Figure 5.1a), is considered having the potential for future large-scale explosive eruptions (Giordano et al., 2012). Its off-rift position, common to many other rift-related volcanic contexts around the world (e.g., Hamlyn et al., 2014; Sigmundsson et al., 2010; Yang et al., 2018), is a matter of scientific debate. The mechanisms triggering off-rift volcanism have recently been clarified by Maccaferri et al. (2014), who

suggest the location of volcanism in rift complex is determined by a competition between gravitational unloading and tectonic stretching. Hence, the study of the MVF as well as other off-rift active volcanoes located along the same rift shoulder like Mt. Erebus and Mt. Rittmann could be of significant scientific interest to better comprehend the complex stress field generated by the extension of the WARS and the flexural uplift of the TAM (Brenn et al., 2017; Huerta and Harry, 2007; Paxman et al., 2019; Stern and ten Brink, 1989; ten Brink et al., 1997). However, despite a variety of geological, geochemical and geophysical investigations performed to improve the knowledge of the MVF and assess its hazard (Adamson and Cavaney, 1967; Armienti et al., 1991, 1988; Armstrong, 1978; Beccaluva et al., 1991a,b; Bonaccorso et al., 1995, 1996; Cremisini et al., 1991; Del Carlo et al., 2022; Ferraccioli et al., 2000; Gambino et al., 2016, 2021; GANOVEX Team, 1987; Giordano et al., 2012; Gubellini and Postpischl, 1991; Hornig et al., 1991; Keys et al., 1983; Lanza et al., 1991; Lanzafame and Villari, 1991; Lee et al., 2015; Lyon, 1986; Lyon and Giggenbach, 1974; Manzoni and Miletto, 1988; Müller et al., 1991; Nathan and Schulte, 1967, 1968; Pasquale et al., 2009; Vignaroli et al., 2015; Wörner and Viereck, 1987, 1989; Wörner et al., 1989), there is no clear consensus on its geological structure and temporal evolution. The main reason lies on the ice that almost completely cover the volcano, limiting the data collection to small, scattered areas of geological outcrops which prevent a detailed characterization of the volcanic area.

The aim of this chapter is the geophysical characterization of the MVF. In section 5.2 we give an overview of the geological and structural setting of the volcanic complex, whereas in section 5.3 we present the analysis and enhancement of the novel HRAM dataset, interpreted along with geochronological and both inedited and available magnetic susceptibility and remanence data collected by authors over the MVF during different Italian Antarctic expeditions of the PNRA (Italian National Antarctic Research Program). In section 5.4, magnetic patterns of subglacial volcanic deposits are imaged with unprecedented detail by means of two complementary inversion methods, thanks to which in section 5.5 we improve

noteworthy the general knowledge of the volcanic history of the MVF, proposing a new temporal evolution for it differing from all those presented so far.

5.2 Geological framework

The MVF is part of the Mt. Melbourne Volcanic Province (Kyle, 1990; Kyle and Cole, 1974), that extends northward to include the older volcanic centers of Mt. Overlord, Mt. Rittmann, the Pleiades and Malta Plateau (Armadillo et al., 2007; Kyle, 1990; Kyle and Cole, 1974; Smellie and Rocchi, 2021, see Figure 5.1a). This province belongs to the McMurdo Volcanic Group (Harrington, 1958; Kyle, 1990; Kyle and Cole, 1974), one of the most extensive alkali volcanic provinces in the world, also including the Hallett and the Erebus Volcanic Provinces respectively northward and southward. The oldest volcanic activity associated with the McMurdo Volcanic Group has been identified in the Meander Intrusives, a 48–18 Ma old set of limited and scattered intrusions exposed on the steep side of the TAM overlooking the Ross Sea and cropping out in the northernmost sector of the MVF (Armienti et al., 1988; GANOVEX Team, 1987; Müller et al., 1991; Pertusati et al., 2012; Tonarini et al., 1997, see Figure 5.1b).

At a regional scale, the widespread alkaline magmatism comprising the McMurdo Volcanic Group, resting on the crystalline basement of the Ross Orogen Wilson Terrane (Carmignani et al., 1988), is inferred to be related to the opening of the WARS in the Eocene time and its subsequent extension which is still in progress (Lanzafame and Villari, 1991; Rocchi et al., 2002; Roland and Tessensohn, 1987; Salvini et al., 1997). Several authors suggested the regional rifting of the Ross Sea and the uplift of the TAM have affected, at a local scale, the tectonic processes and magmatism of the MVF. Lanzafame and Villari (1991) proposed the localization of the volcanic activity forming MVF could be related to two main intersecting sets of extensional faults striking NW-SE and NNE-SSW, whereas Vignaroli et al. (2015) indicated tree main sets of high-angle fault systems trending NW-SW, NE-SW and N-S

(Figure 5.1b). This tectonic setting is inferred the consequence of a deformation regime transition (in space and time) from pure transcurrent to extensional in an overall context of oblique rifting scenario affecting the entire Northern Victoria Land (Vignaroli et al., 2015).

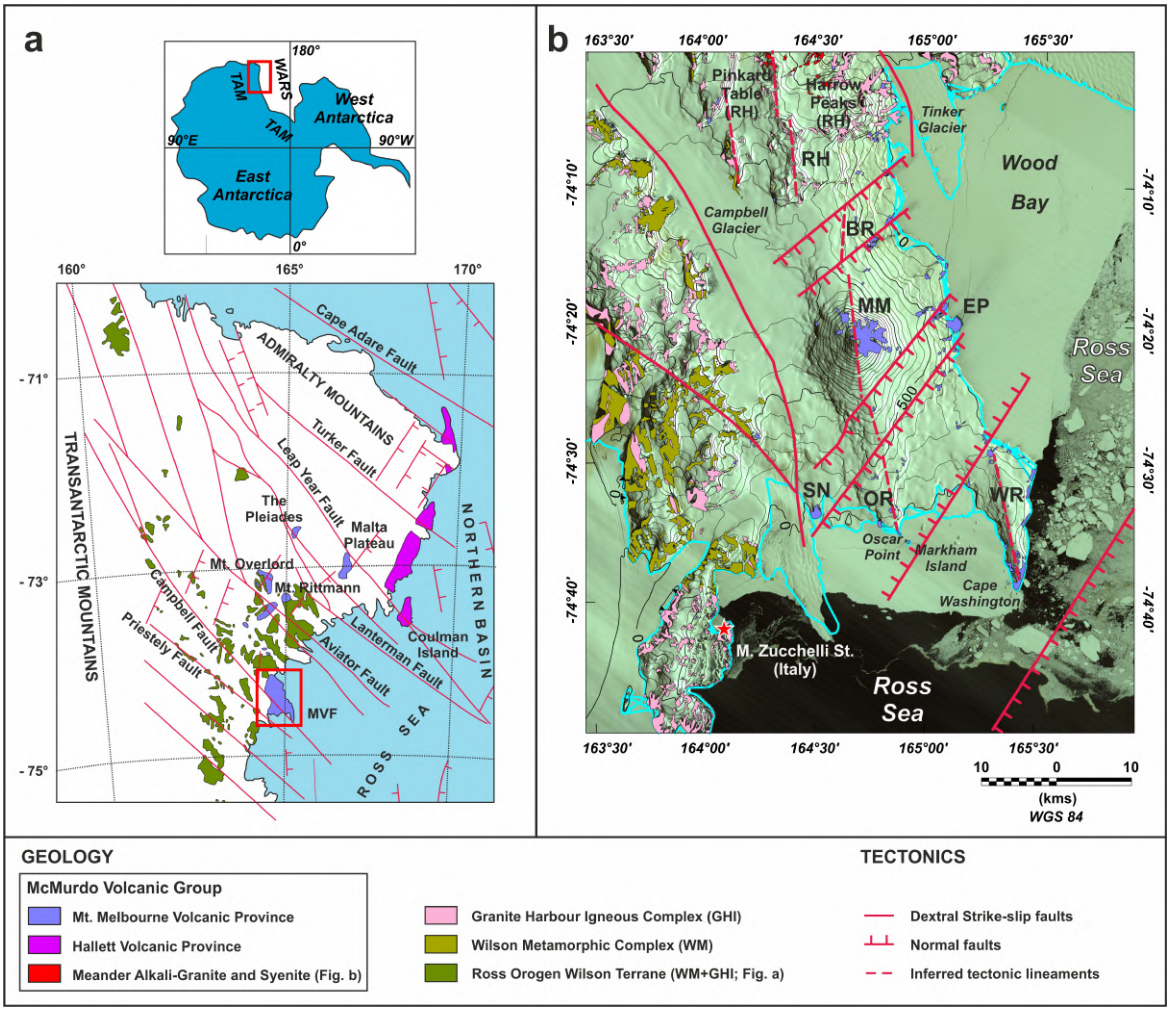

Figure 5.1 - (a) Regional map of the geology and tectonics of Northern Victoria Land (after GANOVEX Team, 1987; Salvini et al., 1997; Storti et al., 2008). (b) Landsat image of the MVF, the study area, with superimposed the recognized geological outcrops and tectonic features affecting the volcanic complex. Contour line intervals every 100 meters. Geological and structural data are digitized from Pertusati et al. (2012) and Giordano et al. (2012), Vignaroli et al. (2015) respectively, whereas Landsat image is from Bindschadler et al. (2008). Sub-suites are defined according to Wörner and Viereck (1989) and Pasquale et al. (2009): Washington Ridge (WR), Oscar Ridge (OR), Shield Nunatak (SN) at south, Edmonson Point (EP) at East, Baker Rocks (BR), Random Hills (RH) at north and the Mt. Melbourne volcano (MM).

The MVF is composed of up to 60 scattered subglacial and subaerial volcanic centers surrounding the 2700m-high Mt. Melbourne stratovolcano, subdivided in seven main volcanic sub-suites on the base of their morphology, eruptive styles and petrography (Wörner and Viereck, 1989, Figure 5.1b). Wörner and Viereck (1989) proposed the first phase of volcanic activity started about 2.7 Ma at WR and then focused on the MM during the late Pleistocene-Holocene (geochronological data from Armstrong (1978) and Kreuzer (1988)-unpubl. report quoted in Wörner and Viereck (1989)). On the other hand, Giordano et al. (2012) proposed new ages for the MVF, postponing the initial development of the MM and its closest peripheral centers to after 450 ka, in apparent disagreement with both some geochronological data from Lee et al. (2015) and from previous studies (e.g., Armienti and Baroni, 1999; Armienti et al., 1991; Armstrong, 1978; Müller et al., 1991). A comprehensive review of all age estimates published in literature is given by Smellie and Rocchi (2021).

However, it is important to outline that most of the existent geochronological data are not always supported by precise sampling localities or sample descriptions. In addition, age estimates refer to scattered sites of subaerial recent lavas, so they do not reflect the likely older completely hidden inner part of the MVF. Therefore, part of the story and architecture of the Mt. Melbourne could be still partially unknown and hidden under the ice.

5.3 Geophysical data

In the first part of this section, we present the technical information about the acquisition and processing of the HRAM data. An innovative technique for automatic magnetic lineament detection gave detailed information about the structural features affecting the MVF. In the second part we present new magnetic susceptibility measurements (listed in Appendix 5.A, Table 5.A.1), integrated with pre-existing magnetic properties data. At the end, we combine all available information, developing a hypothesis about the internal structure of the volcanic complex to be tested through magnetic inversion presented in section 5.4.

5.3.1 HRAM Survey

5.3.1.1 Data Acquisition & Processing

The HRAM dataset was acquired over a survey area of 2640 km^2 along 128 lines flown using a Squirrel-B2 helicopter. Line spacing was 500 m and tie intervals 2500 m for a total of 6490 km lines length (Figure 5.2a). The survey was flown in a draped mode with nominal constant clearance of 450 m from the topographic surface monitored using at the same time a radar, a laser (ADM Geophysical Altimeter OPTEC) and a barometric (Rosemount) altimeter. Magnetic data were collected at sampling frequency of 10 Hz using an optically pumped Scintrex MAC III Cesium magnetometer with a resolution of 0.01 nT, installed in a bird configuration. Three geomagnetic base stations, acquiring data at a 30 second sampling rate, were set up at Baker Rocks (BR), Cape Washington and Pinkard Table in order to monitor the Geomagnetic activity prior and during the survey (Figure 5.2a). A GNSS differential navigation system (Magnavox 4200 + GPS Trimble ProXRS) was used to allow for differential corrections to be applied to the positioning data.

The processing of raw magnetic data has been carried out according to classical aero-geophysical procedures (e.g., Luyendyk, 1997). In detail, initial raw data check was performed in the field and any plausible artifact or spike was removed. Lag correction was applied to correct for the relative positioning between the helicopter and the magnetic sensor (about 15 m) during flights and diurnal variations of the Geomagnetic field were subtracted using base stations magnetic data recordings. The positional data were recovered using carrier-phase, continuous, kinematic GPS processing techniques (Mader, 1992). The geomagnetic reference field for all the data points of the survey, calculated using the proper DGRF coefficients, was then subtracted to obtain Total-field Magnetic intensity Anomaly (TMA) data. Residual diurnal magnetic variations errors in the data were removed using leveling procedures, whereas residual flight line-related corrugation noise was minimized by means of micro-levelling techniques (Ferraccioli et al., 1998). TMA data have not been

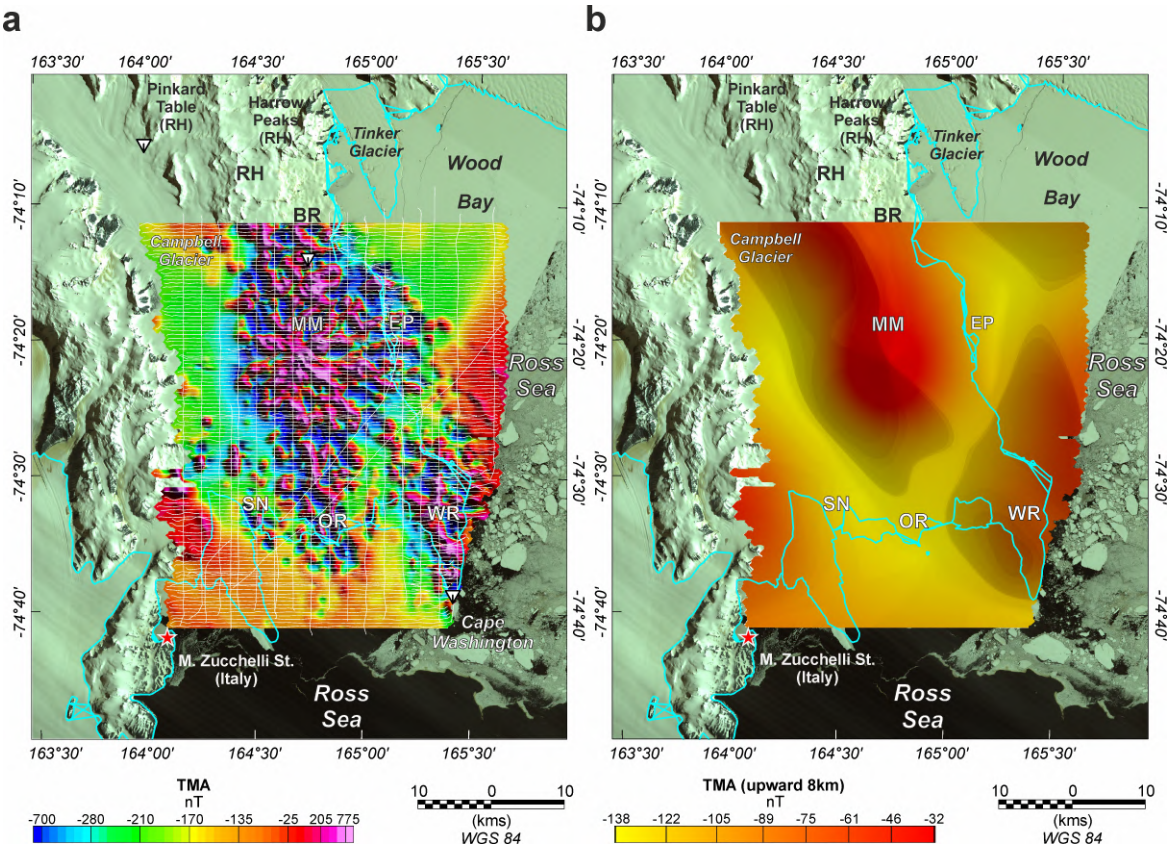

Figure 5.2 - (a) Landsat image with superimposed new High-resolution Total-field Magnetic intensity Anomaly (TMA) data covering the entire MVF. The three inverted white triangles represent the locations of the geomagnetic stations installed during the aeromagnetic survey to monitor the geomagnetic activity. (b) TMA data upward-continued at 8 km height. This low-pass filtered data shows clearly along the entire MVF a pronounced negative anomaly. For abbreviations see caption of Figure 5.1.

reduced to pole, since this mathematical operation assumes both no draped data and induced magnetization as the only source causing the TMA, untrue in volcanic contexts. However, being the MVF near to the South Pole, magnetic anomalies in our TMA dataset can be considered, in a sensible approximation, as reduced to the pole (i.e., should not present dipolar shapes). TMA gridded data are shown in Figure 5.2a.

5.3.1.2 Digital Enhancement & Automatic Lineament Detection

Digital Enhancement techniques are usually employed in potential field geophysics to recognize geological and structural features such as faults, lithological contacts and other structures causing a sharp variation of a physical property (in our case magnetization). Hence, in a continent like Antarctica where rock outcrops and main tectonic structures are almost completely covered by the ice sheet, digital enhancement techniques play a crucial role in the reconstruction of the expected geological and structural framework of complex areas like the MVF. For this reason, we have (i) upward-continued our TMA data to understand the nature of the sources of the magnetic anomalies in the dataset and (ii) implemented an image analysis algorithm based on the Hough transform (Duda and Hart, 1972; Hart, 2009; O'Gorman and Clowes, 1976) to be applied to the tilt derivative (TDR, Fairhead, 2016; Miller and Singh, 1994; Verduzco et al., 2004) of our TMA data, to unveil with unprecedented detail the main structural features affecting the subglacial MVF.

Regarding the first target, the TMA dataset was upward-continued to 8 km height in order to better isolate and describe the long wavelength magnetic signatures in the data, reflecting the main structures expected in the deeper part of the volcanic complex. The upward-continued data gridded are shown in Figure 5.2b. At a first glance, the original TMA grid reveals two similar magnetic signatures beneath MM and WR, characterized by wide NW-SE to N-S trending long wavelength pervasive negative anomalies superimposed by apparent short-wavelength positive ones forming radial patterns. Looking at the upward-continued data, the radial pattern completely disappears together with all positive anomalies, suggesting the negative signatures dominate on the TMA dataset.

For the second purpose, we calculated the TDR of our gridded TMA, being this type of data enhancement especially suitable to detect local maxima of TMA due to geological sources, such as fault-related dikes, cones alignments, lava flows, etc. Differently from other digital enhancement techniques, the TDR is independent from the magnetization

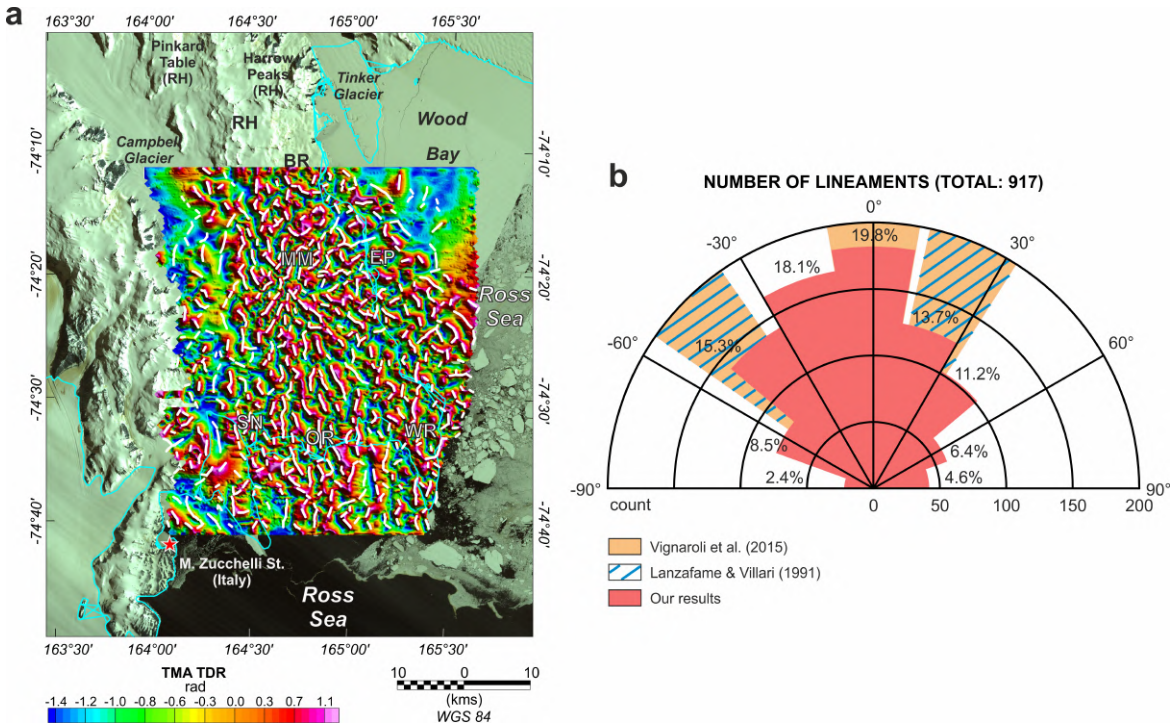

Figure 5.3 - (a) Lineaments detected by the proposed algorithm for automatic lineament detection through the Hough Transform (total amount of lineaments: 917), superimposed on the TDR of our TMA dataset. For abbreviations see caption of Figure 5.1. (b) Rose diagram of the percentual frequencies of the detected magnetic lineaments trends. In the background, trends resulting from field surveys of Lanzafame and Villari (1991) and Vignaroli et al. (2015). The N-S trend is the most frequent in the entire MVF.

direction (Fairhead, 2016), making it particularly useful in volcanic contexts where usually the remanent magnetization dominates upon the induced one. The TDR map is shown in Figure 5.3a. In order to detect the magnetic lineaments, we have first applied the phase congruency operator (Kovesi, 1999, 2003) to the TDR, tracing the local positive picks. Then, we have transformed the phase into a black and white image and applied a skeleton algorithm (Lee et al., 1994) to reduce the binary image to 1-pixel wide curved lines without changing the essential structure. At the end, we have applied the Hough Transform to automatically detect and statistically analyze the lineaments in the image. The minimum length detection threshold was placed equal to the magnetic data spacing (500 m). All the structures detected are shown in Figure 5.3a. To better visualize the structural information

achieved, a rose diagram representing the frequency of all the inferred features with respect to their angular orientation is shown in Figure 5.3b and compared with the trends resulting from Lanzafame and Villari (1991) and Vignaroli et al. (2015) (Figure 5.1b).

Our results, discussed more in detail in the next sub-section 5.3.3, reveal three main sets of structural features trending N-S, NW-SE and NNE-SSW; the E-W trending set is likely devoid of geological significance, being mainly the result of residual leveling errors not removed during the TMA data processing. These results are in good agreement with published data of tectonic structures measured directly in the field. Such measurements were obtained from data collected from a few scattered outcrops, while our results have a broader coverage being derived from the HRAM data. Moreover, the method proposed in this study can also detect minor trends (see the rose diagram in Figure 5.3b) and so it proves to be an excellent support for structural studies in remote areas.

5.3.2 Rock magnetism

Magnetic properties on rock samples represent fundamental constraints to magnetic inverse modeling, particularly in volcanic environments. The only susceptibility and remanent magnetization measurements on rock samples collected in the MVF were carried out during the 1985/86 and 2002/2003 Italian Antarctic expeditions to Victoria Land (Bozzo et al., 1987; Lanza et al., 1991; Manzoni and Miletto, 1988; Pasquale et al., 2009). In addition, other unpublished magnetic susceptibility data collected in the field during the 2002/2003 Italian Antarctic expedition are presented in this work. These data have been measured by means of a portable kappa-meter Geofyzika KT5 with a resolution of 10^{-5} SI units, collecting for each site up to 12 measurements to be able to make a statistical evaluation of the quality of the data. Locations and magnetic susceptibility data from the new samples analyzed are shown in Figure 5.4a and listed in Table 5.A.1 in Appendix 5.A. In the same table, are listed also all previous magnetic property data available for the MVF.

The large variability in magnetic susceptibility shown by rock samples, even belonging to the same outcrops (Table 5.A.1), reflects the petrographic and textural heterogeneity of rocks observed in this volcanic area (Wörner et al., 1989) and, consequently, the variable content and type of ferromagnetic minerals in magmatic products (Clark, 1997; Hinze et al., 2013). A similar argument applies to the magnetic remanence, reaching in some places very high values ($> 20\,\mathrm{A/m}$, see Table 5.A.1). Furthermore, the widespread prevalence of very high Koenigsberger ratios (i.e., the ratio of Remanent magnetization and Induced magnetization modules, see section 1.3.2) suggests the magnetic susceptibility of rocks could be neglected during modeling of TMA data (Manzoni and Miletto, 1988).

For what concerns the inclination of magnetic remanence, assuming no continental-scale tectonic displacement/rotation occurred in this part of Antarctica during the Quaternary period, it is representative of the polarity of the Earth magnetic field recorded by rocks after their cooling. In detail, samples with both normal (i.e., negative remanence inclination) and reverse (i.e., positive remanence inclination) polarization were found in MVF, the reverse ones located on OR area (also southward to Markham Island), north of WR and on the south-eastern slope of the MM (Figure 5.4b). Since the times of the magnetic polarity reversal are well known, these remanence data are fundamental to (i) document certainly that volcanic activity started before the current Brunhes magnetic epoch (> 0.78 Ma, chron C1n following the notation proposed by Cande and Kent (1992, 1995)) and (ii) correctly assess the anomaly sources in our HRAM dataset. Hence, coupling available geochronological data from rock samples collected around the field we can finally have a look at the inner buried MVF and obtain important hints to reconstructing the timing of the volcanic activity, as we discuss afterwards.

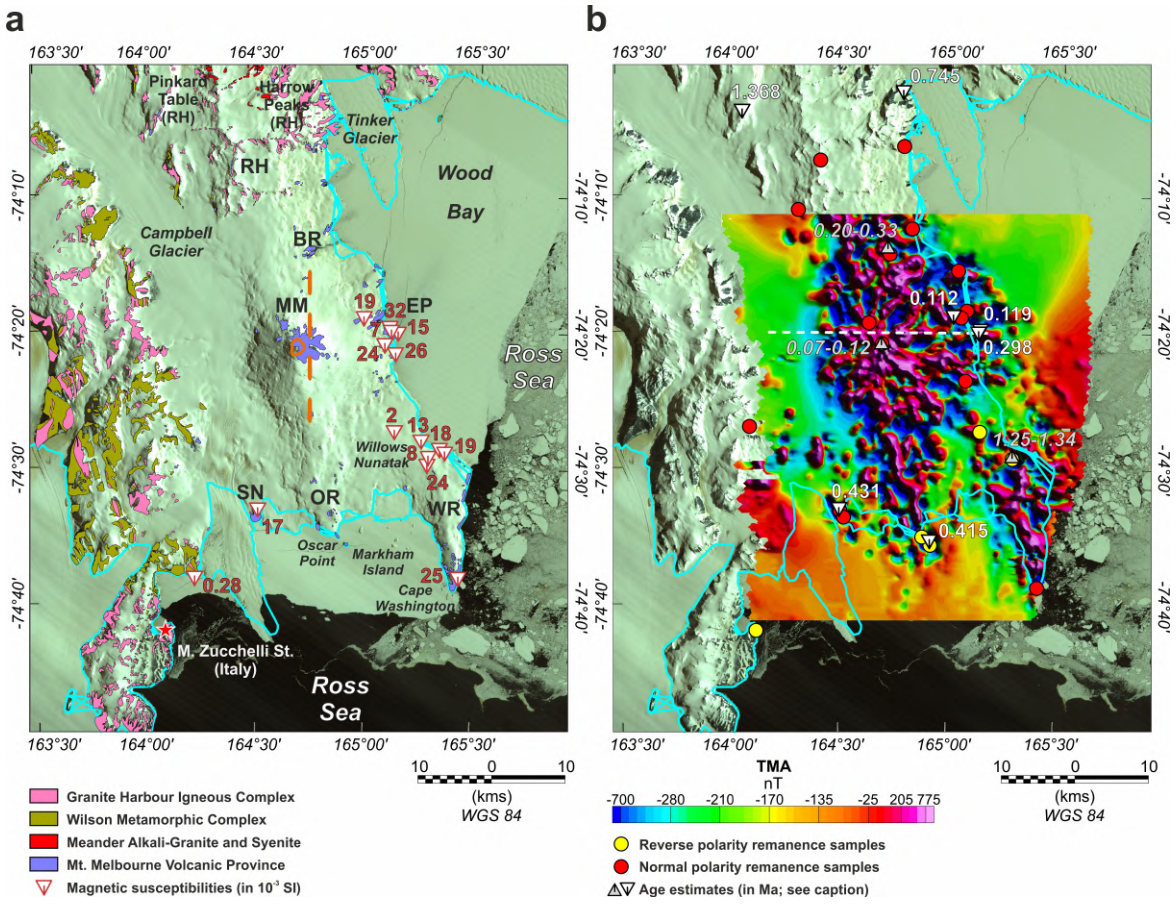

Figure 5.4 - (a) Location and values of the new magnetic susceptibility measures (red numbers and inverted triangles) collected around the MVF (listed in Table 5.A.1, Appendix 5.A) and geology of the study area on Landsat image. Notice the very low value in magnetic susceptibility shown by the only sample collected on the Granite Harbour Igneous Complex compared to all the other ones. In addition, the caldera area affected by hydrothermal activity and the trace of an altered cliff discussed in Giordano et al. (2012) are shown in orange. See caption of Figure 5.1 for abbreviations. (b) Locations and values of the most recent age estimates together with magnetic remanence polarity data from literature (base map is Landsat image of the MVF with superimposed the TMA grid). Inverted white triangles and white numbers are the age estimates from Giordano et al. (2012), light grey triangles and numbers in italics are ages from Lee et al. (2015). Other available ages (discussed throughout this manuscript) are not shown due to either missing or imprecise location of the samples (all ages are listed in Table 5.B.1). Magnetic remanence sample data are from Manzoni and Miletto (1988) and Lanza et al. (1991). Moreover, in dashed white is shown the E-W profile along which has been achieved the 2D forward magnetic model illustrated in Figure 5.D.1.

5.3.3 HRAM and rock magnetism interpretation combined with available geochronological data

Our analysis and enhancement of TMA data supplied new detailed information about (i) the sub-ice structural lineaments and (ii) the buried volcanic framework characterizing the MVF.

Regarding point (i), three main subglacial sets of features trending N-S, NW-SE and NNE-SSW have been detected through automatic lineament detection, the first one more pervasively distributed and matching the topographic orientation of both the WR and the MM (Figure 5.3). Our observations can be compared with structural data available in literature and derived from either direct field investigations or aerial image analysis (e.g., Giordano et al., 2012; Lanzafame and Villari, 1991; Vignaroli et al., 2015, Figures 5.1b-5.3). Our lineaments fit the orientation of the main tectonic structures and fault-related dikes, subaerial alignments of volcanic scoria cones and lava flows described for the MVF area, striking approximately N-S at OR and WR and NE-SW at EP (Wörner and Viereck, 1989). The N-S and NW-SE trending lineaments likely can be associated with a strike-slip deformation pattern (e.g., Läufer et al., 2011; Salvini et al., 1997; Storti et al., 2008) and seem to link the MM area to RH northward and OR southward, suggesting a common structural control on the volcanic activity generating these sub-suites. The NNE-SSW trend appears to connect MM to the EP sub-suites, inferred the result of a Quaternary change in the deformation regime that involved the activation of major extensional fault zones along the modern coastline (Vignaroli et al., 2015). Moreover, both MM and WR lineaments follow the already described radial pattern in the TMA grid. Such a pattern could be associated with both (i) radial lava flow events steered by the topographic gradient and (ii) swarms of radial dikes of volcano-tectonic origin. Evidence of radial lava flows is suggested by field observations on the crater area of MM (Wörner and Viereck, 1989), whereas radial swarms of dikes could be emplaced in the fissures of the volcanic edifices generated by a local stress field change related to the propagation of magma inside the volcano (e.g., Geshi, 2008, and references therein).

As regards the buried volcanic framework characterizing the MVF (point ii), two similar magnetic signatures beneath MM and WR have been recognized, characterized by strong and distinct positive and negative anomalies.

The positive anomalies, commonly showing a radial pattern on MM and WR as just indicated by results from automatic lineament detection (Figures 5.2a-5.3a), are related to short-wavelength signal components due to shallower sources characterized by different magnetic properties with respect to surrounding volcanics, as suggested by upward-continued TMA data (Figure 5.2b). These magnetic sources may be associated with volcanic activity, in the form of swarms of feeder dikes and related lava flows, occurred during periods of magnetic normal polarity. These could be either the current Brunhes epoch (C1n < 0.78 Ma) or the Jaramillo (C1r.1n) and Olduvai (C2n) chrons (1.07 – 0.99 Ma and 1.95 – 1.77 Ma respectively), short intervals in the reverse magnetic polarity Matuyama epoch (2.58 – 0.78 Ma). The Brunhes hypothesis is in better agreement with the consistent observation of geochronological data younger than 0.50 Ma and normal polarity from most of the rocks of the MM slopes and the peripheral southwestern SN and eastern EP centers, the last considered one of the youngest volcanic sub-suites of the MVF (see Figure 5.4b, Armienti et al., 1991; Armstrong, 1978; Giordano et al., 2012; Kreuzer, 1988; Lee et al., 2015; Müller et al., 1991). In the summit of MM, positive magnetic anomalies, field evidence and historical observations on ice thickness indicate volcanic activity occurred until recent times (Adamson and Cavaney, 1967; Del Carlo et al., 2022; Keys et al., 1983; Lee et al., 2019; Lyon, 1986; Nathan and Schulte, 1968); the latter eruptions deposited tephra layers thick about 5 m in the eastern crater rim (Wörner and Viereck, 1989). For a comprehensive overview of all age estimates and magnetic remanence inclination data available for each volcanic sub-suite, refer to Table 5.B.1.

As far as the other peripheral centers to the north, at BR (Figure 5.4a) ages are available for both the coastal and inland sectors, showing a younging of rocks moving inland. Ages

from the inland area are 0.72±0.10 and 0.19 to 0.33 Ma (Armstrong, 1978; Lee et al., 2015), whereas those in the coast to the north are 2.59±0.11 and 2.96±0.20 Ma (Armienti et al., 1991). All these age estimates are placed in periods of normal polarity, the oldest in the Gauss epoch and the youngest in the current Brunhes, in agreement with remanence negative inclinations from rocks samples collected in this area.

For the northernmost RH (Figure 5.4a), Armienti et al. (1991) reported age estimates of about 12.50 Ma, much older than all the others available for the MVF, whereas Giordano et al. (2012) indicated younger ages of 0.745±0.066 and 1.368±0.090 Ma (Figure 5.4b). If we take into account only the more recent ages proposed by Giordano et al. (2012), owing to the limitations of the K-Ar method used by Armienti et al. (1991) for dating, the formation of the RH volcanic centers likely started in the Matuyama epoch and continued in the current Brunhes epoch, as suggested even by normally-polarized remanence samples from that area.

Regarding the southeastern WR area (Figure 5.4a), age ranging from 2.70 to 1.67 Ma (Kreuzer, 1988) coupled with normally-polarized remanence samples (see Figure 5.4b) suggest the positive radial pattern in this area could be the response of lava flows deposited either during the Olduvai chron or, as pointed out by Lanza et al. (1991), at the end of the Gauss epoch, being the oldest age estimates placed before the Gauss – Matuyama polarity reversal (2.58 Ma). As a support for both the hypotheses, the remanence samples, located where positive magnetic anomalies occur, are surrounded by negative ones, most likely related to magmatic activity occurred in the Matuyama epoch; in fact, the preceding reverse polarity Gilbert epoch would be too older (5.89 – 3.58 Ma) with respect to the ages available on WR (Armstrong, 1978; Kreuzer, 1988).

The negative magnetic signatures over both the MM and WR, dominating the enhanced TMA data (Figure 5.2b), could be related to a combination of different phenomena, that are a) strong demagnetization owing to intensive hydrothermal alteration, b) topographic effects,

c) lava flows with highly variable content in magnetic minerals (i.e., strong contrasts in magnetic susceptibility/remanence) and d) thick volcanic strata with reverse magnetization.

Regarding the demagnetization hypothesis (point a), various authors described the presence of weak and scarce geothermal surface manifestations around MM such as fumarolic activity, steaming grounds and ice hummocks focused on the north rim and slope of two craters in the southern side of the caldera (Cremisini et al., 1991; Gambino et al., 2021; Lyon and Giggenbach, 1974; Nathan and Schulte, 1967, Figure 5.4a). In addition, hydrothermal alteration is pointed out by Giordano et al. (2012) along a sub-vertical cliff about $50-100$ m high running N-S along the entire eastern flank of MM (Figure 5.4a). The effect of a hydrothermal circulation in a volcanic environment is the loss of magnetization from magnetic minerals contained abundantly on rocks, resulting in a smooth attenuation of magnetic anomalies following the location of geothermal surface manifestations (e.g., Bouligand et al., 2014; Finn et al., 2022, 2007; Finn and Morgan, 2002). This phenomenon has not been observed in the MVF, suggesting the absence of a spread and consistent deep hydrothermal circulation (Figure 5.4b). As a validation of this evidence, Lyon and Giggenbach (1974), Cremisini et al. (1991) and Gambino et al. (2021) suggested that the hydrothermal manifestations of the MVF, showing very low pressure and intermittent activity in some locations, could derive from melted buried ice. Hence, hydrothermal manifestations and alterations would be the result of localized and superficial hydrothermal activity not affecting in depth the magnetic properties of rocks in the MM. In light of these considerations, the first hypothesis seems less probable.

As far as hypotheses b), 3D forward modeling has been performed to test the topographic effects by means of the Parker's algorithm (Parker, 1973), as implemented in the software package GMSYS-3D (Geosoft 8.5 Standard Edition, https://www.seequent.com/products-solutions/geosoft-oasis-montaj/). The model geometry is 36.5 x 53.1 km wide in the East and North direction respectively, designed to include the main volcanic sub-suites only. The

approach chosen requires a model geometry defined by surfaces, infinitely elongated outside the model, which separate layers with fixed magnetic properties. Since our aim is to calculate the magnetic response of the topography, surfaces defined are the top and the bottom of the model. The top is represented by the subglacial topographic surface defined by BedMachine v.2 data with a resolution of 500 m (Morlighem et al., 2020, Figure 5.5a), re-gridded at 100 m in accordance with our model resolution. The bottom surface is placed at the constant elevation of -2500 m; a different elevation would not have affected the results since the magnetic response of an infinitely elongated flat magnetized layer is zero (Blakely, 1996). The magnetized layer enclosed among the top and the bottom surfaces is characterized by induced magnetization only, with module, inclination and declination of $5\,\mathrm{A/m}$, -83.1° and 133.2° respectively. Such a magnetization module value has been chosen so that computed positive magnetic anomalies match as much as possible with those in our TMA dataset, whereas the inclination and declination agree with those of the Earth's magnetic field in the study area when the survey was flown. The resulting magnetic contribution of the topography is shown in Figure 5.5b. As it can be seen, negative anomalies in our TMA dataset are too intense to be explained by terrain effects due, for example, to subglacial valleys. The only exception relates to the negative anomaly around the western flank of the MM caused by the southern part of the Campbell Glacier valley (Figure 5.5), whose bed has recently been better characterized through a helicopter-borne ice penetrating radar survey (Lee et al., 2021). Elsewhere, we cannot exclude that the deposition of lava flows could have been influenced by valleys excavated by erosion along radial-shaped volcano-tectonic fractures during periods of volcanic quiescence, generating low-amplitude anomalies elongated along the valleys themselves.

Regarding point c), a strong contrast in magnetic mineral content among lava flows and surrounding volcanics is not enough to explain the alternation of strong negative and positive anomalies in our TMA dataset. The proof come from the summit area of MM, characterized

by strong positive magnetic anomalies despite available samples show low values in magnetic remanence module. This suggests local less magnetized volcanics and lava flows do not significantly affect the TMA signal, since it is dominated by surrounding more magnetized rocks.

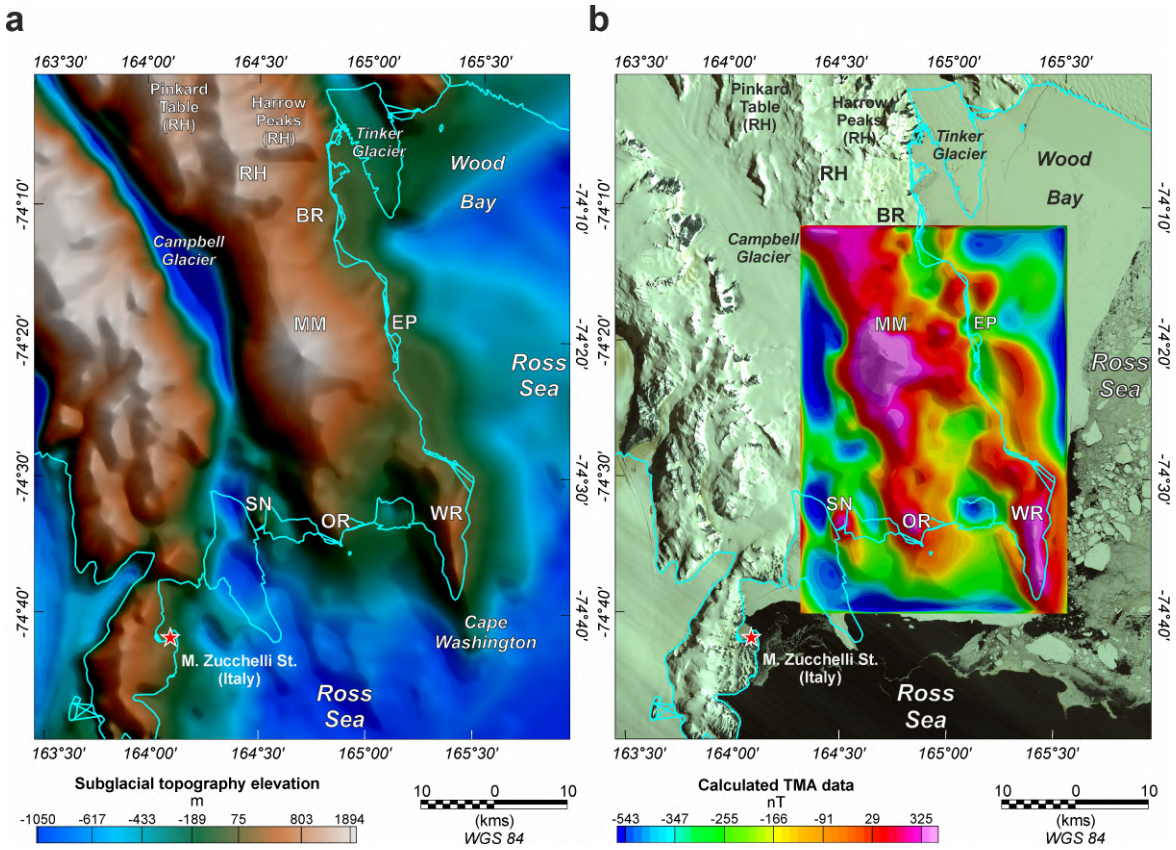

Figure 5.5 - (a) Subglacial topography from BedMachine v.2 data (Morlighem et al., 2020). (b) TMA response of the topography from the 3D Parker's forward model described in sub-section 5.3.3. For abbreviations see caption of Figure 5.1.

In light of above, the best explanation that fits for such strong negative anomalies in our TMA dataset is the occurrence of reversely-polarized rocks, as commonly found in volcanic environments (e.g., Blanco-Montenegro et al., 2018; Dumont et al., 2021). An example come from the Piton des Neiges volcano (Réunion Island), where paleo-valleys excavated in reversely-polarized volcanics and filled by normally-polarized lava flows have been clearly recognized by performing a HRAM survey (Dumont et al., 2021; Martelet et al., 2014). In

this volcano, the magnetic signature of the filled paleo-valleys forms a positive radial pattern surrounded by strong negative anomalies, similarly to that recognized in our TMA dataset.

Moreover, in the MVF reversely-polarized remanence has been found in samples from some outcrops in northern WR, Willows Nunatak (at the south-eastern slope of MM) and in OR area (including Markham Island), indicating volcanic activity during the Matuyama epoch (Figure 5.4b). This evidence is supported by geochronological data older than the last magnetic polarity reversal (i.e., 0.78 Ma) for WR, Willows Nunatak and SN (Figure 5.4b; Table 5.B.1).

Regarding Willows Nunatak / north of WR, close to the reversely-polarized remanence samples, five ages of 2.40±0.10, 1.25±0.09, 1.34±0.07, 1.31±0.09 and 1.32±0.07 Ma were estimated (Armstrong, 1978; Lee et al., 2015). Being Willows Nunatak located at the basal slope of MM, the just described age estimates are a strong clue pointing to a beginning for the magmatic activity that built-up the MM edifice at least during the Matuyama epoch, namely much earlier than ever thought. This hypothesis is strengthened by trachytic xenoliths found in the Mt. Melbourne pyroclastics, interpreted possibly as old as 2.5 Ma (Wörner and Viereck, 1989), placed in time at the beginning of the reverse polarity Matuyama epoch.

For what concern the OR area, the geochronological data available indicates discordant ages of 0.71±0.18 Ma and 0.415±0.024 Ma (Armienti et al., 1991; Giordano et al., 2012). The first age straddles the transition of the Matuyama and Brunhes epochs, while the second is placed in the current Brunhes epoch and appears in disagreement with reversely-polarized remanence data. However, the magnetic signal upon Markham Island shows a local moderate increase in TMA with respect to surrounding strong negative values, suggesting a possible intrusion of a small younger normally-polarized volcanic body. Hence, all evidence suggests this peripheral volcanic center could have formed just before the last magnetic polarity reversal, continuing to develop until more recent ages.

Regarding SN, ages of 1.56 to 1.77 Ma are available for a basal mugearitic lava flow (Kreuzer, 1988; Müller et al., 1991). These ages refer to samples collected above an erosional unconformity separating the basal mugearitic lava flows from overlying younger alkali-basalts interbedded with subaerial tephra (Wörner and Viereck, 1987, 1989), for which two age estimates of 0.48±0.24 and 0.43±0.08 Ma are available (Armienti et al., 1991; Giordano et al., 2012). For the sake of completeness, another age of 0.07±0.05 Ma was documented for an upper alkali basalt flow (Kreuzer, 1988) but would be unlikely and possibly affected by some analytical error (Giordano et al., 2012). An interesting information comes from a normally-polarized remanence sample collected in the basal SN, whose inclination is lower (in absolute value) compared with another near normally-polarized sample, relative to the upper alkali-basalts (Figure 5.4b, see Tables 5.A.1-5.B.1). As a possible explanation for the sample showing lower remanence inclination, Lanza et al. (1991) suggested either (i) outcrop displacement or (ii) lava flow emplaced during a magnetic polarity transition. Following the last hypothesis, the younger portion of the basal mugearitic lava flows could be deposited at the transition among the Matuyama epoch and either the Jaramillo chron or the Brunhes epoch, being the overlying alkali-basalts spread out certainly in the Brunhes epoch as suggested by geochronological data. Moreover, these remanence samples are located at the boundary between a strong positive and negative magnetic anomaly, documenting likely a contact between normal and reverse polarity volcanic products. Therefore, also in this area there is strong evidence of a magmatic activity started prior to the last magnetic polarity reversal.

All the evidence described above are quite strong, being all the normal remanence samples always located upon or near areas of magnetic positive anomaly and *vice versa* all the reverse remanence samples always placed upon or near magnetic negative anomalies (see Figure 5.4b).

In addition, reversely-polarized remanence samples give us other important structural information that would have conditioned first lava depositions. In fact, all these samples show ENE-WSW oriented magnetic lineations (Lanza et al., 1991), suggesting first lava flows driven by NW-SE to N-S fissures on the crystalline basement of the Ross Orogen Wilson Terrane, in the assumption of a low topographic gradient. Magnetic lineations, defined by the directions of maximum susceptibility, are indeed known to commonly reflect the direction of the lava flows (Hrouda, 1982; Tarling and Hrouda, 1993).

In summary, our findings suggest the inner structure of the MVF could be approximated by a NW-SE to N-S elongated thick reversely-polarized volcanic unit built-up during the Matuyama epoch, overlying the Ross Orogen Wilson Terrane, intruded and surmounted by swarms of fault-related dikes and lava flows deposited during normal polarity chrons forming the present-day main volcanic centers.

5.4 Inverse Modeling

All the geophysical evidence discussed above points for the MVF to a general magnetic structure characterized by a basal reversely-polarized volcanic unit, covered locally by an upper normally-polarized one on the main volcanic centers. The magnetic responses of these two units are quite well distinct in the TMA signal, being the long-wavelength components related to the basal reversely-polarized volcanics and the short-wavelength ones to swarms of normally-polarized dikes and related lava flows. Hence, we have applied a two-step procedure to image properly the inner framework of the MVF:

i modeling of long-wavelength components using the 3D Parker-Oldenburg's method;

ii modeling of short-wavelength components by an *ad hoc* developed approach.

Parker-Oldenburg's method (Oldenburg, 1974; Parker, 1973) is an inverse approach based on the Parker's forward algorithm, considering a set of layers with the top and bottom boundaries

defined by arbitrary surfaces, hence it is particularly suitable to define the geometry of the basal reversely-polarized volcanic unit. The upper unit, between the subglacial topography and the top of the basal reversely-polarized unit, is instead modeled using vertical 3D prisms with variable intensity of magnetization (Bhattacharyya, 1964), suitable to image the dike and lava flow distribution that affects in particular MM and WR areas. For this second step, the dataset to invert is the original TMA from which the contribution of the basal reversely-polarized unit, obtained at point (i), is subtracted.

The two-step approach is presented in detail in the next sub-sections 5.4.1 and 5.4.2.

5.4.1 Modeling of long-wavelength signal components

The methodology used to define the main volcanic unitscharacterizing the MVF is based on Parker-Oldenburg's algorithm (Oldenburg, 1974; Parker, 1973) as implemented in the software package GMSYS-3D (Geosoft 8.5 Standard Edition), whose Parker's forward algorithm has been already described at sub-section 5.3.3. The model geometry is, again, 36.5 x 53.1 km wide in the East and North direction respectively, being designed to not include northward the smaller volcanic centers of RH, possibly characterized by different geological settings. In fact, these scattered volcanics are inferred resting directly on the Ross Orogen Wilson Terrane (Figure 5.1b). The top of the model is represented by the subglacial topographic surface defined by BedMachine v.2 data (Morlighem et al., 2020), whereas the bottom surface is placed at the constant elevation of $-2500\,\mathrm{m}$ for the same reason explained in sub-section 5.3.3 about the 3D forward calculation test. According to the hypothesis proposed above about the inner structure of the MVF, the geophysical setup of the model consists of two overlapping layers characterized by opposite magnetic polarity, the deeper reverse and the shallower normal. Since the target of the Parker-Oldenburg's inversion method is represented by the geometry of the surface separating the two magnetic layers, their magnetization properties are maintained constant during the inversion. The starting

elevation of this surface was placed at $-1000\,\mathrm{m}$, below the most depressed topographical point of the MVF. For physical consistency, an underneath layer representing the crystalline basement of the Ross Orogen Wilson Terrane is not entered. The reason of this choice is due to (i) the lack of knowledge about the geometry of the basement and (ii) its negligible magnetic response compared to the overlying strong-remanence volcanic flows, as suggested by susceptibility data available in the literature about the Ross Orogen Wilson Terrane (Bozzo et al., 1991; Talarico et al., 2003, see Figure 5.4a). As a constraint for the inversion results, we have used the magnetic remanences data from Manzoni and Miletto (1988) and Lanza et al. (1991) to define averaged magnetic properties for the two modeled layers (see Table 5.A.1). Magnetic susceptibility has not been considered owing to the high Koenigsberger ratio shown by rock samples from the MVF (Table 5.A.1), suggesting dominant remanence as already explained (see Manzoni and Miletto, 1988). The samples MB4, MB11, MB16, MB21, MB27, MB29 have not been considered for the calculation of the averaged magnetic properties due to their low-angle inclination values, explainable likely by limited gravitational or tectonic displacements (Lanza et al., 1991). Sample MB29 has been discarded as a precaution, because it could also document a magnetic polarity transition. In summary, the deeper layer is set with average values of magnetic remanence module, inclination and declination of $5.63\,\mathrm{A/m}$, 78.02° and 161°, whereas the shallower $8.08\,\mathrm{A/m}$, -75.35° and 143.3° respectively. The Earth's Magnetic Field module, inclination and declination values were $64413.5\,\mathrm{nT}$, -83.1° and 133.2° when the survey was flown.

The results from the inversion are shown in Figure 5.6a-b, in the form of (i) geometry of the inverted contrast surface and (ii) thickness of the shallower volcanic unit with inferred normal polarity. A misfit grid among our TMA dataset and the calculated response of the model from inversion is shown in Figure 5.C.1 in Appendix 5.C. The inverted surface (point i), whose shape has been achieved after 21 iterations, shows pronounced corrugation and seems to image vertical features cutting the underneath reversely-polarized magnetic lava

flows (Figure 5.6a). Similar features, geologically explainable as vertical swarms of feeder dikes, are quite evident in MM area likely as a consequence of the volcanic activity that occurred in the current Brunhes epoch, significantly eroding the basal reversely-polarized unit. For what concerns point (ii), it has been achieved as a difference among the subglacial topography grid with the inverted magnetic contrast surface (Figure 5.6b). Results suggest that the areas in MVF characterized by non-zero thickness of normal polarity volcanic rocks can be found at MM, BR, WR, SN, OR, and in part at EP, namely in the main volcanic centers of the MVF. Elsewhere, reversely-polarized volcanics are expected to outcrop on the subglacial topography, in good agreement with the locations of reversely-polarized magnetic samples (Figure 5.6b).

However, looking at the calculated TMA grid from Parker-Oldenburg's model, it can be noticed that the positive anomalies are not addressed in shape and values, since they lack the radial pattern described in the observed TMA data particularly in the MM and WR areas. On the contrary, the background negative anomaly in the observed and calculated TMA data (see Figure 5.C.1) appears very similar, particularly in shape. Hence, the hypothesis of a basal reversely-polarized volcanic unit with homogenous magnetic properties explains well the long-wavelength components of the TMA signal. The non-fitted short-wavelength components of the TMA data, representing the positive anomalies, point to an upper unit not as homogenous as the basal one, in which the magnetization is expected to vary laterally also in polarity. The reason for this could be found in a more thick reversely-polarized basal volcanic unit intruded by swarms of normally-polarized feeder dikes and surmounted by related lava flows particularly on the MM edifice and WR.

As discussed in the introduction of section 5.4, this lateral variation in magnetization, expected for the shallower parts of the main volcanic centers, is the target of an *ad hoc* developed approach. The detailed settings and results of this methodology are presented in the next sub-section.

5.4.2 Modeling of short-wavelength signal components

Our purpose here is to assess the variability in magnetization expected in the upper volcanic unit of the main sub-suites of the MVF to address the sources of the positive anomalies in the TMA dataset, including the characteristic radial pattern. To accomplish this, we consider the same model geometry used for the Parker-Oldenburg's model and a discretization of the study area involving vertical prisms, whose top is defined by the BedMachine v.2 subglacial topography and the bottom confined by the contrast surface achieved through the previous Parker-Oldenburg's inversion. Vertical prisms, each with horizontal dimensions of 250x250 m, are defined where the subglacial topography does not match the contrast surface (i.e., no zero-thickness of the upper volcanic unit in Parker-Oldenburg's model in the previous sub-section). Hence, the total number of prisms considered is 11219 out of a total of 31311 possible locations. The model parameters are only the intensity of magnetization of each prism, with inclination and declination fixed and equal to that of the inducing Earth's Magnetic Field when the survey was flown (-83.1° and 133.2° respectively). This simplification is possible because at the time of the survey the inducing Earth's magnetic field was almost parallel and anti-parallel to the magnetization vectors obtained from the average magnetic properties of the inferred normally- and reversely-polarized volcanic units presented in sub-section 5.4.1 (the main difference lies in the declination values; however, their effect in the magnetic response decreases approaching the Earth's poles). Hence, positive values in the magnetization module will refer to prisms with magnetization vectors having the same direction as that of the current Earth's magnetic field, whereas negative ones will indicate magnetization vectors aligned to the current Earth's magnetic field but pointing in the opposite direction. The advantages of reducing the model parameters in such a way are (i) the decrease of the number of degrees of freedom of the inverse problem and (ii) the linear relationship between model parameters and calculated data, considering as forward formulae those from Bhattacharyya (1964). As a result, this approach is easy to handle and setup. Such

method shows some similarities with the apparent susceptibility mapping approach (e.g., Grant, 1973; Silva and Hohmann, 1984; Zunino et al., 2009), however, it is characterized by a different setup (i.e., apparent susceptibility mapping assumes prisms infinitely-elongated in depth) and used in a different geological context.

The dataset to invert was re-sampled at a resolution of 250 m for consistency with the model setup, with a total amount of 31311 observation points. This kind of discretization was chosen as a balance between keeping the model resolution high and being able to manage the amount of required computer memory for the matrix representing the forward model. The dataset to invert was obtained by subtracting the total-field magnetic response of the reversely-polarized volcanic unit, whose geometry was figured out through the previous inversion approach, from our TMA dataset. Consequently, the signal obtained should be almost exclusively the response of magnetic sources placed in the upper volcanic unit. The variance associated with each TMA measure is $100\,\mathrm{nT}^2$.

The final model setup is shown in Figure 5.6c. In order to constrain the solution, we have set prior information about the model parameters in the form of a Gaussian probability density function with mean equal to $1\,\mathrm{A/m}$ and variance $0.5\,\mathrm{A}^2/\mathrm{m}^2$ (i.e., same mean and variance for each model parameter). This choice reflects our wish to obtain a smooth and geologically plausible map of the lateral variation of magnetization. Following the probabilistic formulation of a linear inverse problem as described in Tarantola (2005), the solution $\mathbf{m}$ (i.e., the intensity of the vectors of magnetization of prisms) is then given by (see equation (2.17))

$$\mathbf{m} = \left(\mathbf{G}^T \mathbf{C}_\mathrm{D}^{-1} \mathbf{G} + \mathbf{C}_\mathrm{M}^{-1}\right)^{-1} \left(\mathbf{G}^T \mathbf{C}_\mathrm{D}^{-1} \mathbf{d} + \mathbf{C}_\mathrm{M}^{-1} \mathbf{m}_\mathrm{prior}\right), \tag{5.1}$$

where $\mathbf{G}$ is the forward matrix, $\mathbf{d}$ and $\mathbf{C}_\mathrm{D}$ the observed data and the relative covariance matrix, $\mathbf{m}_\mathrm{prior}$ and $\mathbf{C}_\mathrm{M}$ the prior model and its covariance matrix (diagonal in our setting). The related posterior covariance matrix $\tilde{\mathbf{C}}_\mathrm{M}$ is then (see equation (2.18))

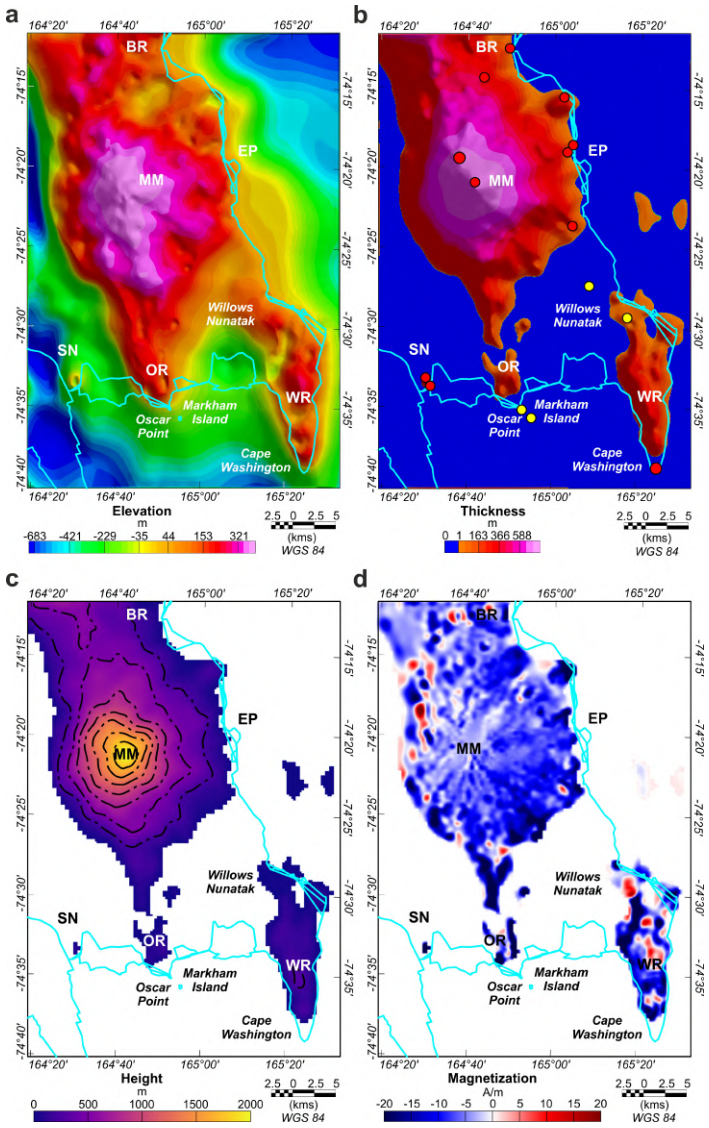

Figure 5.6 - (a) Map showing the elevation of the contrast surface between the basal reversely-polarized unit and the upper volcanic one characterized by highly variable magnetization modules and polarities, resulting from Parker-Oldenburg's inversion. This surface appears very rough, being the reversely-polarized volcanic bottom likely intruded by swarms of normally-polarized feeder dikes. (b) Map of the thickness of the upper volcanic unit obtained as a difference between the subglacial topography and the contrast surface shown in (a). The location of the magnetic remanence polarity samples discussed in sub-section 5.3.2 are superimposed on the map (references in Figure 5.4b). (c) Map showing the location and height of the prisms involved in the *ad hoc* approach used for characterizing the upper volcanic unit inferred on the MVF. Contour lines every 250 meters of height. (d) Map showing the magnetization intensity expected for the upper volcanic unit . For abbreviations in panels (a)-(d), see caption of Figure 5.1.

$$\tilde{\mathbf{C}}_{\mathrm{M}} = \left(\mathbf{G}^{T}\,\mathbf{C}_{\mathrm{D}}^{-1}\,\mathbf{G} + \mathbf{C}_{\mathrm{M}}^{-1}\right)^{-1}. \tag{5.2}$$

The results of the inversion are shown in Figures 5.6d - 5.C.2 in the form of maps of intensity of magnetization and magnetization variance, respectively. For the sake of interpretation, being the magnetic dipole associated with each prism nearly aligned to the vertical, this inversion approach is mostly sensitive to anomalous bodies directly below the respective magnetic anomalies. The calculated TMA data, figured out as the sum of the total-field anomaly due to the basal reversely-polarized volcanic unit from the 3D Parker-Oldenburg's model and the response from the solution using this inversion approach, is shown in Figure 5.C.3 in Appendix 5.C. The calculated data fit very well our short-wavelength TMA dataset. In the areas excluded by this modeling approach, positive peaks visible are likely due to swarms of normally-polarized dikes intruding the reversely-polarized basal unit or directly the low-susceptibility Ross Orogen Wilson Terranes. Overall, our results confirm a high variability in magnetization in the shallower volcanic unit in all areas involved in this inversion, particularly in MM and WR (Figure 5.6d), as supported by field evidence of strong petrographic variability of rocks (Wörner and Viereck, 1989). In MM, low negative values in magnetization affect almost the whole edifice, interrupted by weakly negative to weakly positive ones characterized by a radial pattern retracing that seen in the TMA data. This suggests the reversely-polarized volcanics could reach even the sub-ice topographic surface, interrupted locally by swarm of normally-polarized dikes and lava flows characterized generally by low magnetic susceptibilities / remanences (see Figure 5.C.4 in Appendix 5.C). This hypothesis is corroborated by lower values in the magnetization module and susceptibility shown by normally-polarized rock samples collected in the upper MM (see Table 5.A.1 and references therein). However, such low values could be also due to the influence of the reversely-polarized volcanics below, softening the actual magnetization of normally-polarized dikes and lava flows. Several strong magnetization contrasts are imaged

along the entire western flank of MM toward both the northern part and the southern tip, whose values are likely enhanced by the higher slope of that side of MM causing a greater lateral transition between normally- and reversely-polarized volcanics. Moreover, they could be also associated with local intrusion of swarms of normally-polarized dikes. A similar argument applies for WR, where sharp magnetization contrasts are imaged. Regarding the sub-suites OR and SN, they are too small compared to the model resolution to make any consideration. However, as already pointed out, both geochronological and magnetic remanence data corroborate the co-presence of normally- and reversely-polarized volcanic products.

A schematic view of the internal structure of the MVF is given by a 2D forward model (Talwani and Heirtzler, 1962) performed along a E-W profile shown in Figure 5.4b, discussed in Appendix 5.D (Figure 5.D.1).

As a concluding remark, our models and field magnetic and geochronological data indicate the MVF is constituted by predominant reversely-polarized volcanics forming the main volcanic centers, that are intruded and topped by normally-polarized swarm of dikes and lava flows. The positive anomalies in the TMA dataset, often having radial patterns, would be caused by the magnetization contrast between these oppositely polarized volcanics. Consequently, our results backdate significantly in time the setting in place of the MM stratovolcano, considered formed only during the normal-polarity Brunhes epoch so far.

5.5 Insights into the temporal evolution of the MVF complex

Analysis and modeling of our HRAM data, coupled with available magnetic and geochronological field data, have shown the importance of combining geophysical and geological investigations in remote and ice-covered areas. As a result, we have shed light into the

inner geophysical and geological structure of the main volcanic centers of the MVF. In addition, here we supply new hints to draw an updated reconstruction of the main volcanic phases that built-up the MVF, proposing an evolutionary model that is more in agreement with those proposed by Wörner and Viereck (1989) and Lanza et al. (1991) rather than that by Giordano et al. (2012). All the discussion is based particularly on the results presented in sub-section 5.3.3.

Volcanic activity in MVF is likely to have started at least around the end of the normal polarity Gauss epoch, possibly at WR area (southern MVF) and at other scattered volcanic centers along the eastern coastal area between WR and BR (Figure 5.7a). The long history of WR is recorded by frequent changes in volcanic products (i.e., pillows, lava flows, hyaloclastites, cinder cones, etc), reflecting variable deposition conditions (Wörner and Viereck, 1989). At present, the structures and relics of this volcanic phase could be partially hidden either by the ice cover or by further subsequent volcanic deposits and lavas, so we cannot exclude that the actual MM edifice could be characterized in the deeper part by the presence of older volcanic centers (see Figure 5.7a).

Subsequently to the polarity reversal occurred at the Gauss – Matuyama transition (Figure 5.7b), at first magmatic activity occurred possibly by means of scattered volcanism, generating for example the RH volcanic centers. Afterwards, spread magmatism focused along NW-SE to N-S trending fissures on the crystalline basement of the Ross Orogen Wilson Terrane, from which ENE-WSW trending lava flows established the current reversely-polarized foundation of the entire MVF, developing the bases of the SN, OR, Markham Island, WR and MM volcanic centers.

The normally-polarized volcanics intruding and overlying WR likely started to form during the Olduvai chron, whereas at MM and SN during the subsequent Jaramillo chron (Figure 5.7b). This phase of volcanic activity might have been driven possibly by the already

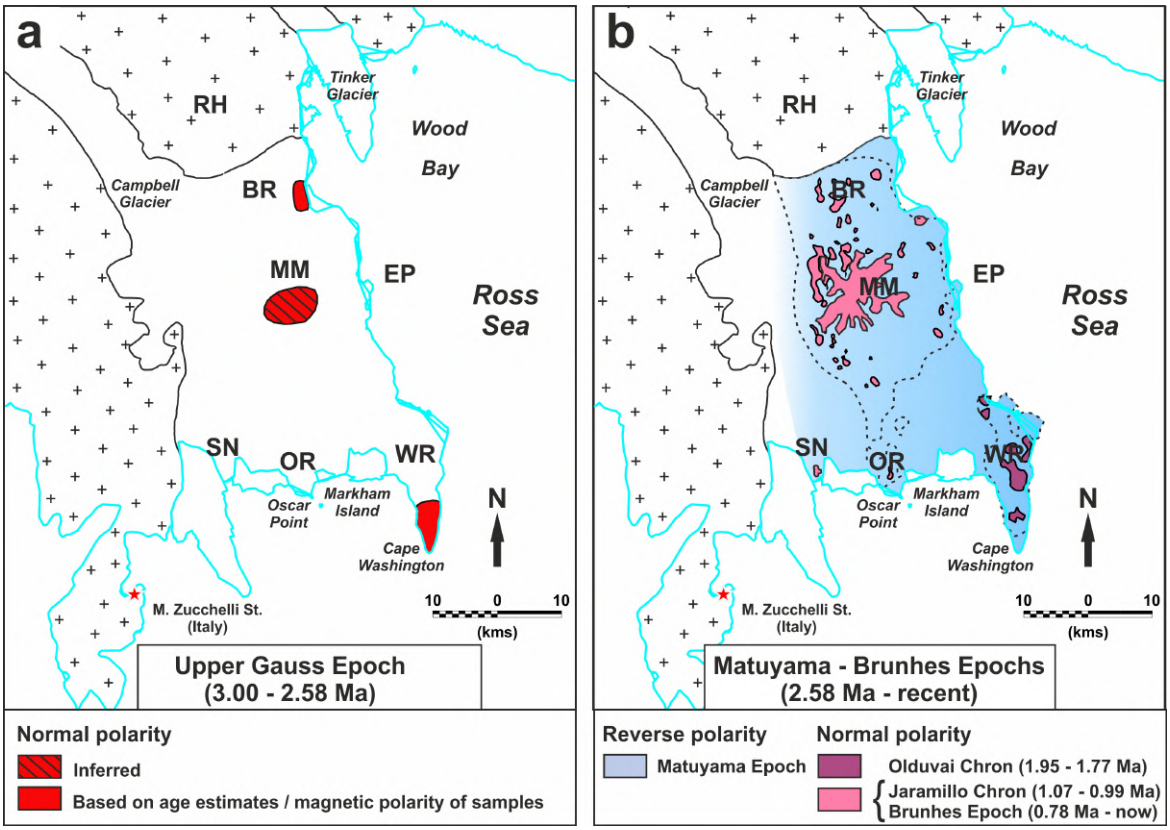

Figure 5.7 - Temporal sequence of the main volcanic phases occurred in MVF. For abbreviations, see caption of Figure 5.1. (a) Volcanics formed at the end of the Gauss epoch. Hypothetical ancestral volcanic activity below the MM is based on our inferences, whereas elsewhere is based on age estimates from Kreuzer (1988) (unpubl. Report quoted in Wörner and Viereck (1989)) and Armienti et al. (1991). (b) Volcanic activity occurred in the Matuyama and Brunhes Epochs. For the sake of coherence, the RH sub-suite is not considered since it has been excluded by our modeling. Dashed lines delimit the main sub-suites interested by normal-polarity volcanic activity, particularly MM and WR, as resulted from modeling results. The shape of dikes and lava flows derives from contouring of magnetizations results discussed in sub-section 5.4.2 and shown in Figure 5.C.4 (Appendix 5.C). The most recent volcanic activity focused on the BR (inland sector), EP and MM sub-suites, in the last assuming a radial shape. The volcanic activity in this period is steered by the activation of the tectonic trend NNE-SSW.

existent NW-SE to N-S trending fissures, facilitating the intrusion of normally-polarized feeder dikes.

After the last polarity reversal (i.e., Matuyama – Brunhes transition, 0.78 Ma) the volcanic activity, at the beginning still active at the satellite centers of OR and SN, progressively

focused on the central and eastern part of the MVF, namely MM, EP and BR inland sector (Figure 5.7b). In this phase, a new set of NNE-SSW trending faults developed on the eastern side of the field, enhancing volcano-tectonic fracturing between the MM edifice and EP and facilitating the intrusion of swarm of dikes and the deposition of lava flows up to recent times, assuming radial shapes at MM owing to its high topographic gradient.

5.6 Concluding remarks

In this chapter we have presented the first detailed aero-magnetic study of the MVF, accomplished combining a novel automatic lineament detection method with a two-step magnetic inversion approach, able to shed light into the sub-ice MVF structure and its temporal evolution.

Automatic lineament detection, performed applying the Hough Transform technique on the TDR of TMA data, has revealed three main structural trends affecting the MVF, oriented N-S, NW-SE and NNE-SSW, that are in good agreement with data from field observations on tectonic structures. TMA data analysis allowed to isolate in the signal two main contributions, that are a large negative long-wavelength and a positive short-wavelength anomaly with radial distribution.

Our two-step magnetic inversion approach, constrained by magnetic property measurements, enabled us to figure out for the MVF a geophysical structure constituted by a main reversely-polarized unit superimposed and intruded by normally-polarized lava flows and dikes. Field evidence for reversely-polarized volcanics comes from some rock samples collected at the basal slope of MM and in the southern peripheral centers. Normally-polarized volcanic flows would locally overlie the reversely-polarized basal unit on the main volcanic centers WR, SN, OR, EP, MM and BR, that on the MM edifice appears eroded by swarm of feeder dikes as a consequence of the longer magmatic activity occurring in this part of the MVF.

Combining our results with available geochronological information from rocks samples collected in the field, we suggest for the MVF a geological history more complex with respect to what was thought so far. In our reconstruction, the starting of a spread magmatic activity would be significantly backdated in time at least at the reverse polarity Matuyama epoch also at MM, driven by NW-SE to N-S fractures on the crystalline basement of the Ross Orogen Wilson Terrane. However, scattered volcanic activity in the north-eastern peripheral center of BR and in the southern tip of WR could have begun even at the end of the normal polarity Gauss epoch. After the last magnetic polarity reversal, volcanic activity progressively moved toward the central portion of the MVF, focusing on the last hundreds/tens of thousands of years on MM and EP. The most recent phase of volcanic activity was driven by a new NNE-SSW trending fault set, reflecting likely an activation of major extensional fault zones along the current coastline (Vignaroli et al., 2015).

Appendices

Introduction

In the Appendices below are shown further data and results completing the discussion about the geophysical characterization of the MVF. In detail:

- in Appendix 5.A, a table listing new magnetic susceptibility data about rocks samples collected in MVF during the 2002/2003 Italian expeditions to Victoria Land is presented, together with already available magnetic properties data collected during both the 2002/2003 and the 1985/1986 Italian Expeditions (Bozzo et al., 1987; Lanza et al., 1991; Manzoni and Miletto, 1988; Pasquale et al., 2009);

- in Appendix 5.B, a table of all age estimates available for the MVF is shown, coupled for each sub-suite with magnetic remanence inclinations data;

- in Appendix 5.C, additional results about the inversion approaches used to reconstruct the inner framework of the volcanic complex are displayed;

- in Appendix 5.D, a 2D forward model along a E-W profile on the MM edifice is provided, in order to give a schematic view of the internal architecture of the MVF imaged through the results from our two-step inversion approach.

Appendix 5.A Magnetic property data

Sample	Source	Locality	Latitude	Longitude	Elevation	χ	χstd	$\lvert M_r \rvert$	M_r incl.	M_r decl.	Q
MB1	*	Mario Zucchelli Station	-74.70	164.12	NA	1027	NA	1.2	79.1	48.6	2.4
MB2	*	Cape Washington	-74.64	165.42	NA	4592	NA	2.6	-72.6	10.6	1.1
MB3	*	Cape Washington	-74.64	165.42	NA	3763	NA	7.9	-74.4	232.5	4.2
MB4	*	SE of Random Hills	-74.10	164.41	NA	2769	NA	0.5	-34.2	31.2	0.3
MB6	*	N of Edmonson Point	-74.26	165.04	NA	3514	NA	13.5	-75.3	25.3	7.4
MB7	*	NE of Baker Rocks	-74.22	164.84	NA	243	NA	0.05	-85.3	31.6	0.5
MB11	*	S of Random Hills	-74.18	164.33	NA	619	NA	2.9	-56.8	238.6	9.8
MB14	*	W of Tinker Glacier	-73.90	164.39	NA	2076	NA	9.1	75.1	285.3	8.2
MB15	*	Tinker-Burns Glaciers	-73.94	164.41	NA	2195	NA	8.4	73.3	318.0	7.6
MB16	*	S of Miller Nunatak	-74.45	164.07	NA	4210	NA	2.0	-48.9	210.9	0.9
MB17	*	Willows Nunatak	-74.49	165.31	NA	1680	NA	9.4	76.2	42.9	10.4
MB18	*	N of Willows Nunatak	-74.46	165.15	NA	572	NA	1.1	82.1	243.4	3.8
MB19	*	S of Edmonson Point	-74.39	165.06	NA	2274	NA	21.9	-68.5	234.9	18.2
MB21	*	Markham Island	-74.59	164.93	NA	3275	NA	1.8	42.2	275.8	1.0
MB22	*	S of Harrows Peaks	-74.09	164.80	NA	3480	NA	10.4	-80.6	149.9	5.7
MB23	*	S of Harrows Peaks	-74.09	164.80	NA	343	NA	6.8	-68.1	173.9	33.7
MB24	*	S of Harrows Peaks	-74.09	164.80	NA	2785	NA	23.4	-78.6	26.7	16.7
MB25	*	Baker Rocks	-74.23	164.75	NA	2295	NA	12.0	-80.2	141.9	10.0
MB26	*	N of Edmonson Point	-74.31	165.07	NA	251	NA	3.1	-62.3	214.9	31.4
MB27	*	N of Edmonson Point	-74.32	165.06	NA	186	NA	5.0	-54.0	100.7	55.5
MB28	*	Oscar Point	-74.58	164.88	NA	6214	NA	4.6	82.3	27.8	1.4
MB29	*	Shield Nunatak	-74.56	164.53	NA	130	NA	2.5	-39.1	198.8	41.3
MB30	*	Upper Mt. Melbourne	-74.32	164.64	NA	129	NA	0.3	-86.0	269.7	5.6
MB31	*	Upper Mt. Melbourne	-74.35	164.69	NA	961	NA	0.8	-77.4	23.5	1.5
MB32	*	Shield Nunatak	-74.55	164.51	NA	136	NA	2.3	-70.3	327.3	32.2
WR1	**	Washngton Ridge	-74.61	165.44	NA	4486	11	NA	NA	NA	NA
WR2	**	Washngton Ridge	-74.59	165.43	NA	231	1	NA	NA	NA	NA
WR3	**	Washngton Ridge	-74.58	165.39	NA	3622	5	NA	NA	NA	NA
WR4	**	N of Washington Ridge	-74.49	165.28	NA	898	18	NA	NA	NA	NA
WR5	**	N of Washington Ridge	-74.48	165.35	NA	4057	3	NA	NA	NA	NA
WR6	**	N of Washington Ridge	-74.47	165.26	NA	2096	2	NA	NA	NA	NA
WR7	**	N of Washington Ridge	-74.48	165.40	NA	494	4	NA	NA	NA	NA
EP1	**	N of Edmonson Point	-74.31	164.99	NA	1904	4	NA	NA	NA	NA
EP2	**	Edmonson Point	-74.33	165.12	NA	338	5	NA	NA	NA	NA
EP3	**	Edmonson Point	-74.33	165.14	NA	822	1	NA	NA	NA	NA
EP4	**	Edmonson Point	-74.36	165.09	NA	879	17	NA	NA	NA	NA
EP5	**	S of Edmonson Point	-74.37	165.11	NA	1764	6	NA	NA	NA	NA
EP6	**	Willows Nunatak	-74.46	165.13	NA	1805	3	NA	NA	NA	NA
SN1	**	Shield Nunatak	-74.54	164.50	NA	298	1	NA	NA	NA	NA
BR1	**	Baker Rocks	-74.23	164.74	NA	791	3	NA	NA	NA	NA
BR2	**	Baker Rocks	-74.20	164.65	NA	813	1	NA	NA	NA	NA
BR3	**	Baker Rocks	-74.21	164.80	NA	4617	2	NA	NA	NA	NA
BR4	**	S of Baker Rocks	-74.29	164.70	NA	2243	9	NA	NA	NA	NA
MM1	**	Medium Mt. Melbourne	-74.31	164.66	NA	119	1	NA	NA	NA	NA
MM2	**	Upper Mt. Melbourne	-74.35	164.62	NA	648	1	NA	NA	NA	NA
TIMM1	***	Shield Nunatak	-74.55	164.51	195	1650	NA	NA	NA	NA	NA
TIMM2	***	Teall Nunatak	-74.84	162.54	264	220	NA	NA	NA	NA	NA
TIMM3	***	Gondwana Station	-74.64	164.22	NA	28	NA	NA	NA	NA	NA
TIMM4	***	Willows Nunatak	-74.50	165.28	381	2390	20	NA	NA	NA	NA
TIMM5	***	Willows Nunatak	-74.49	165.29	397	785	41	NA	NA	NA	NA
TIMM6	***	Willows Nunatak	-74.48	165.34	145	1905	57	NA	NA	NA	NA
TIMM7	***	Willows Nunatak	-74.47	165.26	195	1338	48	NA	NA	NA	NA
TIMM8	***	Willows Nunatak	-74.46	165.13	275	149	7	NA	NA	NA	NA
TIMM9	***	Willows Nunatak	-74.48	165.36	104	1750	67	NA	NA	NA	NA
TIMM10	***	Edmonson Point	-74.32	164.99	545	1887	68	NA	NA	NA	NA
TIMM11	***	Edmonson Point	-74.33	165.11	28	3175	65	NA	NA	NA	NA
TIMM12	***	Edmonson Point	-74.33	165.11	165	744	23	NA	NA	NA	NA
TIMM13	***	Edmonson Point	-74.34	165.14	150	1460	NA	NA	NA	NA	NA
TIMM14	***	Edmonson Point	-74.35	165.08	271	2380	91	NA	NA	NA	NA
TIMM15	***	Edmonson Point	-74.36	165.13	13	2553	74	NA	NA	NA	NA
TIMM16	***	Cape Washington	-74.63	165.44	300	2468	93	NA	NA	NA	NA

Table 5.A.1 - New and already available magnetic susceptibility and remanence data achieved from rock samples collected in MVF. χ and χstd columns list magnetic susceptibility values and their standard deviations respectively, expressed in terms of 10^{-5} SI units. Remanence modules $\lvert M_r \rvert$ refer to Natural Remanent Magnetization (NRM), whereas inclinations M_r incl. and declinations M_r decl. to a more precise Thermo-Remanent Magnetization (TRM), albeit the rocks samples of the MVF show secondary magnetization components absent or negligible (Lanza et al., 1991). Q is the Koenigsberger ratio. Data source: *Lanza et al. (1991); Manzoni and Miletto (1988). **Pasquale et al. (2009). ***This study.

Appendix 5.B Age estimates vs magnetic remanence data

Volcanic sub-suite	Geochronology (Ma)	Age source	M_r incl. (°)
Washington Ridge (WR)	1.250 ± 0.090	###	-74.4
	1.310 ± 0.090	###	-72.6
	1.320 ± 0.070	###	76.2
	1.340 ± 0.070	###	
	1.670 ÷ 2.700	**	
	1.680 ± 0.190	#	
	2.720 ± 0.170	#	
Willows Nunatak	2.400 ± 0.100	*	82.1
Oscar Ridge (OR)	0.415 ± 0.024	##	42.2
	0.710 ± 0.180	***	82.3
Shield Nunatak (SN)	0.070 ± 0.050	**	-70.3
	0.431 ± 0.082	##	-39.1
	0.480 ± 0.240	***	
	1.560 ÷ 1.770	**	
	1.610 ± 0.050	#	
	1.650 ± 0.040	#	
	1.740 ± 0.030	#	
Mt. Melbourne edifice (MM)	0.010 ± 0.020	*	-86.0
	0.015 ± 0.035	**	-77.4
	0.070 ± 0.010	###	
	0.080 ± 0.015	*	
	0.120 ± 0.020	###	
	0.250 ± 0.060	*	
	0.250 ± 0.350	#	
Edmonson Point (EP)	0.047 ± 0.021	#	-75.3
	0.050 ± 0.020	**	-68.5
	0.074 ± 0.110	**	-62.3
	0.112 ± 0.084	##	-54.0
	0.119 ± 0.012	##	
	0.298 ± 0.055	##	
	0.900 ± 1.150	#	
Baker Rocks (BR)	0.190 ± 0.040	*	-85.3
	0.200 ± 0.010	###	-80.2
	0.200 ± 0.010	###	
	0.280 ± 0.030	###	
	0.330 ± 0.030	###	
	0.720 ± 0.100	*	
	2.590 ± 0.110	***	
	2.960 ± 0.200	***	
Random Hills (RH)	0.745 ± 0.066	##	-80.6
	1.368 ± 0.090	##	-78.6
	12.430 ± 0.160	***	-68.1
	12.630 ± 0.170	***	-56.8
			-34.2

Table 5.B.1 - Age estimates and remanence inclination data available for each sub-suite composing the MVF (sorted from south to north). M_r incl. data refer to Thermo-Remanent Magnetization (TRM) inclinations (Lanza et al., 1991). Data source: *Armstrong (1978); **Kreuzer (1988) - unpubl. report; ***Armienti et al. (1991); #Müller et al. (1991); ##Giordano et al. (2012); ###Lee et al. (2015).

Appendix 5.C Further modeling results

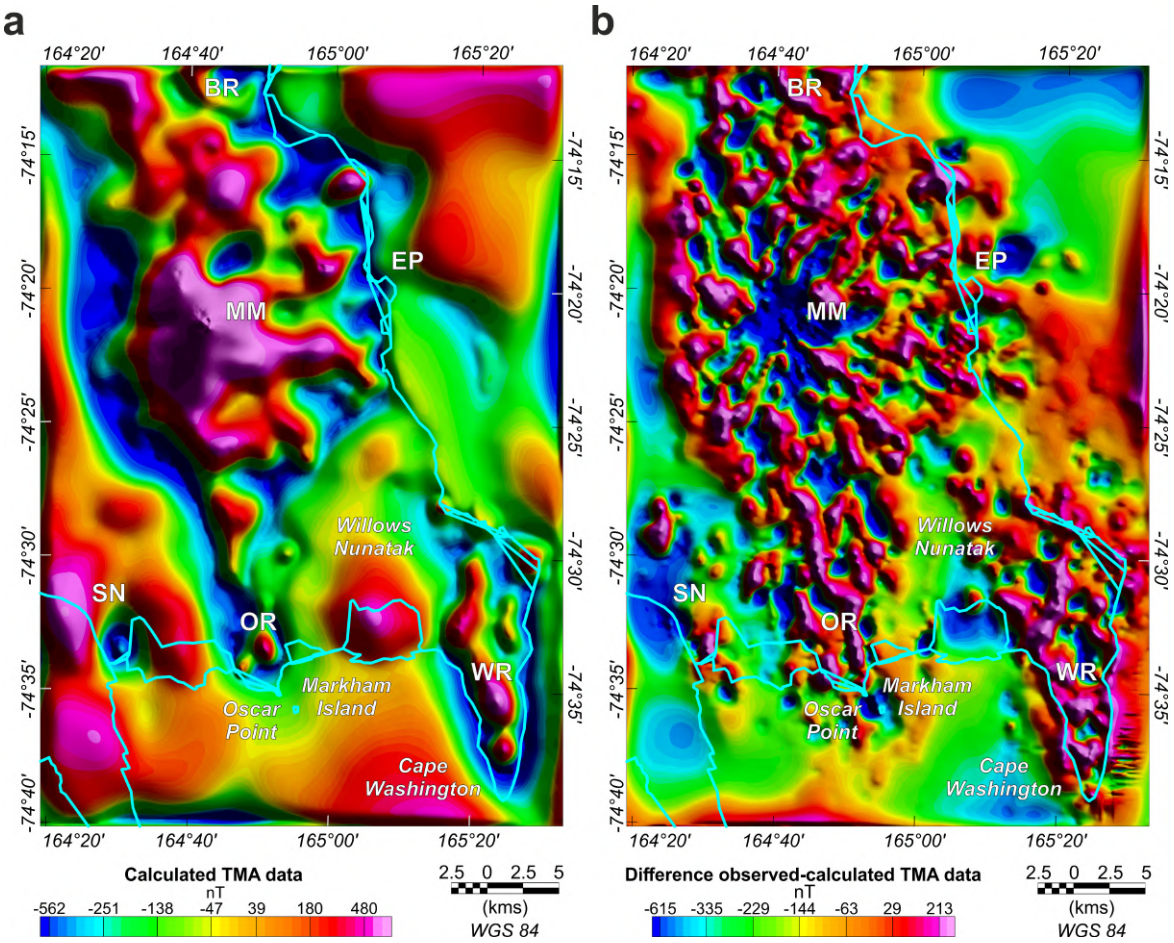

Figure 5.C.1 - (a) TMA calculated data, representing the response of the model obtained by the inversion approach described in sub-section 5.4.1, whose results are shown in Figures 5.6a-b (main text) in terms of geometry of the inverted contrast surface and thickness of the shallower volcanic stratum with inferred normal polarity. (b) Grid difference between our TMA dataset and the calculated response of the model from inversion displayed in (a). For abbreviations on both the panels, see Figure 5.1 in the main text.

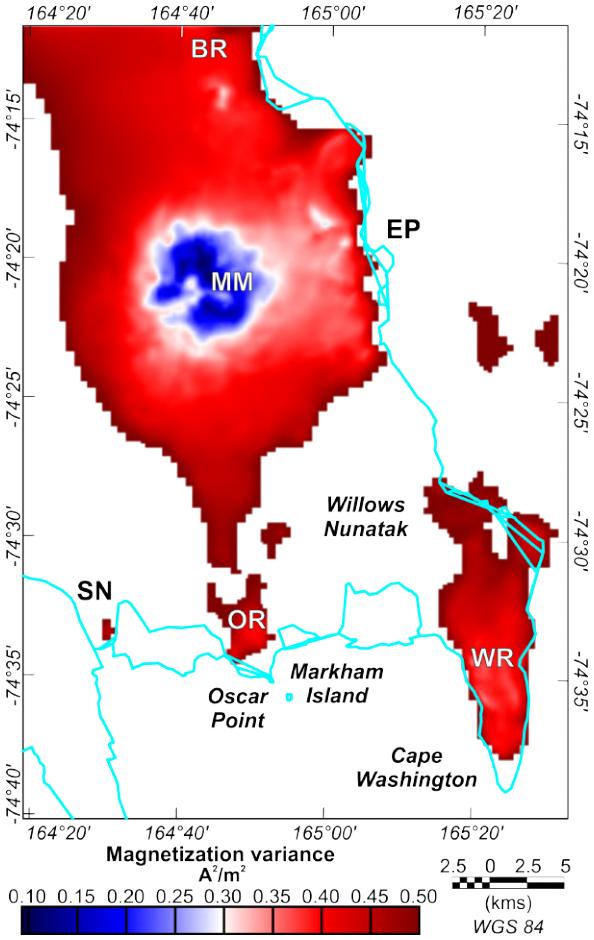

Figure 5.C.2 - Map showing the magnetization intensity variance expected for the upper volcanic unit, obtained extracting the diagonal elements from the posterior covariance matrix $\tilde{\mathbf{C}}_{\mathrm{M}}$ calculated using the equation (5.2). It should be noticed that $\tilde{\mathbf{C}}_{\mathrm{M}}$ together with the model $\mathbf{m}$, achieved solving equation (5.1), fully characterize the posterior PDF of the model parameters $\sigma(\mathbf{m})$, representing the actual solution using the deterministic inversion approach described in sub-section 5.4.2 (see paragraph "Linear case - Deterministic approach"). For abbreviations, see Figure 5.1 in the main text.

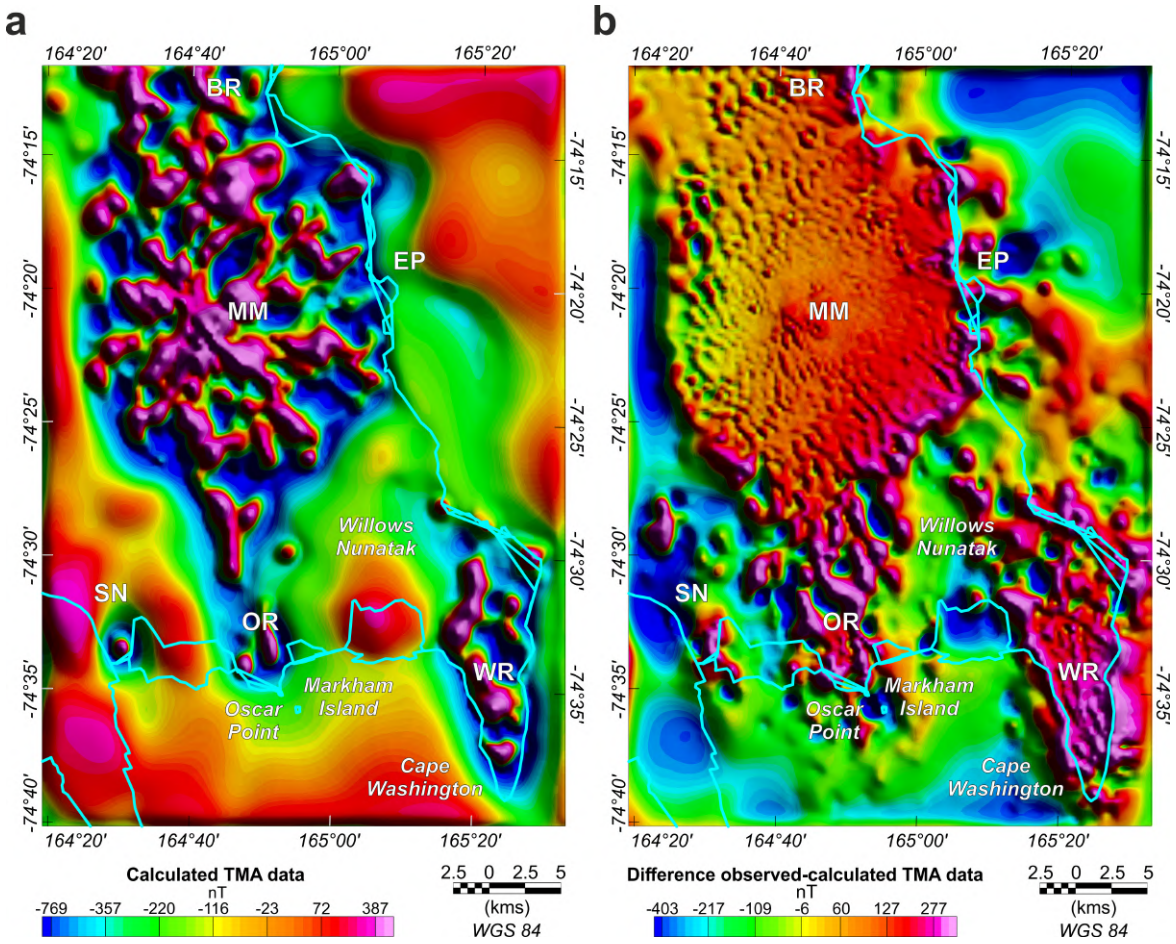

Figure 5.C.3 - (a) TMA calculated data, representing the response of the model obtained by the inversion approach described in sub-section 5.4.2, whose results are shown in Figure 5.6d (main text) in terms of 2D map of apparent magnetization. (b) Grid difference between our TMA and the response obtained summing the contribution shown in (a) with that calculated from the contrast surface achieved through the 3D Parker-Oldenburg's method shown in Figure 5.6a (main text). For abbreviations on both the panels, see Figure 5.1 in the main text.

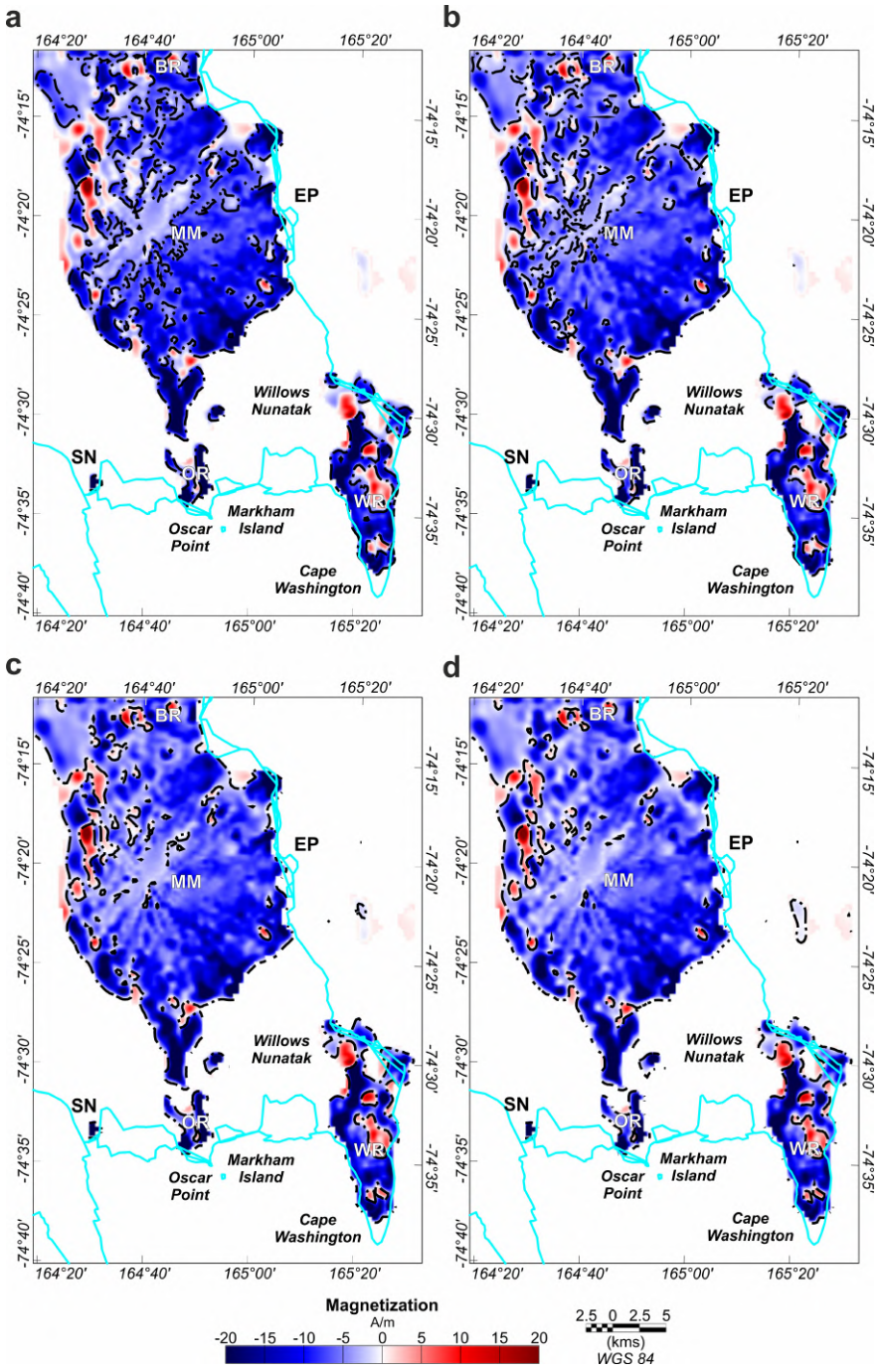

Figure 5.C.4 - Maps of the lateral magnetization variability in MVF obtained through the inversion approach described in sub-section 5.4.2. The differences between the Figures (a), (b), (c) and (d) are related to the contour values of apparent magnetization chosen, that are $-5, -3, -1$ and $0\,\mathrm{A/m}$ respectively. The reader can notice the contours at -5 and $-3\,\mathrm{A/m}$ clearly draw radial shapes similar to that shown by TMA data, suggesting the positive anomalies in the TMA data are due to the magnetization contrast among normal-polarized lava flows deposited on underlying reverse-polarized volcanics. Regarding the contours of higher magnetizations, radial shapes become circular spots, well imaging dikes intruding the reverse-polarized volcanic edifice of MM and WR. For abbreviations, see Figure 5.1 in the main text.

Appendix 5.D 2D section of the MVF

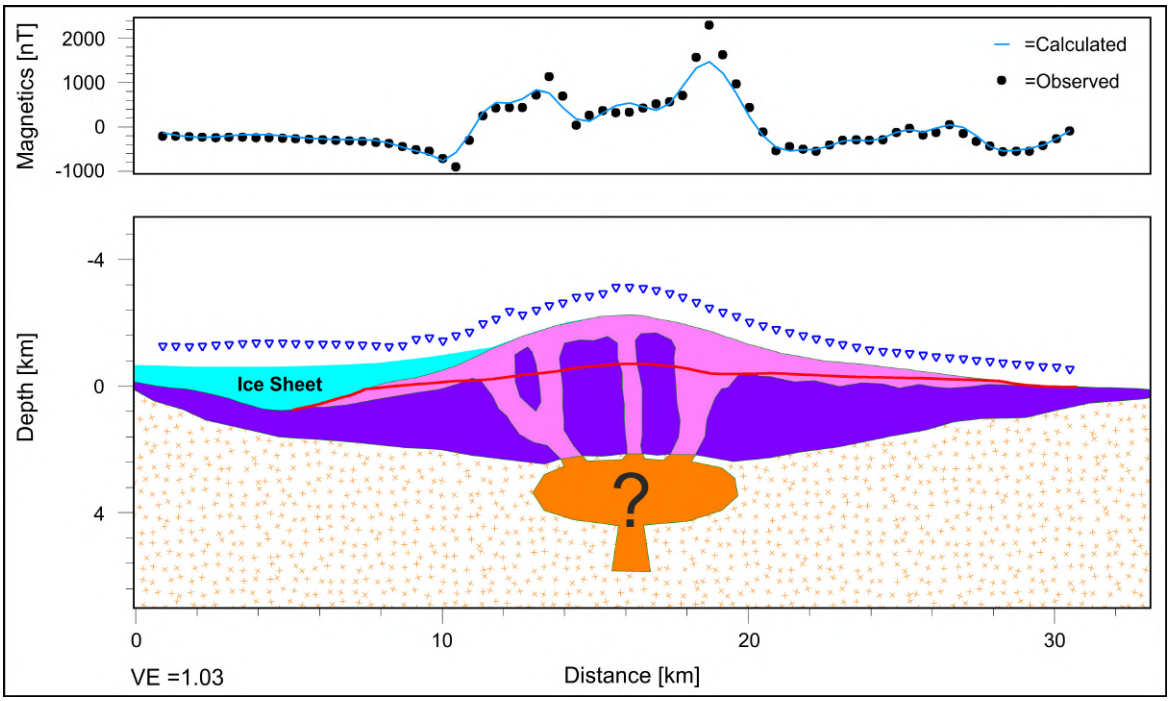

Figure 5.D.1 - 2D forward model showing the inner structure below MM along the E-W profile displayed in Figure 5.4b in the main text (vertical exaggeration equal to 1.03). A total number of 69 observation points are indicated as inverted blue triangles in the second panel, whereas the respective measured data and the calculated response of the model are shown in the first panel. In pink are modeled normally-polarized lava flows and fault-related dikes, whereas in purple reversely-polarized volcanics. The magnetic properties associated to them are only magnetic remanence, with module, inclination and declination of $8.08\,\mathrm{A/m}$, $-75.35°$, $143.3°$ and $5.63\,\mathrm{A/m}$, $78.02°$, $161°$ respectively (same values used for the 3D Parker-Oldenburg's inversion). Below is the Ross Orogen Wilson Terrane, to which is associated only magnetic susceptibility equal to $0.28 \cdot 10^{-3}$SI (see Figure 5.4a in the main text). In orange is qualitatively indicated a magma chamber, whose actual existence, position and extension are unknown. For a comparison, the trace of the contrast layer among inferred normally- and reversely-polarized volcanics obtained through the Parker-Oldenburg's inversion method is placed on the model. It can be noticed that this contrast surface matches the respective in the 2D forward model particularly toward the external part of MM, where the approximation of two overlapping strata with opposite magnetic properties works well. Conversely, this approximation does not work anymore for the central part of the MM affected by the intrusion of normally-polarized feeder dikes, rather causing a lateral variability in magnetization properties and polarities.

Part IV

Final considerations

Conclusions

Final remarks

Despite the great efforts made by geophysicists to manage the non-uniqueness affecting potential fields inverse problems, gravity and magnetic modeling still suffers from a lack of methodologies capable of characterizing in an informative way the density and magnetization distribution inferred for a target geological scenario. Moreover, the strong non-linearity characterizing the forward problem of some parameterization approaches makes the related inverse problem very hard to be managed and setup. For such reason, the popular polygon-based parameterization approach, potentially suitable to parameterize a wide range of geological scenarios, has been confined on a trivial trial-and-error modeling strategy, strongly subjective and then unable to take into account the non-uniqueness issue. Conversely, linear inversion problems based on the prism-based parameterization are comfortably tackled from a deterministic viewpoint, which provides as solution just an optimal model preventing a more informative uncertainty estimation distinctive of probabilistic approaches.

This thesis aimed to bridge these gaps, proposing (i) a non-linear polygon-based inversion method of gravity and magnetic data following the probabilistic approach to inverse problems, and (ii) a linear probabilistic inversion method exploiting an unedited version of the prism-based parameterization strategy.

As far as the contribute (i), a preparatory complete study on the polygon-based parameterization approach has been performed, starting from a validation of its theoretical framework.

In detail, in chapter 3 we have analyzed all the forward formulations available for the 2D magnetic case, restoring the mathematical correctness of the popular derivation of Talwani and Heirtzler (1962, 1964), whose validity has been recently questioned by Kravchinsky et al. (2019). In fact, we have demonstrated that the two derivations actually are just two algebraic variants of a unique mathematical derivation, and a numerical test comparing them with another formulation from Won and Bevis (1987) confirmed complete agreement. The impact of actual mathematical weaknesses on the Talwani's derivation would have been significant, since the majority of forward engines are based on it. Such mathematical checks have been extended in chapter 4 to the 2.5D to 2.75D gravity and magnetic cases (Campbell, 1983; Rasmussen and Pedersen, 1979), completing the puzzle about polygon-based parameterization approaches. An error sign has been revealed for the 2.75D magnetic case, supported by a numerical comparison with a forward engine exploiting the prism-based parameterization approach (Bhattacharyya, 1964).

All formulae, rectified when necessary, have been employed as forward problems to develop, still in chapter 4, a methodology to invert gravity and magnetic data, independently or jointly, based on the Hamiltonian Monte Carlo (HMC) scheme (Duane et al., 1987; Fichtner et al., 2019; Neal, 2012). HMC is an efficient probabilistic inversion approach which proved to be capable of fully characterizing the geometries of synthetic- and real-case geological bodies by means of collections of models, upon which statistical analysis and uncertainty estimation on the model parameters have revealed helpful information to characterize a geological scenarios under study. Using this inversion method, the geological plausibility of a model explored is automatically checked or, if required, fixed, in order to avoid unrealistic cross-intersection between polygons. In addition, all the code required for the 2D to 2.75D gravity and magnetic forward problems, together with the HMC inversion method exploiting them, has been released as open-source packages in order to make

accessible to the geophysical community this progress in potential fields modeling (see section "Open-source software" for more details).

As regards the contribution (ii), the inversion method has been developed following the probabilistic viewpoint, which provide both the posterior model and the related covariance matrix, fully characterizing the posterior PDF of the model parameters. Using this methodology, a geological scenario is parameterized by prismatic bodies extended in the z direction neither infinitely, as in the case of the Apparent Susceptibility Mapping method (e.g., Grant, 1973; Silva and Hohmann, 1984; Zunino et al., 2009), nor finitely with a 3D arrangement. Here, differently from the Apparent Susceptibility Mapping method, prisms are infinitely extended in the z direction but arranged in order to horizontally cover the geophysical body we would like to parameterize, making this method particularly suited to characterize the density and magnetization variability on geological strata. In this thesis, this approach has been employed to fully characterize the magnetization variability of the shallower volcanic unit of the Mt. Melbourne Volcanic Field (Antarctica), contributing to reveal for the first time its inner geophysical architecture. However, this method can be easily exploited for the gravity case substituting the magnetic forward equation from Bhattacharyya (1964) with the gravity forward formulae from either Nagy (1966) or Banerjee and Das Gupta (1977).

As a final consideration, the 2D/2.75D polygon-based HMC inversion method presented in this thesis would also serve as a basis for developing, in the next future, a sophisticated 3D inversion methodology of gravity and magnetic data, as briefly discussed in the next section.

Future perspectives

Following my professional aim to move toward 3D inverse modeling methodologies, a future outlook of this thesis work would be to develop a 3D joint gravity and magnetic inversion method, combining an elegant parameterization of geological bodies through polyhedra with a fully nonlinear inversion strategy based on the probabilistic approach. In detail,

polyhedra with uniform to high-order polynomial density and magnetization contrasts would allow to characterize geological bodies in the subsurface in a sharp, flexible and faithful fashion, whose gravity and magnetic contributes can be calculated through recently derived mathematical formulations (Ren et al. (2020) and Ren et al. (2022) for the gravity and the magnetic case, respectively). The polyhedron-based parameterization can be considered as the 3D expansion of the 2D/2.75D polygon-based approach discussed in chapters 2 - 3 - 4, since for both model parameters can be either the density/magnetization or node positions of bodies. Such possibility makes the proposed method suitable for most of the cases where gravity and magnetic modeling is required.

As inversion approach, the choice would rely again on the promising HMC strategy, since it allows the model space to be explored more efficiently thanks to trajectories that are steered toward its high-probability areas by the gradient calculation of the posterior PDF of the model parameters (Neal, 2012). A reduced amount of prior information and number of iterations would be thus required to better characterize the model null space with respect to other sampling strategies, making the inversion easier to setup and less time-consuming. Moreover, using HMC makes it possible to perform a statistical analysis and uncertainty estimation of the model parameters from the collection of posterior models, enabling to appraise different probable geological scenarios (e.g., see section 4.4).

The only issue about the polyhedral parameterization, in common with the 2.75D polygonal one, would be the hazard to achieve during the inversion process bodies self-crossing each other. Hence, an automatic geometry checks system controlling the evolution of bodies shape would be required to make the method feasible. The set of routines performing these checks would represent the 3D evolution of those already implemented in the Julia package GeoPolygons in the context of the 2D/2.75D polygonal parameterization (see Appendix 4.C).

References

Adamson, R. G. and Cavaney, R. J. (1967). Volcanic Debris-Layers near Mount Melbourne, Northern Victoria Land, Antarctica. *New Zealand Journal of Geology and Geophysics*, 10(2):418–421.

Armadillo, E., Bozzo, E., Gambetta, M., and Rizzello, D. (2012). Impact of human activities on the geomagnetic field of Antarctica: A high resolution aeromagnetic survey over Mario Zucchelli Station. *Environment International*, 47:1–7.

Armadillo, E., Ferraccioli, F., Zunino, A., Bozzo, E., Rocchi, S., and Armienti, P. (2007). Aeromagnetic search for Cenozoic magmatism over the Admiralty mountains block (East Antarctica). In *Antarctica: A Keystone in a Changing World–Online Proceedings of the 10th ISAES, edited by AK Cooper and CR Raymond et al., USGS Open-File Report*, volume 1047.

Armadillo, E., Rizzello, D., Pasqua, C., Pisani, P., Ghirotto, A., Kabaka, K., Mnjokava, T., Mwano, J., Didas, M., and Tumbu, L. (2020). Geophysical Constraints on the Luhoi (Tanzania) Geothermal Conceptual Model. *Geothermics*, 87:101875.

Armienti, P. and Baroni, C. (1999). Cenozoic climatic change in Antarctica recorded by volcanic activity and landscape evolution. *Geology*, 27(7):617.

Armienti, P., Civetta, L., Innocenti, F., Manetti, P., Tripodo, A., and Villari, L. (1991). New petrological and geochemical data on Mt. Melbourne Volcanic Field, Northern Victoria Land, Antarctica (II Italian Antarctic Expedition). *Memorie della Società Geologica Italiana*, 46:397–424.

Armienti, P., Ghezzo, C., Innocenti, F., Manetti, P., Rocchi, S., and Tonarini, S. (1988). Palaeozoic and Cainozoic intrusives of Wilson Terrane: geochemical and isotopic data. *Memorie della Società Geologica Italiana*, 43:67–75.

Armstrong, R. L. (1978). K-Ar dating: Late Cenozoic McMurdo Volcanic Group and dry valley glacial history, Victoria Land, Antarctica. *New Zealand Journal of Geology and Geophysics*, 21(6):685–698.

Aster, R. C., Thurber, C. H., and Borchers, B. (2005). *Parameter estimation and inverse problems*. Number v. 90 in International geophysics series. Elsevier Academic Press, Amsterdam ; Boston. OCLC: ocm57470064.

Banerjee, B. and Das Gupta, S. (1977). Gravitational attraction of a rectangular parallelepiped. *Geophysics*, 42(5):1053–1055.

Baranov, A., Tenzer, R., and Bagherbandi, M. (2018). Combined Gravimetric–Seismic Crustal Model for Antarctica. *Surveys in Geophysics*, 39(1):23–56.

Bath, G. D. (1962). Magnetic anomalies and magnetizations of the Biwabik iron-formation, Mesabi area, Minnesota. *Geophysics*, 27(5):627–650.

Bayes, T. (1763). LII. An essay towards solving a problem in the doctrine of chances. By the late Rev. Mr. Bayes, FRS communicated by Mr. Price, in a letter to John Canton, AMFR S. *Philosophical transactions of the Royal Society of London*, (53):370–418. Publisher: The Royal Society London.

Beccaluva, L., Civetta, L., Coltorti, M., Orsi, G., Saccani, E., and Siena, F. (1991a). Basanite to tephrite lavas from Melbourne volcanic province, Victoria Land, Antarctica. *Memorie della Società Geologica Italiana*, 46:383–395.

Beccaluva, L., Coltorti, M., Orsi, G., Saccani, E., and Siena, F. (1991b). Nature and evolution of the sub-continental lithospheric mantle of Antarctica: evidence from ultramafic xenoliths of the Melbourne Volcanic Province (Northern Victoria Land, Antarctica). *Memorie della Società Geologica Italiana*, 46:353–370.

Betancourt, M. (2017). A Conceptual Introduction to Hamiltonian Monte Carlo. *arXiv:1701.02434 [stat]*. arXiv: 1701.02434.

Bezanson, J., Edelman, A., Karpinski, S., and Shah, V. B. (2017). Julia: A Fresh Approach to Numerical Computing. *SIAM Review*, 59(1):65–98.

Bhattacharyya, B. (1964). Magnetic anomalies due to prism-shaped bodies with arbitrary polarization. *Geophysics*, 29(4):517–531.

Bhattacharyya, B. K. and Chan, K. C. (1977). Computation of gravity and magnetic anomalies due to inhomogeneous distribution of magnetization and density in a localized region. *Geophysics*, 42(3):602–609.

Bhattacharyya, B. K. and Navolio, M. E. (1975). Digital convolution for computing gravity and magnetic anomalies due to arbitrary bodies. *Geophysics*, 40(6):981–992.

Bhattacharyya, B. K. and Navolio, M. E. (1976). A fast Fourier transform method for rapid computation of gravity and magnetic anomalies due to arbitrary bodies. *Geophysical Prospecting*, 24(4):633–649.

Bindschadler, R., Vornberger, P., Fleming, A., Fox, A., Mullins, J., Binnie, D., Paulsen, S., Granneman, B., and Gorodetzky, D. (2008). The Landsat Image Mosaic of Antarctica. *Remote Sensing of Environment*, 112(12):4214–4226.

Blakely, R. J. (1996). *Potential Theory in Gravity and Magnetic Applications*. Cambridge University Press.

Blanco-Montenegro, I., Montesinos, F. G., and Arnoso, J. (2018). Aeromagnetic anomalies reveal the link between magmatism and tectonics during the early formation of the Canary Islands. *Scientific Reports*, 8(1):42.

Blokh, Y. (1980). Calculation of the magnetic field due to two-dimensional anisotropic objects of arbitrary sections with consideration of demagnetization. Izvestiya. *Earth Physics*, 16(2):126–130.

Bonaccorso, A., Falzone, G., Gambino, S., and Villari, L. (1995). Tilt signals recorded at Mt Melbourne Volcano (Northern Victoria Land, Antarctica) between 1989–94. *Terra Antartica*, 2(2):111–116.

Bonaccorso, A., Gambino, S., Falzone, G., Privitera, E., and Morelli, A. (1996). Physics volcanological studies in the activity framework of the Mt. Melbourne Observatory (northern Victoria Land, Antarctica). *Italian geophysical observatories in Antarctica. Bologna: Compositori*, pages 67–92.

Bonvalot, S., Balmino, G., Briais, A., Kuhn, M., Peyrefitte, A., Vales, N., Biancale, R., Gabalda, G., Reinquin, F., and Sarrailh, M. (2012). World Gravity Map.

Bouligand, C., Glen, J. M., and Blakely, R. J. (2014). Distribution of buried hydrothermal alteration deduced from high-resolution magnetic surveys in Yellowstone National Park. *Journal of Geophysical Research: Solid Earth*, 119(4):2595–2630.

Bozzo, E., Caneva, G., and Manzoni, M. (1987). Geomagnetic investigations in the Terra Nova Bay region, Victoria Land, Antarctica. *5th Symp. Antarctic Earth Sci., Abstracts*, 143.

Bozzo, E., Ghezzi, G., Simeoni, U., and Taviani, M. (1991). The magnetic susceptibility of Ross Sea continental shelf surficial sediments (Antarctica). *Memorie della Società Geologica Italiana*, 46:563–569.

Brenn, G. R., Hansen, S. E., and Park, Y. (2017). Variable thermal loading and flexural uplift along the Transantarctic Mountains, Antarctica. *Geology*, 45(5):463–466.

Cady, J. W. (1980). Calculation of Gravity and Magnetic Anomalies of Finite-length Right Polygonal Prisms. *Geophysics*, 45(10):1507–1512.

Campbell, D. L. (1983). *BASIC Programs to Calculate Gravity and Magnetic Anomalies for 2 1/2-dimensional Prismatic Bodies*. USGS, Open-file Report 83-154.

Cande, S. C. and Kent, D. V. (1992). A new geomagnetic polarity time scale for the Late Cretaceous and Cenozoic. *Journal of Geophysical Research*, 97(B10):13917.

Cande, S. C. and Kent, D. V. (1995). Revised calibration of the geomagnetic polarity timescale for the Late Cretaceous and Cenozoic. *Journal of Geophysical Research: Solid Earth*, 100(B4):6093–6095.

Carmichael, R. (1982). Magnetic properties of minerals and rocks, CRC Handbook of Physical Properties of Rocks, II RS Carmichael, 229–287.

Carmignani, L., Ghezzo, C., Gosso, G., Lombardo, B., Meccheri, M., Montrasio, A., Pertusati, P., and Salvini, F. (1988). Geological map of the area between David and Mariner glaciers, Victoria Land, Antarctica. *Memorie della Società Geologica Italiana*, 33:77–97.

Clark, D. A. (1983). Comments on Magnetic Petrophysics. *Exploration Geophysics*, 14(2):49–62.

Clark, D. A. (1997). Magnetic petrophysics and magnetic petrology: aids to geological interpretation of magnetic surveys. *AGSO J. Aust. Geol. Geophys.*, 17(2):83–103.

Clark, D. A. and Emerson, J. B. (1991). Notes On Rock Magnetization Characteristics In Applied Geophysical Studies. *Exploration Geophysics*, 22(3):547–555.

Cremisini, C., Gianelli, G., Mussi, M., and Torcini, S. (1991). Geochemistry and isotope chemistry of surface waters and geothermal manifestations at Terra Nova Bay,(Victoria Land, Antarctica). *Memorie della Società Geologica Italiana*, 46:463–475.

Daly, R. A., Manger, G. E., and Clark, S. P. (1966). Section 4: Density of rocks. In *Geological Society of America Memoirs*, volume 97, pages 19–26. Geological Society of America.

Damaske, D., Schreckenberger, B., and Goldmann, F. (2014). A high resolution aeromagnetic survey over the Mesa Range, northern Victoria Land, Antarctica. *Polarforschung*, 84(1):1–13.

de Moura, D. S., Molina, E. C., Marangoni, Y. R., and Jovane, L. (2019). Gravity and Magnetic Constraints on the Crustal Structure of the Ceará Plateau, Brazilian Equatorial Margin. *Frontiers in Earth Science*, 7.

Del Carlo, P., Di Roberto, A., Di Vincenzo, G., Re, G., Albert, P., Nazzari, M., Smith, V., and Cannata, A. (2022). Tephrostratigraphy of proximal pyroclastic sequences at Mount Melbourne (northern Victoria Land, Antarctica): Insights into the volcanic activity since the last glacial period. *Journal of Volcanology and Geothermal Research*, 422:107457.

Dortman, N. (1976). Fiziceskie svoistva gornich porod i polesnich iskopamych. *Izdat Nedra, Moskva*.

Duane, S., Kennedy, A. D., Pendleton, B. J., and Roweth, D. (1987). Hybrid Monte Carlo. *Physics Letters B*, 195(2):216–222.

Duda, R. O. and Hart, P. E. (1972). Use of the Hough transformation to detect lines and curves in pictures. *Communications of the ACM*, 15(1):11–15.

Dumont, M., Reninger, P. A., Aunay, B., Pryet, A., Jougnot, D., Join, J. L., Michon, L., and Martelet, G. (2021). Hydrogeophysical Characterization in a Volcanic Context From Local to Regional Scales Combining Airborne Electromagnetism and Magnetism. *Geophysical Research Letters*, 48(12).

Dziewonski, A. M. and Anderson, D. L. (1981). Preliminary reference Earth model. *Physics of the Earth and Planetary Interiors*, 25(4):297–356.

Eaton, G. and Watkins, J. (1967). The use of seismic refraction and gravity methods in hydrologic investigations. *Mining and ground-water geophysics: Geological Survey of Canada Economic Geology Report*, 26:554–568.

Ebbing, J., Dilixiati, Y., Haas, P., Ferraccioli, F., and Scheiber-Enslin, S. (2021). East Antarctica magnetically linked to its ancient neighbours in Gondwana. *Scientific Reports*, 11(1):5513.

Einstein, A. (1916). Die Grundlage der allgemeinen Relativitätstheorie. *Annalen der Physik*, 354(7):769–822.

Fairhead, D. (2016). *Ebook: Advances in Gravity and Magnetic Processing and Interpretation*. EAGE Publications bv.

Ferraccioli, F., Armadillo, E., Bozzo, E., and Privitera, E. (2000). Magnetics and gravity image tectonic framework of the Mount Melbourne volcano area (Antarctica). *Physics and Chemistry of the Earth, Part A: Solid Earth and Geodesy*, 25(4):387–393.

Ferraccioli, F., Armadillo, E., Jordan, T., Bozzo, E., and Corr, H. (2009a). Aeromagnetic exploration over the East Antarctic Ice Sheet: A new view of the Wilkes Subglacial Basin. *Tectonophysics*, 478(1-2):62–77.

Ferraccioli, F., Armadillo, E., Zunino, A., Bozzo, E., Rocchi, S., and Armienti, P. (2009b). Magmatic and tectonic patterns over the Northern Victoria Land sector of the Transantarctic Mountains from new aeromagnetic imaging. *Tectonophysics*, 478(1-2):43–61.

Ferraccioli, F., Gambetta, M., and Bozzo, E. (1998). Microlevelling procedures applied to regional aeromagnetic data: an example from the Transantarctic Mountains (Antarctica). *Geophysical Prospecting*, 46(2):177–196.

Ferraccioli, F., Jones, P. C., Curtis, M. L., Leat, P. T., and Riley, T. R. (2005). Tectonic and magmatic patterns in the Jutulstraumen rift (?) region, East Antarctica, as imaged by high-resolution aeromagnetic data. *Earth, Planets and Space*, 57(8):767–780.

Fichtner, A., Zunino, A., and Gebraad, L. (2019). Hamiltonian Monte Carlo Solution of Tomographic Inverse Problems. *Geophysical Journal International*, 216(2):1344–1363.

Fichtner, A., Zunino, A., Gebraad, L., and Boehm, C. (2021). Autotuning Hamiltonian Monte Carlo for Efficient Generalized Nullspace Exploration. *Geophysical Journal International*, 227(2):941–968.

Finn, C. A., Bedrosian, P. A., Holbrook, W. S., Auken, E., Bloss, B. R., and Crosbie, J. (2022). Geophysical imaging of the Yellowstone hydrothermal plumbing system. *Nature*, 603(7902):643–647.

Finn, C. A., Deszcz-Pan, M., Anderson, E. D., and John, D. A. (2007). Three-dimensional geophysical mapping of rock alteration and water content at Mount Adams, Washington: Implications for lahar hazards. *Journal of Geophysical Research*, 112(B10):B10204.

Finn, C. A. and Morgan, L. A. (2002). High-resolution aeromagnetic mapping of volcanic terrain, Yellowstone National Park. *Journal of Volcanology and Geothermal Research*, 115(1-2):207–231.

Fletcher, R. (1987). *Practical methods of optimization*. Wiley, Chichester ; New York, 2nd ed edition.

Gambino, S., Aloisi, M., Falzone, G., and Ferro, A. (2016). Tilt signals at Mount Melbourne, Antarctica: evidence of a shallow volcanic source. *Polar Research*, 35(1):28269.

Gambino, S., Armienti, P., Cannata, A., Del Carlo, P., Giudice, G., Giuffrida, G., Liuzzo, M., and Pompilio, M. (2021). Chapter 7.3 Mount Melbourne and Mount Rittmann. *Geological Society, London, Memoirs*, 55(1):741–758.

GANOVEX Team (1987). Geological map of North Victoria land, Antarctica, 1: 500,000—explanatory notes. *Geologisches Jahrbuch B*, 66:7–79.

Gebremedhin, A. H. and Walther, A. (2020). An Introduction to Algorithmic Differentiation. *WIREs Data Mining and Knowledge Discovery*, 10(1):e1334.

Geshi, N. (2008). Vertical and lateral propagation of radial dikes inferred from the flow-direction analysis of the radial dike swarm in Komochi Volcano, Central Japan. *Journal of Volcanology and Geothermal Research*, 173(1-2):122–134.

Ghalenoei, E., Dettmer, J., Ali, M. Y., and Kim, J. W. (2022). Trans-dimensional gravity and magnetic joint inversion for 3-D earth models. *Geophysical Journal International*, 230(1):363–376.

Ghidella, M., Zambrano, O., Ferraccioli, F., Lirio, J., Zakrajsek, A., Ferris, J., and Jordan, T. (2013). Analysis of James Ross Island volcanic complex and sedimentary basin based on high-resolution aeromagnetic data. *Tectonophysics*, 585:90–101.

Giordano, G., Lucci, F., Phillips, D., Cozzupoli, D., and Runci, V. (2012). Stratigraphy, geochronology and evolution of the Mt. Melbourne volcanic field (North Victoria Land, Antarctica). *Bulletin of Volcanology*, 74(9):1985–2005.

Golynsky, A. V., Ferraccioli, F., Hong, J. K., Golynsky, D. A., von Frese, R. R. B., Young, D. A., Blankenship, D. D., Holt, J. W., Ivanov, S. V., Kiselev, A. V., Masolov, V. N., Eagles, G., Gohl, K., Jokat, W., Damaske, D., Finn, C., Aitken, A., Bell, R. E., Armadillo, E., Jordan, T. A., Greenbaum, J. S., Bozzo, E., Caneva, G., Forsberg, R., Ghidella, M., Galindo-Zaldivar, J., Bohoyo, F., Martos, Y. M., Nogi, Y., Quartini, E., Kim, H. R., and Roberts, J. L. (2018). New Magnetic Anomaly Map of the Antarctic. *Geophysical Research Letters*, 45(13):6437–6449.

Goodge, J. W. and Finn, C. A. (2010). Glimpses of East Antarctica: Aeromagnetic and satellite magnetic view from the central Transantarctic Mountains of East Antarctica. *Journal of Geophysical Research*, 115(B9):B09103.

Grant, F. (1973). Magnetic susceptibility mapping: The first years experience. In *43rd Annual International Meeting, Society of Exploration Geophysics, Mexico City, 1973*.

Grant, F. (1985a). Aeromagnetics, geology and ore environments, I. Magnetite in igneous, sedimentary and metamorphic rocks: An overview. *Geoexploration*, 23(3):303–333.

Grant, F. (1985b). Aeromagnetics, geology and ore environments, II. Magnetite and ore environments. *Geoexploration*, 23(3):335–362.

Grant, F. S. and West, G. F. (1965). *Interpretation theory in applied geophysics*. New York: McGraw-Hill.

Grauch, V. J. S. and Hudson, M. R. (2011). Aeromagnetic anomalies over faulted strata. *The Leading Edge*, 30(11):1242–1252.

Griewank, A. and Walther, A. (2008). *Evaluating Derivatives: Principles and Techniques of Algorithmic Differentiation*. Society for Industrial and Applied Mathematics, Philadelphia, PA, 2nd ed edition.

Gubellini, A. and Postpischl, D. (1991). The Mount Melbourne (Antarctica) geodetic network. *Memorie della Società Geologica Italiana*, 46:595–610.

Hadamard, J. (1902). Sur les problèmes aux dérivées partielles et leur signification physique. *Princeton university bulletin*, pages 49–52.

Haggerty, S. E. (1979). The aeromagnetic mineralogy of igneous rocks. *Canadian Journal of Earth Sciences*, 16(6):1281–1293.

Hamlyn, J. E., Keir, D., Wright, T. J., Neuberg, J. W., Goitom, B., Hammond, J. O. S., Pagli, C., Oppenheimer, C., Kendall, J.-M., and Grandin, R. (2014). Seismicity and subsidence following the 2011 Nabro eruption, Eritrea: Insights into the plumbing system of an off-rift volcano. *Journal of Geophysical Research: Solid Earth*, 119(11):8267–8282.

Hansen, T. M., Cordua, K. S., Zunino, A., and Mosegaard, K. (2016). Probabilistic Integration of Geo-Information. In *Integrated Imaging of the Earth*, pages 93–116. American Geophysical Union (AGU). Section: 6.

Harrington, H. J. (1958). Nomenclature of Rock Units in the Ross Sea Region, Antarctica. *Nature*, 182(4631):290–290.

Hart, P. (2009). How the Hough transform was invented [DSP History]. *IEEE Signal Processing Magazine*, 26(6):18–22.

Hawkins, R. and Sambridge, M. (2015). Geophysical imaging using trans-dimensional trees. *Geophysical Journal International*, 203(2):972–1000.

Henkel, H. (1976). Studies of density and magnetic properties of rocks from Northern Sweden. *Pure and Applied Geophysics*, 114(2):235–249.

Hinze, W. J., von Frese, R. R. B., and Saad, A. H. (2013). *Gravity and Magnetic Exploration: Principles, Practices, and Applications*. Cambridge University Press, Cambridge.

Hoffman, M. D. and Gelman, A. (2014). The No-U-Turn sampler: adaptively setting path lengths in Hamiltonian Monte Carlo. *J. Mach. Learn. Res.*, 15(1):1593–1623.

Hornig, I., Worner, G., and Zipfel, J. (1991). Lower crustal and mantle xenoliths from the Mt. Melbourne volcanic field, northern Victoria Land, Antarctica. *Memorie della Società Geologica Italiana*, 46:337–352.

Hrouda, F. (1982). Magnetic anisotropy of rocks and its application in geology and geophysics. *Geophysical Surveys*, 5(1):37–82.

Hubbert, M. K. (1948). A Line-Integral Method of Computing the Gravimetric Effects of Two-Dimensional Masses. *Geophysics*, 13(2):215–225.

Huenges, E. and Ledru, P. (2011). *Geothermal energy systems: exploration, development, and utilization*. John Wiley & Sons.

Huerta, A. D. and Harry, D. L. (2007). The transition from diffuse to focused extension: Modeled evolution of the West Antarctic Rift system. *Earth and Planetary Science Letters*, 255(1-2):133–147.

Hunt, C. P., Moskowitz, B. M., Banerjee, S. K., and others (1995). Magnetic properties of rocks and minerals. *Rock physics and phase relations: A handbook of physical constants*, 3:189–204.

Jahren, C. E. (1963). Magnetic susceptibility of bedded iron-formation. *Geophysics*, 28(5):756–766.

Johnson, G. and Olhoeft, G. (1984). Density of rocks and minerals Handbook of Physical Properties of Rocks ed Carmichael RS.

Jordan, T., Neale, R., Leat, P., Vaughan, A., Flowerdew, M., Riley, T., Whitehouse, M., and Ferraccioli, F. (2014). Structure and evolution of Cenozoic arc magmatism on the Antarctic Peninsula: a high resolution aeromagnetic perspective. *Geophysical Journal International*, 198(3):1758–1774.

Jordan, T. A., Ferraccioli, F., and Forsberg, R. (2022). An embayment in the East Antarctic basement constrains the shape of the Rodinian continental margin. *Communications Earth & Environment*, 3(1):52.

Keys, J., McIntosh, W., and Kyle, P. (1983). Volcanic activity of Mount Melbourne, Northern Victoria Land. *Antarctic journal of the United States*, 18(5):10–11.

Kim, H. R., Golynsky, A. V., Golynsky, D. A., Yu, H., von Frese, R. R. B., and Hong, J. K. (2022). New Magnetic Anomaly Constraints on the Antarctic Crust. *Journal of Geophysical Research: Solid Earth*, 127(3).

Kostrov, N. P. (2007). Calculation of magnetic anomalies caused by 2D bodies of arbitrary shape with consideration of demagnetization. *Geophysical Prospecting*, 55(1):91–115.

Kovesi, P. (1999). Image features from phase congruency. *Videre: Journal of computer vision research*, 1(3):1–26. Publisher: Citeseer.

Kovesi, P. (2003). Phase congruency detects corners and edges. In *The australian pattern recognition society conference: DICTA*, volume 2003.

Kravchinsky, V. A., Hnatyshin, D., Lysak, B., and Alemie, W. (2019). Computation of Magnetic Anomalies Caused by Two-Dimensional Structures of Arbitrary Shape: Derivation and Matlab Implementation. *Geophysical Research Letters*, 46(13):7345–7351.

Kreuzer, H. (1988). Unpublished report.

Ku, C. C. (1977). A direct computation of gravity and magnetic anomalies caused by 2-and 3-dimensional bodies of arbitrary shape and arbitrary magnetic polarization by equivalent-point method and a simplified cubic spline. *Geophysics*, 42(3):610–622.

Kuang, X., Zhu, X., Ning, F., Li, W., Zheng, Q., Li, B., and Zhou, D. (2022). Aeromagnetic-Imaged Basement Fault Structure of the Eastern Tarim Basin and Its Tectonic Implication. *Frontiers in Earth Science*, 9.

Kyle, P. (1990). A. McMurdo volcanic group western Ross embayment. *Volcanoes of the Antarctic plate and southern Oceans*, 48:18–145. Publisher: Wiley Online Library.

Kyle, P. R. and Cole, J. W. (1974). Structural control of volcanism in the McMurdo Volcanic Group, Antarctica. *Bulletin Volcanologique*, 38(1):16–25.

Lanza, R., Manzoni, M., and Miletto, M. (1991). Paleomagnetic data from the Mt. Melbourne volcanic province, North Victoria Land, Antarctica. *Memorie della Società Geologica Italiana*, 46:533–541.

Lanzafame, G. and Villari, L. (1991). Structural evolution and volcanism in Northern Victoria Land (Antarctica): data from Mt. Melbourne-Mt. Overlord-Malta Plateau region. *Memorie della Società Geologica Italiana*, 46:371–381.

Lee, H., Seo, H., Han, H., Ju, H., and Lee, J. (2021). Velocity Anomaly of Campbell Glacier, East Antarctica, Observed by Double-Differential Interferometric SAR and Ice Penetrating Radar. *Remote Sensing*, 13(14):2691.

Lee, M. J., Kyle, P. R., Iverson, N. A., Lee, J. I., and Han, Y. (2019). Rittmann volcano, Antarctica as the source of a widespread 1252 ± 2 CE tephra layer in Antarctica ice. *Earth and Planetary Science Letters*, 521:169–176.

Lee, M. J., Lee, J. I., Kim, T. H., Lee, J., and Nagao, K. (2015). Age, geochemistry and Sr-Nd-Pb isotopic compositions of alkali volcanic rocks from Mt. Melbourne and the western Ross Sea, Antarctica. *Geosciences Journal*, 19(4):681–695.

Lee, T., Kashyap, R., and Chu, C. (1994). Building Skeleton Models via 3-D Medial Surface Axis Thinning Algorithms. *CVGIP: Graphical Models and Image Processing*, 56(6):462–478.

Li, C.-F., Lu, Y., and Wang, J. (2017). A Global Reference Model of Curie-point Depths Based on EMAG2. *Scientific Reports*, 7(1):45129.

Li, Y. and Oldenburg, D. W. (1998). 3-D Inversion of Gravity Data. *Geophysics*, 63(1):109–119.

Li, Y. and Oldenburg, D. W. (2000). Joint Inversion of Surface and Three-Component Borehole Magnetic data. *Geophysics*, 65(2):540–552.

Li, Y., Shearer, S. E., Haney, M. M., and Dannemiller, N. (2010). Comprehensive Approaches to 3D Inversion of Magnetic Data Affected by Remanent Magnetization. *Geophysics*, 75(1):L1–L11.

Lindsley, D. H., Andreasen, G. E., and Balsley, J. R. (1966). Section 25: Magnetic properties of rocks and minerals. In *Geological Society of America Memoirs*, volume 97, pages 543–552. Geological Society of America.

Llubes, M., Seoane, L., Bruinsma, S., and Rémy, F. (2018). Crustal Thickness of Antarctica Estimated Using Data from Gravimetric Satellites. *Solid Earth*, 9(2):457–467.

Luo, X. (2010). Constraining the shape of a gravity anomalous body using reversible jump Markov chain Monte Carlo. *Geophysical Journal International*, 180(3):1067–1079.

Luyendyk, A. (1997). Processing of airborne magnetic data. *AGSO Journal of Australian Geology and Geophysics*, 17:31–38.

Lyon, G. L. (1986). Stable isotope stratigraphy of ice cores and the age of the last eruption at Mount Melbourne, Antarctica. *New Zealand Journal of Geology and Geophysics*, 29(1):135–138.

Lyon, G. L. and Giggenbach, W. F. (1974). Geothermal activity in Victoria Land, Antarctica. *New Zealand Journal of Geology and Geophysics*, 17(3):511–521.

Läufer, A., Damaske, D., and Lisker, F. (2011). Neogene tectonics in the Edisto and Tucker Inlet region and its correlation with offshore magnetic anomalies north of Cape Adare, northern Victoria Land, Antarctica. *Polarforschung*, 80(2):111–126.

Maccaferri, F., Rivalta, E., Keir, D., and Acocella, V. (2014). Off-rift volcanism in rift zones determined by crustal unloading. *Nature Geoscience*, 7(4):297–300.

Mader, G. L. (1992). Rapid static and kinematic global positioning system solutions using the ambiguity function technique. *Journal of Geophysical Research: Solid Earth*, 97(B3):3271–3283.

Manzoni, M. and Miletto, M. (1988). Rock-magnetic properties of volcanites from Mt. Melbourne (North Victoria Land): Preliminary results. *Memorie della Società Geologica Italiana*, 43:173–180.

Mariano, J. and Hinze, W. J. (1993). Modeling complexly magnetized two-dimensional bodies of arbitrary shape. *Geophysics*, 58(5):637–644.

Martelet, G., Reninger, P., Perrin, J., and Deparis, J. (2014). Acquisition géophysique héliportée de l'île de La Réunion. *BRGM report*, pages 1–90.

Martos, Y. M., Catalán, M., Jordan, T. A., Golynsky, A., Golynsky, D., Eagles, G., and Vaughan, D. G. (2017). Heat Flux Distribution of Antarctica Unveiled. *Geophysical Research Letters*, 44(22):11,417–11,426.

Martín-Atienza, B. and García-Abdeslem, J. (1999). 2-D gravity modeling with analytically defined geometry and quadratic polynomial density functions. *Geophysics*, 64(6):1730–1734.

Maule, C. F., Purucker, M. E., Olsen, N., and Mosegaard, K. (2005). Heat Flux Anomalies in Antarctica Revealed by Satellite Magnetic Data. *Science*.

Maxwell, J. C. (1873a). *A treatise on electricity and magnetism*, volume 2. Oxford : Clarendon Press.

Maxwell, J. C. (1873b). *A treatise on electricity and magnetism*, volume 1. Oxford : Clarendon Press.

Menke, W. (2018). *Geophysical data analysis: Discrete inverse theory*. Academic press.

Metropolis, N., Rosenbluth, A. W., Rosenbluth, M. N., Teller, A. H., and Teller, E. (1953). Equation of State Calculations by Fast Computing Machines. *The Journal of Chemical Physics*, 21(6):1087–1092.

Meyer, B. and Saltus, R. (2016). EMAG2: Earth Magnetic Anomaly Grid (2-arc-minute resolution) Version 3.

Mieth, M., Jacobs, J., Ruppel, A., Damaske, D., Läufer, A., and Jokat, W. (2014). New detailed aeromagnetic and geological data of eastern Dronning Maud Land: Implications for refining the tectonic and structural framework of Sør Rondane, East Antarctica. *Precambrian Research*, 245:174–185.

Milano, M., Kelemework, Y., La Manna, M., Fedi, M., Montanari, D., and Iorio, M. (2020). Crustal Structure of Sicily from Modelling of Gravity and Magnetic Anomalies. *Scientific Reports*, 10(1):16019.

Miller, H. G. and Singh, V. (1994). Potential field tilt—a new concept for location of potential field sources. *Journal of Applied Geophysics*, 32(2-3):213–217.

Morlighem, M., Rignot, E., Binder, T., Blankenship, D., Drews, R., Eagles, G., Eisen, O., Ferraccioli, F., Forsberg, R., Fretwell, P., Goel, V., Greenbaum, J. S., Gudmundsson, H., Guo, J., Helm, V., Hofstede, C., Howat, I., Humbert, A., Jokat, W., Karlsson, N. B., Lee, W. S., Matsuoka, K., Millan, R., Mouginot, J., Paden, J., Pattyn, F., Roberts, J., Rosier, S., Ruppel, A., Seroussi, H., Smith, E. C., Steinhage, D., Sun, B., Broeke, M. R. v. d., Ommen, T. D. v., Wessem, M. v., and Young, D. A. (2020). Deep glacial troughs and stabilizing ridges unveiled beneath the margins of the Antarctic ice sheet. *Nature Geoscience*, 13(2):132–137.

Mosegaard, K. and Tarantola, A. (1995). Monte Carlo Sampling of Solutions to Inverse Problems. *Journal of Geophysical Research: Solid Earth (1978– 2012)*, 100(B7):12431–12447.

Mosegaard, K. and Tarantola, A. (2002). Probabilistic Approach to Inverse Problems. In *International Geophysics*, volume 81, pages 237–265. Elsevier.

Müller, P., Schmidt-Thomé, M., Kreuzer, H., Tessensohn, F., and Vetter, U. (1991). Cenozoic prealkaline magmatism at the western margin of the Ross Sea, Antarctica. *Memorie della Società Geologica Italiana*, 46:315–336.

Nabighian, M. N., Grauch, V. J. S., Hansen, R. O., LaFehr, T. R., Li, Y., Peirce, J. W., Phillips, J. D., and Ruder, M. E. (2005). The Historical Development of the Magnetic Method in Exploration. *Geophysics*, 70(6):33ND–61ND.

Nagy, D. (1966). The gravitational attraction of a right rectangular prism. *Geophysics*, 31(2):362–371.

Nathan, S. and Schulte, F. J. (1967). Recent Thermal and Volcanic activity on Mount Melbourne, Northern Victoria Land, Antarctica. *New Zealand Journal of Geology and Geophysics*, 10(2):422–430.

Nathan, S. and Schulte, F. J. (1968). Geology and petrology of the Campbell—Aviator Divide, Northern Victoria Land, Antarctica: Part 1—post Paleozoic rocks. *New Zealand Journal of Geology and Geophysics*, 11(4):940–975.

Neal, R. (2012). MCMC Using Hamiltonian Dynamics. *Handbook of Markov Chain Monte Carlo*.

Newton, 1642-1727, I. (1687). *Philosophiæ naturalis principia mathematica*. Londini : Jussu Societatis Regiae ac Typis Josephi Streater ..., 1687.

Nocedal, J. and Wright, S. J. (2006). *Numerical optimization*. Springer series in operations research and financial engineering. Springer, New York, 2nd ed edition.

O'Gorman and Clowes (1976). Finding Picture Edges Through Collinearity of Feature Points. *IEEE Transactions on Computers*, C-25(4):449–456.

Oldenburg, D. W. (1974). The inversion and interpretation of gravity anomalies. *Geophysics*, 39(4):526–536.

Pappa, F., Ebbing, J., and Ferraccioli, F. (2019). Moho Depths of Antarctica: Comparison of Seismic, Gravity, and Isostatic Results. *Geochemistry, Geophysics, Geosystems*, 20(3):1629–1645.

Parasnis, D. (1971). *Physical Property Guide for Rocks and Minerals*. Geophysical memorandum. Atlas Copco ABEM.

Parker, R. L. (1973). The Rapid Calculation of Potential Anomalies. *Geophysical Journal International*, 31(4):447–455.

Pasquale, V., Verdoya, M., Chiozzi, P., and Armadillo, E. (2009). Thermal, radioactive and magnetic properties of the lavas of the Mt Melbourne Volcanic Field (Victoria Land, Antarctica). *Annals of Geophysics*, 52(2):197–207.

Paxman, G. J. G., Jamieson, S. S. R., Ferraccioli, F., Bentley, M. J., Ross, N., Watts, A. B., Leitchenkov, G., Armadillo, E., and Young, D. A. (2019). The Role of Lithospheric Flexure in the Landscape Evolution of the Wilkes Subglacial Basin and Transantarctic Mountains, East Antarctica. *Journal of Geophysical Research: Earth Surface*, 124(3):812–829.

Pertusati, P., Musumeci, G., Carosi, R., Meccheri, M., Baroni, C., Capponi, G., Carmignani, L., Castelli, D. C. C., Crispini, L., Di Vincenzo, G., Ghezzo, C., Montomoli, C., Montrasio, A., Oggiano, G., Perchiazzi, N., Ricci, C., Salvini, F., Skinner, D., Talarico, F., and Tessenshon, F. (2012). Antarctic Geological 1: 250.000 Map Series–Mount Melbourne Quadrangle (Victoria Land). Publisher: Museo Nazionale dell'Antartide, Scienze della Terra, Siena.

Plouff, D. (1975). Derivation of formulas and FORTRAN programs to compute magnetic anomalies of prisms. *Final Report*, pages 1973–1974.

Plouff, D. (1976). Gravity and magnetic fields of polygonal prisms and application to magnetic terrain corrections. *Geophysics*, 41(4):727–741.

Raimbourg, H., Jolivet, L., and Leroy, Y. (2007). Consequences of progressive eclogitization on crustal exhumation, a mechanical study. *Geophysical Journal International*, 168(1):379–401.

Rasmussen, R. and Pedersen, L. B. (1979). End Corrections in Potential Field Modeling. *Geophysical Prospecting*, 27(4):749–760.

Ravat, D., Lu, Z., and Braile, L. (1999). Velocity–density relationships and modeling the lithospheric density variations of the Kenya Rift. *Tectonophysics*, 302(3-4):225–240.

Ray, A. (2021). Bayesian inversion using nested trans-dimensional Gaussian processes. *Geophysical Journal International*, 226(1):302–326.

Ren, Z., Chen, C., Zhong, Y., Chen, H., Kalscheuer, T., Maurer, H., Tang, J., and Hu, X. (2020). Recursive Analytical Formulae of Gravitational Fields and Gradient Tensors for Polyhedral Bodies with Polynomial Density Contrasts of Arbitrary Non-negative Integer Orders. *Surveys in Geophysics*, 41(4):695–722.

Ren, Z., Zhang, Y., Zhong, Y., Pan, K., Wu, Q., and Tang, J. (2022). Magnetic Anomalies Caused by 3D Polyhedral Structures With Arbitrary Polynomial Magnetization. *Geophysical Research Letters*, 49(18).

Reynolds, R. L. (1977). Magnetic titanohematite minerals in uranium-bearing sandstone. Open-File Report 77-355, US Geological Survey. Series: Open-File Report.

Robert, C. P. (2015). The Metropolis-Hastings Algorithm. *arXiv:1504.01896 [stat]*. arXiv: 1504.01896.

Rocchi, S., Armienti, P., D'Orazio, M., Tonarini, S., Wijbrans, J. R., and Di Vincenzo, G. (2002). Cenozoic magmatism in the western Ross Embayment: Role of mantle plume versus plate dynamics in the development of the West Antarctic Rift System. *Journal of Geophysical Research: Solid Earth*, 107(B9):ECV 5–1–ECV 5–22.

Rochette, P. (1987). Magnetic susceptibility of the rock matrix related to magnetic fabric studies. *Journal of Structural Geology*, 9(8):1015–1020.

Roland, N. W. and Tessensohn, F. (1987). Rennick faulting-an early phase of Ross Sea rifting. *Geologisches Jahrbuch. Reihe B, Regionale Geologie Ausland*, 66:203–229.

Ruppel, A., Läufer, A., Crispini, L., Capponi, G., and Lisker, F. (2017). A high-resolution aeromagnetic survey over the Lanterman Range, northern Victoria Land, Antarctica. page 14182. Conference Name: EGU General Assembly Conference Abstracts ADS Bibcode: 2017EGUGA..1914182R.

Saad, A. H. (1969a). Magnetic properties of ultramafic rocks from Red Mountain, California. *Geophysics*, 34(6):974–987.

Saad, A. H. (1969b). Paleomagnetism of Franciscan ultramafic rocks from Red Mountain, California. *Journal of Geophysical Research*, 74(27):6567–6578.

Salvini, F., Brancolini, G., Busetti, M., Storti, F., Mazzarini, F., and Coren, F. (1997). Cenozoic geodynamics of the Ross Sea region, Antarctica: Crustal extension, intraplate strike-slip faulting, and tectonic inheritance. *Journal of Geophysical Research: Solid Earth*, 102(B11):24669–24696.

Sambridge, M., Rickwood, P., Rawlinson, N., and Sommacal, S. (2007). Automatic Differentiation in Geophysical Inverse Problems. *Geophysical Journal International*, 170(1):1–8.

Scarponi, M., Hetényi, G., Plomerová, J., Solarino, S., Baron, L., and Petri, B. (2021). Joint Seismic and Gravity Data Inversion to Image Intra-Crustal Structures: The Ivrea Geophysical Body Along the Val Sesia Profile (Piedmont, Italy). *Frontiers in Earth Science*, 0.

Scheiber-Enslin, S., Ebbing, J., and Webb, S. J. (2014). An Integrated Geophysical Study of the Beattie Magnetic Anomaly, South Africa. *Tectonophysics*, 636:228–243.

Schön, J. (1996). *Physical properties of rocks: fundamentals and principles of petrophysics*. Number v. 18 in Handbook of geophysical exploration. Seismic exploration. Pergamon, Oxford, OX, UK ; Tarrytown, N.Y., U.S.A, 1st ed edition.

Shuey, R. T. and Pasquale, A. S. (1973). End Corrections in Magnetic Profile Interpretation. *Geophysics*, 38(3):507–512.

Sigmundsson, F., Hreinsdóttir, S., Hooper, A., Árnadóttir, T., Pedersen, R., Roberts, M. J., Óskarsson, N., Auriac, A., Decriem, J., Einarsson, P., Geirsson, H., Hensch, M., Ófeigsson, B. G., Sturkell, E., Sveinbjörnsson, H., and Feigl, K. L. (2010). Intrusion triggering of the 2010 Eyjafjallajökull explosive eruption. *Nature*, 468(7322):426–430.

Silva, J. B. C. and Hohmann, G. W. (1984). Airborne magnetic susceptibility mapping. *Exploration Geophysics*, 15(1):1–13.

Smellie, J. L. and Rocchi, S. (2021). Chapter 5.1a Northern Victoria Land: volcanology. *Geological Society, London, Memoirs*, 55(1):347–381.

Stern, T. A. and ten Brink, U. S. (1989). Flexural uplift of the Transantarctic Mountains. *Journal of Geophysical Research: Solid Earth*, 94(B8):10315–10330.

Storti, F., Balestrieri, M. L., Balsamo, F., and Rossetti, F. (2008). Structural and thermochronological constraints to the evolution of the West Antarctic Rift System in central Victoria Land. *Tectonics*, 27(4).

Talarico, F., Armadillo, E., Ferraccioli, F., and Rastelli, N. (2003). Magnetic petrology of the Ross Orogen in Oates Land (Antarctica). *Terra Antartica*, 10:197–220.

Talwani, M. (1965). Computation with the Help of a Digital Computer of Magnetic Anomalies Caused by Bodies of Arbitrary Shape. *Geophysics*, 30(5):797–817.

Talwani, M. and Heirtzler, J. (1962). The mathematical expression for the magnetic anomaly over a two-dimensional body of polygonal cross-section. *Lamont. Doherty Geol. Obs. Columbia Univ., Tech. Rep*, 6.

Talwani, M. and Heirtzler, J. R. (1964). Computation of Magnetic Anomalies Caused by Two Dimensional Structures of Arbitrary Shape. *Stanford University Publications*, 9(1):464–480.

Talwani, M., Worzel, J. L., and Landisman, M. (1959). Rapid Gravity Computations for Two-Dimensional Bodies with Application to the Mendocino Submarine Fracture Zone. *Journal of Geophysical Research (1896-1977)*, 64(1):49–59.

Tarantola, A. (2005). *Inverse Problem Theory and Methods for Model Parameter Estimation*. SIAM.

Tarling, D. H. and Hrouda, F. (1993). *The magnetic anisotropy of rocks*. Chapman & Hall, London ; New York, 1st ed edition.

ten Brink, U. S., Hackney, R. I., Bannister, S., Stern, T. A., and Makovsky, Y. (1997). Uplift of the Transantarctic Mountains and the bedrock beneath the East Antarctic ice sheet. *Journal of Geophysical Research: Solid Earth*, 102(B12):27603–27621.

Tominaga, M., Tivey, M. A., MacLeod, C. J., Morris, A., Lissenberg, C. J., Shillington, D. J., and Ferrini, V. (2016). Characterization of the in Situ Magnetic Architecture of Oceanic Crust (Hess Deep) Using near-Source Vector Magnetic Data. *Journal of Geophysical Research: Solid Earth*, 121(6):4130–4146.

Tonarini, S., Rocchi, S., Armienti, P., and Innocenti, F. (1997). Constraints on timing of Ross Sea rifting inferred from Cainozoic intrusions from northern Victoria Land, Antarctica. *The Antarctic region: Geological evolution and processes*, pages 511–521. Publisher: Terra Antartica Publication Siena.

van der Meijde, M., Julià, J., and Assumpção, M. (2013). Gravity Derived Moho for South America. *Tectonophysics*, 609:456–467.

Van Rossum, G. and De Boer, J. (1991). Interactively testing remote servers using the Python programming language. *CWI quarterly*, 4(4):283–303.

Verduzco, B., Fairhead, J. D., Green, C. M., and MacKenzie, C. (2004). New insights into magnetic derivatives for structural mapping. *The Leading Edge*, 23(2):116–119.

Vignaroli, G., Balsamo, F., Giordano, G., Rossetti, F., and Storti, F. (2015). Miocene-to-Quaternary oblique rifting signature in the Western Ross Sea from fault patterns in the McMurdo Volcanic Group, north Victoria Land, Antarctica. *Tectonophysics*, 656:74–90.

Whitney, J. A. and Stormer, J. C. (1983). Igneous sulfides in the Fish Canyon Tuff and the role of sulfur in calc-alkaline magmas. *Geology*, 11(2):99.

Wilson, G., Damaske, D., Möller, H.-D., Tinto, K., and Jordan, T. (2007). The geological evolution of southern McMurdo Sound - new evidence from a high-resolution aeromagnetic survey. *Geophysical Journal International*, 170(1):93–100.

Witter, J. B., Glen, J. M. G., Siler, D. L., and Fournier, D. (2018). 2D and 3D Potential Field Mapping and Modelling at the Fallon FORGE Site, Nevada, USA. *GRC Transactions*, 42:21.

Won, I. J. and Bevis, M. (1987). Computing the Gravitational and Magnetic Anomalies Due to a Polygon; Algorithms and Fortran Subroutines. *Geophysics*, 52(2):232–238.

Wörner, G. and Viereck, L. (1987). Subglacial to emergent volcanism at Shield Nunatak, Mt. Melbourne volcanic field, Antarctica. *Polarforschung*, 57(1/2):27–41.

Wörner, G. and Viereck, L. (1989). The Mt. Melbourne Volcanic Field (Victoria Land, Antarctica). I: Field Observations. *Geologisches Jahrbuch. Reihe E, Geophysik*, 38:369–393.

Wörner, G., Viereck, L., Hertogen, J., and Niephaus, H. (1989). The Mt. Melbourne volcanic Field (Victoria Land, Antartica). II. Geochemistry and magma genesis. *Geologisches Jahrbuch. Reihe E, Geophysik*, 38:395–433.

Yang, H., Chemia, Z., Artemieva, I. M., and Thybo, H. (2018). Control on off-rift magmatism: A case study of the Baikal Rift Zone. *Earth and Planetary Science Letters*, 482:501–509.

Zunino, A., Benvenuto, F., Armadillo, E., Bertero, M., and Bozzo, E. (2009). Iterative Deconvolution and Semiblind Deconvolution Methods in Magnetic Archaeological Prospecting. *Geophysics*, 74(4):L43–L51.